Experimental and Numerical Assessment of Multi-Source PM Emissions during Ore Mucking in a Polymetallic Underground Mine Environment

Abdullah Rasheed Qureshi

Lead Supervisor: Dr. Sergei Sabanov

Internal Co-Supervisor: Dr. Emil Bayramov

External Co-Supervisor: Prof. Jürgen Brune

A thesis submitted in fulfillment of the requirements for the degree of Doctor of Philosophy

Department of Mining Engineering

School of Mining and Geosciences

2025

Originality Statement

I affirm that the work submitted is wholly my own and contains no materials previously published or authored by others, save when proper acknowledgment is provided in the thesis. I thus declare that the intellectual substance of this thesis is the result of my own work, and no significant portions of this material have been utilized to meet the requirements for any other degree or diploma at Nazarbayev University or any other educational institution.

Abdullah Rasheed Qureshi

Date: 7th May 2025

Dedication

I completely dedicate my thesis to my respected parents, my cherished wife Faiza Qureshi, my beloved daughter Amna Rasheed Qureshi, and my son Abdul Majid Qureshi, whose steadfast love, support, and understanding have illuminated my path during this arduous academic endeavor. To my parents, whose sacrifices and faith in me have been the cornerstone of my resolve; to my wife, your support and companionship have infused joy into the most challenging times; and to my kids, your innocent and delightful smiles have ignited my ambition to strive for greater accomplishments.

Additionally, I would like to dedicate this thesis to the memory of my friend Abdul Sami Gahejo Abro (Late). He has been a steadfast partner throughout my early career and academic journey. He consistently strived to investigate new academic avenues, and his encouragement motivated me to excel in my endeavors.

My dedication serves as a modest expression of my thanks and a monument to the significant influence they have had on my life and my academic accomplishment.

With my utmost affection and commitment,

Acknowledgment

As I conclude this thesis, I am profoundly grateful to those whose support and guidance have been instrumental throughout this academic journey.

I extend my sincere gratitude to my supervisor, **Dr. Sergei Sabanov**, for his steadfast support, expert advice, and extensive knowledge. His mentorship has significantly refined my research abilities and motivated me to explore new avenues in academia. I am truly privileged to have worked under his guidance.

I am equally thankful to my co-supervisors, **Dr. Emil Bayramov** and **Prof. Jürgen Brune**, for their essential contributions and unwavering support. Their insightful feedback and dedication have been pivotal in shaping this thesis.

I am very appreciative of **Prof. Fidelis Suorineni** and **Prof. Ali Mortazavi,** who served as internal examiners, for their constructive feedback on my research. Their guidance has greatly enhanced the quality of my work, and I am grateful for their expertise and support.

I express my profound gratitude to **Prof. Shimin Liu**, Professor of Energy and Mineral Engineering at Penn State University, USA, for serving as an external examiner. His feedback was instrumental in improving the overall quality of my research.

I also extend my sincere thanks to **Prof. Peyman Pourafshary,** Acting Vice Dean for Academic Affairs and Research, for his efforts in managing and coordinating the smooth conduct of my PhD thesis defense.

I acknowledge the continuous support of **Dr. Izhar Mithal Jiskani,** Post.Doc, Department of Sustainability and Planning, Aalborg University, Denmark, for his tireless assistance in reviewing and suggesting improvements throughout the research process.

I am grateful to **Nursultan Magauiya**, **Nursultan Kuzembayev**, and **Gulim Kurmangazy** for their contributions to fieldwork experimentation and their unwavering support.

I am thankful to Nazarbayev University for providing funding for this project under **Research Grant #0122022FD4128**.

I extend my thanks to all the faculty members and administrative staff of the School of Mining and Geosciences for their continuous support and assistance.

Finally, I appreciate everyone who has been part of this remarkable journey, contributing to my pursuit of knowledge and making it a gratifying and enriching experience.

Abstract

Particulate matter (PM) emissions during load-haul-dump (LHD) operations in underground polymetallic mines pose significant health risks to miners and contribute to environmental pollution. This study investigates the PM dispersion from various emission sources during ore handling in a polymetallic underground mine. A combined approach of field experimentation and numerical simulation was employed to evaluate the airflow dynamics and PM diffusion characteristics in the operational drift of mine, situated in East Kazakhstan. For numerical simulation, ANSYS Fluent was used to model and analyze the scenarios. Two primary operating conditions (OC-1 and OC-2) were examined. In OC-1 the airflow and PM2.5 dispersion characteristics were evaluated based on existing and simulating volumetric airflows during LHD handling ore, including condition 1 (C1) loading at the working face, condition 2 (C2) dumping at a temporary dumpsite, and condition (C3) dumping into an underground mine truck (UMT). The existing volumetric airflow in the mine drift was Q = 13 m^3/s, and the simulated volumetric airflows were Q = 15, 17, and 20 m^3/s to assess the impact of increased ventilation rate on PM dispersion. In OC-2 airflow patterns and PM mitigation strategies were investigated under four auxiliary ventilation system (AVS) designs. The four AVS designs were categorized based on the positioning of AVS ducts' outlets and all four AVS designs were assessed under scenario 1 (S1) loading near the working face, and scenario 2 (S2) unloading inside the temporary dumpsite. The numerical simulation was compared with the data collected during the field experimentation to validate the results. The comparative analysis revealed the difference between experimental and simulation results for both airflow and PM was less than 10% in OC-1 and OC-2. The research delineates complex airflow patterns characterized by backflow, vortex, unsteady, and steady flow regions. Findings indicate that C2 exposes LHD operators to the highest PM concentrations, followed by C1, while C3 results in greater PM exposure for UMT operators compared to LHD operators. The study further evaluates PM diffusion characteristics across the experimental and simulated volumetric airflows and AVS designs in both OC-1 and OC-2. The analysis of the novel combination of spatial-temporal model and multiple sources of PM revealed that Q = 17 m^3/s was able to reduce PM concentrations to 28%, 29%, and 20% in C1, C2, and C3, respectively. Similarly, AVS 2 showed 15% and 27% reduction of PM concentrations in S1 and S2, respectively. Moreover, correlation equations, with high coefficient values (R^2), were proposed between the PM concentrations and length of the mine drift to predict the PM concentrations for similar operating conditions in underground mines. These findings provide valuable insights for developing strategies to reduce elevated PM concentrations in the mine drifts. Implementing the recommended AVS designs, and volumetric airflows can significantly enhance air quality management in underground mining environments, promoting miner health and operational efficiency.

Keywords: Auxiliary Ventilation System, Diesel-powered equipment, Dual Duct Forced, Field experimentation, Numerical simulation, Particulate matter, Pollution risks, Underground mine environment, Volumetric airflows

Contents

List of Figures

List of Tables

1. Introduction

1.1. Background

The mining industry produces raw materials to meet global industrial demands. The mining system consists of sub-systems, which involve excavation, transportation and processing. However, these mining subsystems contribute to the generation of hazardous materials (PM and gases), posing a threat to the health of underground miners and the mine environment [1-3].

Diesel-powered equipment (DPE) is essential to the mining transportation sector due to its operational versatility and accessibility. The variable working conditions of the DPE produce diesel particulate matter (DPM), and the generation of other hazardous aerosols in underground mines [4, 5]. Airborne dust generation and migration in underground mines are affected by dust particle size, shape, density, ventilation system, mine opening size and shape, and ongoing mining operations [6, 7]. Thus, airborne dust particle size distribution affects dust dispersion within mining systems [8].

PM sizes vary from coarse particles ≤ 10 μm, fine particles ≤ 2.5 μm, and ultra-fine particles ≤ 1 μm [9]. PM may remain suspended for extended periods owing to their small size. The human body can inhale an excessive amount of suspended PM after prolonged exposure. PM can bypass human body defenses and cause damage in the lungs by transporting additional hazardous substances to the alveoli. Particles from the alveolar epithelium can spread to connective tissue, blood, and lymph, causing respiratory and blood system diseases and possibly cancer [10-13]. Recent research at Harvard's T. H. Chan School of Public Health found that polluted air containing excessively small particles increases early mortality [14]. Air pollution causes 4.2 million casualties worldwide, making it the fifth biggest cause of death, according to the World Health Organization (WHO) [15-18]. The National Institute for Occupational Safety and Health (NIOSH) specifies PM as a potential occupational carcinogen, while the International Agency for Research on Cancer (IARC) classifies it as a Group 1 human carcinogen [19, 20].

Underground mining environments, characterized by narrow roadways, restricted cross-sectional areas, and poor ventilation, are prone to the prolonged suspension of air contaminants, hindering their effective dissipation. Furthermore, these conditions substantially elevate the susceptibility of these contaminants to human health relative to non-mining areas[21-23].

Therefore, it is crucial to examine the attributes and dispersion of PM generated during material transport by LHD under varying operational situations to formulate solutions aimed at mitigating miners' exposure to potential hazardous materials.

Presently, many methods have been employed in underground mines to mitigate PM risks including the utilization of biodiesel, the implementation of diesel filters, and the deployment of environmental cabs and ventilation systems [24] . The AVS is the primary technology for diluting PM in underground mines. For this reason, an effective and economic AVS design is necessary, which contains both airflow quantity and the length and position of the outlets of ducts. Usually, a single duct forced (SDF), dual duct hybrid (DDH),

or a dual duct forced (DDF) AVS is adopted to ventilate and control PM in mine working faces or roadways with a dead end. Additionally, Computational Fluid Dynamics (CFD) can be used for this purpose to visualize the intricacies related to airflow dynamics and PM dilution by changing the AVS characteristics. CFD has been effectively utilized in mining engineering research to address diverse issues connected to air and particle flow.

Chang et al. [24] employed CFD to analyze the concentration distribution and diffusion patterns of DPM at various positions of SDF-AVS at the mine working face. Their findings indicated that an AVS with a pipe length exceeding the actual length by 5 m exhibited higher dilution efficacy for DPM. Duan et al. [25] utilized CFD to investigate the dispersion patterns of DPM under SDF-AVS in an underground mine. The excavation working face indicated that DPM accumulated on both sides of the monorail crane and within the airflow's blind zone. Liu et al. [26] adopted CFD to investigate the distribution of PM generated by trackless rubber wheel vehicles (TRTVs) at idling speeds under various operational situations and recommended appropriate ventilation strategies. The mine was equipped with SDF-AVS. Xu et al. [27] employed an isolation zone of an underground mine as an operational model and utilized CFD to predict the concentration distribution of DPM within this isolation area of an underground coal mine. 2D and 3D models were developed to thoroughly examine the airflow and particle concentration distribution features within the roadway. The roadway contained two dump/load sites but was not equipped with any AVS. These studies adopted SDF-AVS to mitigate the DPM in a working face or near a dead-end inside an underground coal mine.

I.M. Konduri et al. [28] investigated airflow migration and dust diffusion at the working face under DDHAVS by a combination of numerical simulation and experimental testing, thereby elucidating the principles governing airflow migration and dust diffusion. Liu et al. [29] examined airflow dynamics and dust dispersion in the roadway utilizing the DDH-AVS by integrating numerical modeling with field measurements. The findings indicate that an increased distance between the air pressure outlet and the head enhances the reduction and regulation of dust dispersion in the roadway, with optimal dust removal efficacy occurring at 35 m. In another study. Cheng et al. [30] used CFD to simulate the effects of various ventilation parameters on the airflow and dust flow fields under DDH-AVS. The results indicate that the dust suppression efficacy of the air curtain is optimal when the air inlet-outlet ratio is 0.75 and the distance between the air curtain generator and the working face is 20 m.

Zhou et al. [31] examine PM and tail gas flow affected by DDH-AVS in a fully mechanized working face. The research additionally investigated the influence of air suction volume and the distance between the DPE and the heading face on the diffusion dynamics of particulate matter and exhaust gases. The findings indicated that a reduced distance between the DPE and the heading face necessitated an increased volumetric airflow to effectively dilute the harmful particles. Conversely, reduced volumetric airflow adequately dilutes the DPM and tail gas when the distance between the heading face and DPE is extended. In another study, Zhou et al. [32] examined the pollution for dust from the heading face and DPM under DDH-AVS in a mechanized excavation face. Several operational scenarios were developed utilizing CFD,

focusing on the air intake volumes of the dust removal (exhausted) fan and the distance from the fan's outlet to the heading face. The findings indicated that optimal management of dust and DPM is attained with varying volumetric air intakes when the distance from the dust removal fan outlet to the heading face is 5

m. Wang et al. [33] utilized CFD to suggest a ventilation and dust control strategy employing DDF-AVS at the tunnel excavation face, with the objective of optimizing dust control and reduction methods in the underground coal mining environment. The ideal configuration stipulates a distance of 5 m between the DDF-AVS outlet on the driver's side and the excavation face, a distance of 5 m between the DDF-AVS on the return air side and the excavation face, and an airflow ratio of 6:4 between the DDF-AVS.

1.2. Problem statement

Despite these numerous studies conducted in underground coal mines to address the substantial PM exposure and potential health impact on the human and environment, there are still challenges that complicate the understanding of PM sources and behavior under different AVS in underground mines. Firstly, a significant literature review reveals that most studies explicitly refer to "PM" in the context of surface mines [34-38], while "DPM" is specifically linked to underground mines [25, 39-42]. This distinction is likely due to the elemental composition of DPM which poses greater health risks than PM. Thus, significant attention has been given to DPM in underground mines, rather than other potential sources of PM in underground mines.

Moreover, the necessary airflow quantity in an underground mine is generally calculated by multiplying the engine power of the diesel vehicles operating within the mine by the unit airflow requirement. This requirement typically ranges from 0.05 to 0.06 cubic meters per second kilowatt of engine power (m^3/kWs) in Australia, 0.047 to 0.092 m^3/kWs in Canada, 0.067 m^3/kWs in China, and 0.063 m^3/kWs in South Africa [43, 44]. Usually, the AVS supply a constant airflow quantity at the working face, while the mining operations are dynamic. The diverse operating conditions contribute to various scenarios and sources of PM generation. These include the operation of multiple DPEs, performing the loading and dumping of ore, and idling at a constant speed. It remains unclear how these volumetric airflows or AVS designs influence the effectiveness of the PM diffusion with varying operating conditions. This study conducts field work in a polymetallic underground mine in Kazakhstan. Currently, no policy specifies the required airflow quantities for effective dilution of PM in underground mines in the region. As global demand for minerals continues to rise, the depths of mines have significantly increased, presenting new challenges for mine ventilation systems. To ensure adequate airflow under these conditions, the SDF-AVS may not suffice, making the installation of the DDF-AVS necessary. Furthermore, operating parameters such as airflow quantity and outlet position are typically determined based on practical experience [33]. To maximize the potential of the DDF-AVS, it is crucial to explore the AVS airflow quantities and outlet positions in relation to PM generation from various sources and dispersion in underground mines. Therefore, a thorough investigation into the characteristics and optimal parameters of the DDF-AVS is imperative.

Addressing these gaps is crucial for developing effective ventilation strategies and technical measures to reduce PM exposure. There is an urgent need for research that integrates field experiments with numerical simulations to evaluate and optimize DDF-AVS supplied volumetric airflows and outlets position under various operational conditions, including different DPE operations and the influence of LHD activities on airflow dynamics and PM dispersion. The insights acquired will be essential for enhancing health and safety of miners, improving air quality, and promoting sustainable practices in underground mining environments.

1.3. Aim and objectives

To study the multi-source PM generation and transposition under dynamic airflow velocity and AVS design characteristics, the aim of this thesis is to analyze a novel combination of spatial-temporal modelling and PM emitted from multiple sources to propose a PM diffusion model for dynamic operating conditions in the operational drift of an underground mine.

The primary objectives are as follows:

- Determine the existing airflow and PM concentrations by experimental measurement in the mine operational drifts and produce the numerical simulation to further analyze different aspects of airflow and PM generation.
- Evaluate the influence of different volumetric airflows and elaborate a correlation between the airflow and PM dispersion.
- Evaluate the effectiveness of existing and simulated DDF-AVS designs over PM dispersion and analyze a relationship between AVS design and PM dispersion.

1.4. Research hypotheses

PM2.5 emissions produced during LHD operations in underground polymetallic mines pose considerable occupational health hazards and jeopardize the efficacy of typical ventilation systems. Maintaining appropriate air quality standards necessitates a comprehensive understanding of airflow dynamics and pollutants dispersion under diverse operational circumstances. While previous studies have examined general ventilation practices, there is a lack of research dedicated to assessing specific design configurations and airflow modifications through integrated experimental and simulation methodologies. This study hypothesizes optimizing ventilation parameters, particularly by enhancing volumetric airflow rates and strategically positioning AVS outlets will substantially decrease PM2.5 concentrations during LHD operations in underground polymetallic mines, thus reducing miners' exposure and enhancing overall air quality.

1.5. Proposed methodology and research framework

To achieve the research objectives, the research framework adopted in this research study is shown in Fig. 1. A mine drift with a working face and a temporary dumpsite, and a haulage drift considered inside a

polymetallic underground mine situated in East Kazakhstan. Several monitoring points at different cross-sectional planes in the mine drift and haulage drift were chosen to record the data. The airflow velocities were recorded by using a hand-held anemometer and a real-time PM concentration monitor was used to record the data on the monitoring points. Afterwards, Ansys-Fluent was selected to conduct numerical simulation. A computational geometry domain of the mine drift and haulage drift was constructed based on the dimensions measured during the field visit. Subsequently, the distribution of computing domain in small finite volume cells (mesh) was carried out and the boundary conditions were assigned. The Eulerian-Lagragian model was selected to simulate the airflow velocities and particle trajectories in the computational domain. Following that, the numerical simulation model was validated by comparing the results with field experiment. An allowable limit of less than 15 % of relevant error was selected to validate the numerical model. After achieving the validation criteria, the numerical simulation was evaluated, and conclusions were drawn as per the objectives of this study.

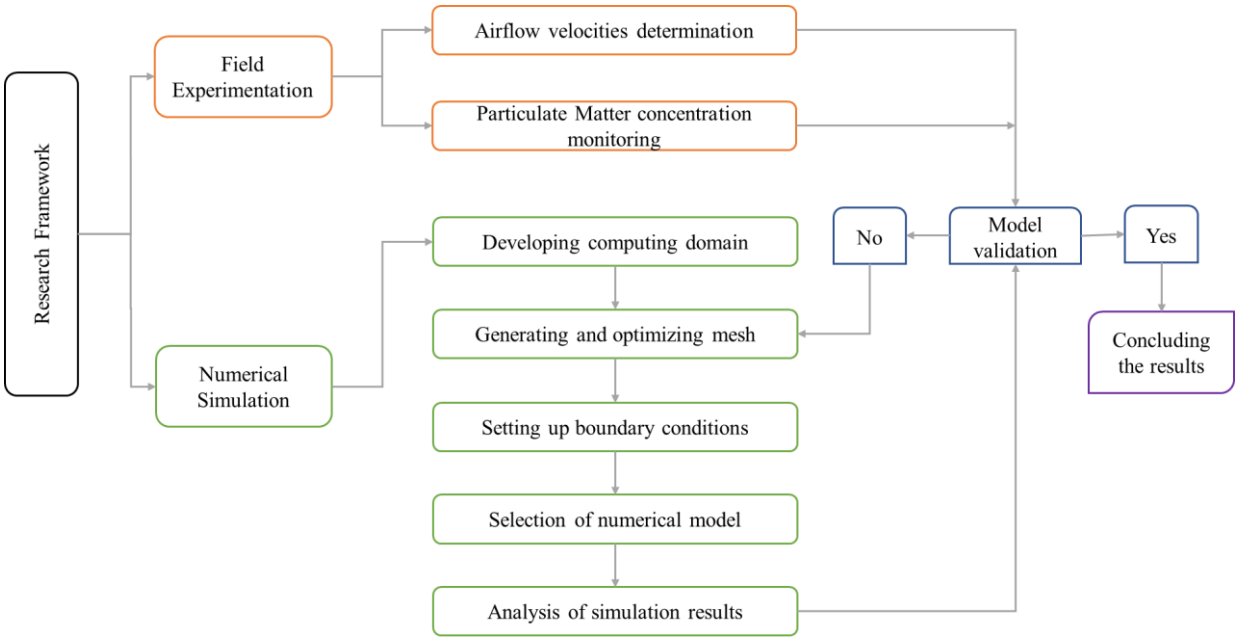

Fig. 1. Research framework overview

1.6. Practical significance

The practical significance of this research study can be expressed as follows:

- This research will assist in identifying the importance of different airflow regions developed in the underground mine. These airflow regions play a pivotal role in the transposition of PM concentrations. The mining professionals will gain valuable insights into the development of airflow regions at different locations and operating conditions to estimate the behavior of PM migration in those regions of the underground polymetallic mines.
- This investigation will enhance the understanding of the regular PM levels found in conventional underground metal mining by offering a thorough database of transient PM concentrations at the mine drift and haulage drift of the underground mine. This information will help in properly interpreting and controlling PM levels.

- This research is pioneering effort to determine the PM concentration produced from multiple sources in the underground metallic mine. Previously, researchers considered DPE exhaust as the only source of PM produced in the underground coal mines. Considering the correct sources of PM generation will reveal the actual PM concentrations threaten the miners' health in underground polymetallic mine.
- This study is the first attempt to adopt DDF-AVS in the mine drift to analyze the behavior of PM migration and dilution under different operating conditions.
- This research is pioneering in assessing whether the volumetric airflow in underground mines selected based on the number of diesel engines working in the mine is sufficient to ventilate the mine drift while PM is produced from multiple sources in the underground polymetallic mine.
- Finally, this research study proposes a novel PM ventilation model, based on spatial-temporal diffusion modelling of PM emitted from multiple sources that will be useful for professionals to integrate with mining operations schedules to minimize the PM exposure to miners.

1.7. Structure of the thesis

This dissertation is structured into six sections to facilitate understanding. Section 1 presents the research background and articulates the problem statement, highlighting the anticipated scientific and industrial contributions. Section 2 offers a critical review of the literature relevant to this research. Section 3 elaborates on the methods and materials employed in conducting the research. Section 4 analyzes the impact of airflow quantity and the influence of DDF-AVS design on PM diffusion. A detailed discussion is conducted in section 5. Section 6 discusses the limitations of this work and recommendations for future work. Finally, Section 7 summarizes the conclusions drawn from this research.

2. Literature Review

2.1. Introduction to PM

Air pollution associated with PM is an escalating global concern [45]. The amalgamation of airborne PM and gaseous pollutants can directly affect human beings, influencing both living conditions and health. Human activities, such as mining, result in health and safety concerns for workers, along with environmental challenges [46, 47]. Dust and PM are generated at several stages of mining activities, including excavation, transportation, and mineral processing [48]. These processes emit particles of varying sizes, from coarse to ultrafine, which can remain airborne for prolonged durations, contingent upon their size and mass. Exposure to such PM can result in respiratory issues, including intensified asthma, bronchitis, and other respiratory illnesses. The tiny particles, specifically PM2.5 (PM with an aerodynamic diameter of $\leqslant$2.5 μm), can infiltrate the lungs and potentially reach the circulation, leading to cardiovascular complications and aggravating pre-existing health disorders.

Furthermore, the amalgamation of PM with gaseous contaminants such as sulfur dioxide (SO_2), nitrogen oxides (NOx), and volatile organic compounds (VOCs) can lead to the generation of secondary pollutants, including ozone and smog [49]. These secondary pollutants enhance health concerns, leading to breathing problems and cardiovascular disease among populations living near mining sites or in regions with elevated human activities. The mineralogical and chemical characteristics, along with the mass and surface area of dust particles, directly influence health, resulting in conditions such as lung cancer, bronchial asthma, chronic bronchitis, pneumoconiosis, pulmonary tuberculosis, occupational asthma, chronic obstructive pulmonary disease, dust-related fibrosis, cardiovascular disease, cerebrovascular disease, and gastric cancer [50]. Thus, to control the PM health impact on humans, Occupational Safety and Health Administration (OSHA) proposed 10 mg/m^3 and Mine Safety and Health Administration (MSHA) established DPM exposure threshold of 0.16 mg/m^3 (quantified as total carbon) for underground metal and nonmetal mines, as a Time Weighted Average (TWA) for Personal Exposure Limit (PEL) to PM under a single 8-hour shift [51-54].

2.2 PM and health effects

Since the research conducted by Dockery et al. [46], PM has been strongly associated with negative health outcomes, revealing a significant correlation between PM levels and fatalities across six U.S. cities with varying average pollution levels. In multiple ways the PM has impacted human health. For instance, PM has been associated with cardiovascular diseases, pulmonary illness, diabetes, and neurological disorders [55, 56]. Despite the undeniable facts about the adverse health impacts of fine particle pollution, the specific characteristics of the particles responsible for these implications remain ambiguous. The adverse health impacts are typically associated with PM mass concentration [57, 58]. Current guidelines concerning PM emissions predominantly rely on the mass concentration of particles [59]. The relationship between early mortality and PM concentration differs by location, equivalent PM concentrations result in distinctly fewer

premature fatalities in China compared to Europe [60]. This development underscores the necessity of determining which sources of PM emissions are more detrimental than others.

The health implications of particles can generally be assessed with two distinct methodologies. Epidemiological studies examine the correlations between fine particle concentrations and health effects at the population level. Toxicological investigations examine the direct results of particle exposure either in animal subjects or in cell exposure.

2.2.1 Toxicological studies

The toxicological investigations underscore the significance of aerosol composition and origins in the health impacts of particles. Park et al. [61] conducted a study that ranked the toxicity of PM from various sources based on oxidative potential measurements and in vitro cellular exposures. Research indicated that PM originating from combustion sources exhibited greater toxicity compared to that from non-combustion sources, particularly emphasizing the harmfulness of traffic-related aerosols, as diesel and gasoline engine emissions were identified as the most toxic contributors. Additional examined sources included biomass and coal combustion, as well as road dust comprising ammonium sulfate, ammonium nitrate, sea spray, and secondary organic aerosols. Therefore, the PM emitted from diesel engines has significance as compared to the other sources of PM to have higher worsen health effects.

A substantial number of animal experiments have been conducted to assess the potential health impacts of prolonged DPM exposure. Heinrich et al. [62] performed a series of tests with rats, mice, and hamsters subjected to both unfiltered and filtered diesel particulate matter to investigate its carcinogenic potential. All the test subjects were 8 to 10 weeks old prior to exposure. The exposure duration was 19 hours per day, five days per week. The longest exposed durations for mice, rats, and hamsters were 120, 140, and 120 weeks, respectively. The amount of unfiltered DPM in this investigation was around 4 mg/m^3. Each batch comprised 96 animals. A clean air exposure chamber was utilized for the control groups, which had an equivalent sample size. A significant incidence of lung tumors in rats (18%, 17/95) was detected following prolonged exposure to DPM, in contrast to the control group (0%, 0/96). Similarly, Mauderly et al. [63] performed a cancer prevention investigation on rats exposed to soot (a principal component of DPM) at high, moderate, and low concentrations (0.35, 3.5, 7.0 mg/m3, respectively) for a duration of up to 30 months (7 hours per day, 5 days per week). The findings indicated that the incidence of lung tumors in the high and intermediate exposure groups was 13% and 4%, respectively, surpassing the control group's rate of 1%.

Animal research has produced significant findings and data from experiments supporting the positive association of DPM exposition and detrimental health effects. While prolonged exposure to DPM may lead to lung tumors in humans, this does not imply that the dose-response data from rat carcinoma research is relevant to humans. Numerous investigations indicated that lung overload resulted in an elevated incidence of lung tumors in rats [64-66]. The clearance and load function of lungs in humans much exceeds that found in rats. The deposition of DPM in the lungs varies across animals and people, even when exposed to the

same dosage of DPM. Therefore, using the DPM exposure dose from laboratory animals as a benchmark for human DPM exposure is unsuitable [67]. Consequently, several occupational investigations have been undertaken, yielding epidemiological information pertinent to the correlation between DPM exposure and lung cancer risk.

2.2.2. Epidemiological studies

In 1986, NIOSH released a report that encompassed several animal experiments and epidemiological investigations about the health risks of prolonged exposure to DPM. In 1988, NIOSH re-evaluated the data from the 1986 report and determined that prolonged exposure to elevated quantities (exceeding 4 mg/m3) of diesel exhaust could substantially heighten the risk of lung tumors in the tested animals. Nevertheless, only two epidemiological research referred to in the work demonstrated that the lung cancer mortality among train workers escalated with prolonged exposure to DPM emissions [68, 69]. NIOSH recommended that DPM may have carcinogenic effects on humans, based on ample animal research and scant epidemiological evidence [70]. In 1988, the IARC convened a review conference with a panel of specialists to assess the health implications of DPM exposure. Consistent with the NIOSH guideline, the IARC designated DPM as a potential human carcinogen (category 2A) [71]. The review primarily assessed over ten study groups pertaining to various industries (railroad workers, drivers, and miners) and case-control studies associated with many diseases (lung cancer, bladder cancer, etc.). However, the correlation between prolonged DPM exposure and lung cancer incidence could not be established due to insufficient evidence from epidemiological research. In 2012, IARC conducted a subsequent study after 24 years, following the initial review in 1988. A significant outcome of this research was the reclassification of DPM as carcinogenic to humans (Group 1), as documented in a report published in 2013 [72].

Several epidemiological studies involving various work titles, as examined in the IARC assessment, presented substantial proof of the cancer risk of DPM [72]. Garshick et al. [73] determined that the relative risk (RR) for lung tumor fatality among long-term exposed railroad workers was 1.40 (95% CI: 1.30–1.51) in comparison to personnel without frequent exposition to DPM emissions. This study did not account for smoking history, a potential confounding variable affecting the results. Consequently, Garshick et al. [74] performed an additional trial with adjustments for smoking history. The study results indicated that the RR of lung cancer was 1.22 (95% CI: 1.12–1.32) when adjusted for smoking history and 1.35 (95% CI: 1.24–1.46) while not adjusted. The findings indicated a minor variation in the risk of lung cancer death after accounting for smoking history. The substantial sample size and extended duration of this investigation facilitated the derivation of credible results. Comparable findings were also observed in epidemiological investigations including workers in the trucking industry, construction sector, and other domains associated with DPM exposure [75-79].

Compared to other industries, underground miners encounter elevated amounts of DPM due to confined operational spaces and inadequate ventilation. In the previous decade, only three epidemiological studies on underground mining have been undertaken, all indicating a significant correlation between prolonged exposure to DPM and an increased risk of lung cancer. A cohort mortality study [80] analyzed 12,315

miners from eight non-metal mines in the U.S. where all the miners worked for over a year during the utilization of diesel equipment. Mortality statistics were monitored until 1997, employing respirable elemental carbon (EC) as a substitute for DPM. Exposure estimates were derived from personal respirable elemental carbon (REC) measurements collected between 1998 and 2001, with historical REC concentrations extrapolated from this data. The study considered characteristics including sex, work titles, and birth dates, but did not include data of smoking history. The findings revealed average DPM values of 1.7 μg/m³ for surface miners and 128.2 μg/m³ for underground miners. The RR of cancer-related fatality was 1.21 (95% CI: 1.01–1.45) for underground miners and 1.33 for surface miners. When average DPM being exposed above 946 μg/m³ yearly, the RR for underground miners elevated to 2.21 (95% CI: 1.19–4.09). The data indicates a greater lung cancer fatality risk in underground miners relative to surface miners, along with a trend of escalating risk associated with extended exposure to DPM.

Silverman et al. [81] expanded upon the previous cohort study by conducting a nested case-control study utilizing the same group of miners as the research sample. This study included additional variables, such as smoking history and prior respiratory disease, while still supporting the findings of Attfield et al. [80]. The findings demonstrated that the risk of lung cancer mortality escalated with extended exposure to DPM (15year lag), independent of smoking status. Underground miners with extended exposure to high levels of diesel particulate matter (≥15 years) exhibited an exponential rise in the risk of lung cancer mortality relative to surface miners exposed to lower concentrations.

Another cohort study [82] involving 5,862 German potash miners, conducted from 1970 to 2001, investigated the association with DPM exposition and lung cancer fatality. Total carbon (TC) served as a substitute for DPM, with cumulative diesel exposure assessed by multiplying TC concentrations by the duration of miners' exposure. Smoking history was considered an influencing factor. The standardized mortality ratio (SMR) for lung cancer in the entire cohort was 0.73 (95% CI: 0.57–0.93). In sub-cohorts with a cumulative DPM exposure of 4.9 mg/m³-years, the SMRs were 1.28 (95% CI: 0.61–2.71) and 1.50 (95% CI: 0.66–3.43), respectively, when compared to the low-exposure group, with adjustments made for smoking. The results indicated a positive correlation between DPM exposition and lung cancer fatalities, with risk escalating over time.

Consequently, both toxicological and epidemiological studies clearly indicate a positive correlation between prolonged DPM exposure and an elevated risk of lung cancer. Despite minimal research explicitly targeting underground miners, a substantial association has been demonstrated between extended exposure to elevated DPM concentrations and increased lung cancer mortality. Considering that underground DPM levels surpass those in other work environments, additional research is required to investigate this occupational group more thoroughly. Furthermore, the possible interaction between DPM and other airborne pollutants, such as dust, must be recognized, as these contaminants may exacerbate negative health outcomes.

2.3. Sources and monitoring of PM

Prior research on PM in underground mines has concentrated on mining operations producing mechanical dust, which can result in elevated mass concentrations in areas close to working face and processing plant [83-86]. The impact of DPM on mine environment, fine particulate concentrations, and occupational exposures has been extensively studied [87-90]. A prior investigation in an underground gold mine demonstrated that DPE exhaust accounts for 78%–98% of the PM2.5 mass and over 90% of the PM2.5 carbon concentration [7]. It has been proposed that DPM concentrations in deep mines can be diminished by up to 95% with the utilization of contemporary exhaust after-treatment systems [91].

2.3.1. Shift-average monitoring technique

Earlier in underground mines, the NIOSH 5040 method was used to identify and control the DPM levels. This method is the recognized standard and is regarded as the most precise approach for assessing miners' DPM exposure [92]. This method is extensively employed to assess DPM exposure due to its reduced susceptibility to influence from mineral sources or other combustibles, and its ability to distinguish between organic and elemental carbon (OC and EC) content. Nonetheless, the NIOSH 5040 method is predicated on shift averages and, like other shift-average measurement techniques, it possesses certain limitations. A shortcoming of the approach is the delay between measurement and result reporting, necessitated by the requirement for processing in a specialized laboratory. This delay may extend beyond two weeks in certain instances, potentially leading to excessive exposure of the miners to DPM. Another limitation is its ability to identify increased DPM levels during brief yet critical intervals. The approach is essentially deficient in assessing DPM transients during measurement. This method complicates the assessment of the impact of variations in DPM levels in the mine environment due to alterations in mining activities, as it may necessitate the collection of multiple air samples from mine. This escalates the time and expenses associated with the DPM monitoring procedure [93].

2.3.2. Real-time monitoring technique

Currently, PM and EC concentrations in underground mines are being monitored using real-time measuring equipment [94, 95]. Mischler et al. [96] examined many DPM measurement techniques and determined that the TEOM monitor produced elevated EC concentrations compared to the usual sampling procedure. Arnott et al. [97] quantified DPM concentrations in Nevada gold mines using the NIOSH 5040 method and real-time monitoring techniques. A photoacoustic monitor was employed to quantify Black Carbon (BC), while a DustTrak nephelometer quantified total scattering PM with submicron sizes (dPM_1). Based on the NIOSH 5040 approach, BC (photoacoustic monitor detection) and dPM_1 (DustTrak nephelometer measurement) represent EC and TC, respectively. The TC and EC values derived from the NIOSH 5040 technique were approximately 50% of the corresponding values obtained from real-time DustTrak nephelometers and photoacoustic monitors. Arnott et al. proposed that in mine analysis of real-time BC and dPM_1 measurements utilizing photoacoustic and DustTrak sensors should be calibrated to yield findings consistent with equivalent EC and TC measurements as per the NIOSH 5040 standard for compliance purposes.

Numerous researchers [98-101] documented assessments of DPM in various Australian coal mines utilizing a real-time-modified personal dust monitor alongside the NIOSH 5040 approach. The real-time DPM monitor (D-PDM) was created based on the Personal Dust Monitor (PDM). “Thermo Fisher Scientific” structurally modified the PDM monitor to make it a submicron (under 1 micron) real-time DPM monitor. A cap light, sample intake, belt-mounted enclosure with respirable dust cyclone, sampling and mass measurement instruments, and charging and communication module for monitor-to-computer data transfer are PDM's main components. PDM data is immediate and quantifies particle mass. PDM findings are less sensitive to water spray droplets than optical approaches. [98]. The Pittsburgh Research Laboratories of NIOSH have conducted a laboratory test of the proposal to convert PDM into D-PDM. The chosen submicron size-selective inlet for the prospective field D-PDM instrument was the BGI 1 μm sharp-cut cyclone. The D-PDM instrument was in the prototype phase. Gillies and Wu [98] established a link between D-PDM mass concentration and TC and EC derived from the NIOSH 5040 technique, identifying a unique correlation equation for each mine. The discrepancies in correlation equations were presumed to arise from inter-mine variations in factors such as atmospheric contamination levels (dust and DPM), vehicle fleet composition, fuel type, engine maintenance, combustion efficiency, engine performance, and interference from other submicron aerosols. Multiple mine-specific and combined linear correlations with zero intercept and strong correlation coefficients were identified.

Takiff and Aiken [102] employed an ICx real-time DPM monitor to assess DPM on a vehicle. This monitor was created by the Respiratory Hazards Control Branch at the NIOSH Pittsburgh Research Laboratory [103, 104] and was later licensed to ICx Technologies. The ICx real-time DPM monitor was employed to assess the EC component of the DPM. Takiff and Aiken elucidated the operational principle of the licensed iteration of a beta prototype of the real-time EC monitor, provided by ICx Technologies, and conducted DPM measurements in a commercial mine. They concluded that the real-time ICx DPM monitor accurately mirrors the results of the NIOSH 5040 method in underground mines and is capable of effectively determining real-time DPM concentrations in such environments.

Noll et al. [105] evaluated the efficacy of three portable devices: a PDM produced by Thermo Scientific, a prototype EC monitor (Airtec) developed by FLIR, and a prototype AE91 instrument from Magee Scientific. The instruments were assessed for their capacity to deliver direct reading tailpipe analysis for DPM. The average biases of the tailpipe results from the PDM and Airtec were discovered to be 3 ± 12% and 4 ± 20%, respectively. In comparison to the conventional approach of measuring tailpipe particle concentrations from diluted exhaust. The AE91 data exhibited a robust correlation with the reference technique. Their findings indicated that these measures would allow mine operators to assess tailpipe concentrations at any site within the mine, facilitating the quantification of engine repairs, modifications, and the identification of cars with the highest DPM emissions. Nonetheless, there are certain limitations to using these technologies for tailpipe concentrations, such as the need that sample collection by Airtec to be undertaken for only 30 seconds when the engine operates at low loads. The PDM offers total DPM mass, whereas the AE91 and Airtec are limited to providing EC concentrations exclusively. A significant

disadvantage of this study was the restricted amount of data points and engines utilized; hence, further data encompassing a greater variety of engines and testing facilities are required for enhanced certainty and confidence. More substantial engines must additionally undergo testing due to their potential to generate distinct airflow in the exhaust.

Noll and Janisko [106] assessed the possible disruptions of dust, humidity, and oil mist on the accuracy of the FLIR Airtec monitor in limestone and granite mines. They determined that when accounting for spatial variability, the FLIR Airtec measurements were comparable to the NIOSH 5040 technique values. The findings of the research conducted by Noll and Janisko indicated that dust and elevated humidity did not influence the FLIR Airtec readings when an impactor was employed. They determined that, in addition to the recognized potential interferences, the existence of certain submicron particles in the monitoring environment could introduce a bias in the FLIR Airtec readings.

Gillies et al. [107] examined several ambient monitoring approaches employed in underground mines and determined that real-time DPM ambient monitoring is increasingly recognized as an engineering tool for optimizing DPM management tactics. Khan and Gillies [108] employed the commercially available FLIR Airtec in conjunction with the NIOSH 5040 technique to ascertain DPM concentrations in both metal and non-metal mines, subsequently identifying significant DPM sources. In metal mines, front-end loaders and dump trucks were the primary generators of diesel particulate matter (DPM), while in non-metal mines, load-haul dumps were the principal contributors to DPM [108]. Khan and Gillies [109] reported preliminary results from a study conducted in a mine utilizing high-percentage biodiesel, observing that the TWA EC values recorded by the FLIR Airtec monitor were typically greater than those obtained through the NIOSH 5040 method. According to the first results, researchers established a correlation equation for TWA EC readings taken using the FLIR Airtec and NIOSH 5040 instruments [109]. While the initial research indicated a potential bias in the TWA EC readings of the FLIR Airtec, the findings of that study were derived from insufficient evidence.

Farzaneh et al. [110] analyzed the amounts of diesel particulates at five locations during the operational periods of an underground mine in Kazakhstan. Real-time monitoring of particle number concentration (PNC), lung deposited surface area (LDSA), and concentrations of PM_1, $PM_{2.5}$, and PM_{10} were performed in the mining operational area and the loader driver's breathing zone within the cabin. The findings indicated that most particles fall within the sub-100 nm range. The concentration levels of PM_1 and $PM_{2.5}$ in the loader cabin area (LA) and operating area (OA) of the mine were comparable due to the uniform dispersion of particulate matter during the mine's operational phase. The primary source of PM_1 and $PM_{2.5}$ was the diesel engine, whereas the low LA/OA ratio for PM_{10} indicated that the source of the coarse particles was dust resuspension in the vicinity of the loader cabin.

Sabanov et al. [86] analyzed PM and LDSA concentrations in oil shale underground mine operations. A real-time particulate matter monitor (DustTrak DRX) and a multimeric fine particle detector (Naneous Partector 2) were utilized for field data collecting during loading and dumping operations of a diesel engine

loader. The investigation of PM, LDSA, particle surface area concentration (SA), average particle diameter (d), PNC, and $PM_{0.3}$ produced some useful association factors. Diesel exhaust emissions caused an average increase in LDSA concentration during loading, which reduced during dumping. The concentration of PM1 was lower during loading and increased during the dumping procedure. Similarly, while loading, an average larger particle diameter was identified, whereas dumping, an average smaller one, was observed. The relationship between PNC and particle diameter shows an approximate split between DPM and oil shale dust sizes.

These experimental research studies provided insight into the composition, characteristics, and concentrations of hazardous materials. However, the scope of these studies is limited in the visualization of PM migration, dispersion, and dilution. To visualize PM transition, dispersal, and dilution and to reduce environmental intricacies and measurement limitations, the computational fluid dynamics (CFD) modelling has been employed in many studies. The use of CFD can assist in realizing the new designs of airflow ducts, mine tunnels and mine ventilation systems.

2.3.3. CFD analysis of PM

CFD simulation has been effectively employed in mining investigation to identify spontaneous combustion and implement inert gas in gob regions [111, 112], examine gas concentrations and airflow dynamics in continuous mining operations [113-116], analyze dust issues and devise dust management systems for underground and open-pit mines [117-120], and enhance the design characteristics for mineral processing [121]. CFD modeling has emerged as a potent instrument for comprehending airflow dynamics, gas behavior, and dust behavior within a complex three-dimensional environment. It can also furnish valuable insights for preliminary proposal assessment and regulatory appraisal. A major limitation associated with CFD is the validation of the simulation with experimentation.

The following research studies adopted a combination of experimental and numerical simulation methodologies. Ping et al. [24] addressed the DPM pollution issues and improved the auxiliary ventilation system at a development face in an underground mine in Western Australia, using it as a physical model, while CFD was performed to assess airflow characteristics and DPM concentration distributions in the development face. The acquired simulation findings were verified using real-time measured data. The variations of DPM concentrations across three scenarios, featuring varying duct lengths, were subsequently compared to the AIOH standard for DPM (0.1 mg/m^3). The findings indicated that the existing auxiliary ventilation system was ineffective in significantly reducing DPM concentration, but a ventilation system with a duct length 5 m longer than the current design demonstrated superior DPM dilution efficacy.

In another study, Zeng et al. [122] developed 3D numerical model of DPM dispersion within a single straight entrance for LHD performing loading and hauling operations utilizing ANSYS FLUENT. The loading procedure was conducted for a duration of 3 minutes. The dynamic mesh method in FLUENT was employed to analyze the effect of truck movement on DPM distribution. The resultant DPM distributions are provided for the scenarios in which the vehicle was moving upstream and downstream of the loading

face. The analysis showed intriguing phenomena, including the piston effect, stratification of DPM in the roof area, and the recirculating of diesel exhaust against ventilation. The modeling results can ascertain whether the regions within the face area and straight entry above the existing U.S. regulatory threshold for DPM concentration (>160 μg/m^3).

Xu et al. [87] conducted a research study in an isolated area of an underground mine in the U.S., which served as the physical model for their investigation. CFD was employed to analyze the dispersion of DPM under two different operating conditions. The researchers utilized a discrete phase model to represent DPM, which demonstrated a superior alignment with experimental data compared to studies that treat DPM as a continuous phase. Elevated concentrations of DPM were observed in both scenarios. The authors suggested that this methodology could be effectively used to optimize the ventilation system.

Liu et al. [26] adopted an integrated approach of numerical simulations and field measurements to investigate the displacement patterns of PM emitted by a trackless rubber-tyred vehicle (TRTV) at idle speed for 60 seconds under varying movement conditions, as well as the dilution effects of the ventilation rate on PM. The results indicated that under varying mobility conditions, the PM predominantly transmitted along the roadway floor, although exhibited overall upward diffusion patterns, signifying that the chambers are situated in high-risk zones. Additionally, the dilution effects of the elevated ventilation rate on PM were examined. The ideal dilution ventilation rate was determined to be 4600 m³/min for condition 1 and 2800 m³/min for condition 2.

Duan et al. [25] investigates the diffusion and distribution of DPM by CFD numerical simulation, conducting a numerical modeling of airflow and the DPM field at the heading face of an underground coal mine. The findings indicate that between 15 s and 60 s, DPM consistently builds in the blind zone of airflow and on either side of the monorail locomotive, with concentrations exceeding 1.2×10^{-7} kg/m^3. The DPM cloud at that moment extends 60 m horizontally and has a distribution pattern characterized by elevated levels in the center and diminished levels on either side. At 90 s, a portion of DPM dissipates to the roadway outlet. At that time, along the entire roadway, starting 23 m from the heading face, the concentration of DPM significantly increases, reaching a peak of 2.91×10^{-7} kg/m³ at 33 m. Following this peak, the concentration begins to decline gradually.

Zhou et al. [31] employed a numerical modeling approach to examine the effects of air suction volume (Q) and the distance (L) between diesel vehicles and head-faces on the diffusion patterns of DPM, CO, and NOx during long suction and short pressure ventilation. The results indicated that for L = 20 m, the diesel vehicle is positioned nearer to the suction air duct. At this stage, when Q = 600 m³/min, the tail gas control efficacy in the roadway is at its peak. Furthermore, with L = 40 m, the diesel vehicle is positioned centrally on the roadway. At this point, when Q = 300 m³/min, the tail gas control efficacy in the roadway is at its peak. When L = 60 m and Q = 200 m³/min, the predominant ventilation type in the roadway is pressure-in ventilation. The higher and medium NOx concentration zones within this air volume are minimal.

Liu et al. [123] investigated the transportation of CO and PM released by diesel vehicles under three operational scenarios was examined using CFD numerical modeling and field measurements. The concentrations of CO and PM varied with alterations in the airflow field across different operational conditions, exhibiting an overall consistent distribution. Despite the differing migration patterns of CO and PM under various operational settings, CO at elevated concentrations ($C \geqslant 44.74$ ppm) and PM at high concentrations ($C \geqslant 89.47$ mg/m^3) were predominantly located in proximity to the exhaust pipe of the diesel vehicle.

Liu et al. [124] investigated the spatiotemporal distribution of PM in the exhaust of two diesel vehicles. The authors used a combination of CFD numerical simulations and field data collection. The investigation contained two operating scenarios (OS): both vehicles moving into the wind (OS-1) and moving with the wind (OS-2). The results demonstrated that in both circumstances, the airflow velocity between the two vehicles displayed a circumferential distribution, and an airflow vortex was generated in the chamber due to wind coupling. When vehicles traveled in the same direction against the wind, PM with a concentration range of 15.79–26.32 mg/m^3 could ascend to the height of the human respiratory zone and was predominantly dispersed on the eastern side of the roadway. Furthermore, the PM concentration in the vicinity of the driver's position exceeded the human exposure limit, necessitating personal protective equipment for the drivers. As vehicles traveled in the same direction as the wind, the concentration of PM on the airflow outlet side significantly increased over time, particularly for PM within the concentration range of 21.05–31.58 mg/m^3, in comparison to the airflow inlet side.

A comprehensive literature review in this chapter reveals that PM from the tailpipe exhaust has been a major concern in underground mine environments. Most studies adopted either field experimentation or combining it with numerical simulation as a methodology to understand the PM emission and migration characteristics. To control PM migration, the literature review highlights different control techniques by modifying operating conditions or the existing ventilation system in the mine. The extensive literature review revealed that existing studies primarily focused on DPM in underground coal mines, overlooked PM generated by other mining operations, and did not consider non-coal mines. In most studies, the DPE were idling at a constant speed on the roadway or inside a chamber with or without an AVS system. However, the emission of DPM and PM both depends upon the engine load and mining operation. Usually there is more than one DPE operating in mining areas, but most studies considered only one DPE while exploring the DPM emission and dispersion. The mining areas with dead-ends are equipped with SDF-AVS or DDH-AVS in the existing studies, which are considered insufficient in many cases. This study addresses these research gaps by considering the emission of both DPM from the exhaust tailpipe and PM during loading and unloading of muck in an underground polymetallic mine. There were more than one DPE performing loading and unloading operations in the mining area, depicting the enhanced emissions of DPM and PM concentrations. The impact of existing volumetric airflow and DDF-AVS design on the transposition of DPM and PM was evaluated, and an optimized volumetric airflow and strategic positioning

of AVS outlets of DDF-AVS will be proposed to decrease the residence time of the pollutants in the mining area.

3. Methods and materials

3.1 Introduction

This research study employed a combination of real-time monitoring and numerical simulations to assess airflow characteristics and the distribution of PM. The real-time monitoring conducted in the mine during DPE handling transportation provided crucial information about fluctuations in airflow velocity and PM concentration across various operational scenarios. However, several challenges arose with real-time monitoring, including the necessity to maintain a safe distance between the DPE and data recording personnel to prevent accidents. Additionally, identifying and recording field data required the DPE to remain idle for specific durations, which led to unwanted delays in transportation and subsequent operations.

Furthermore, the numerical data collected from the field lacked the ability to visualize the actual mine site, its operating conditions, airflow characteristics, and PM migration patterns. To address the limitations of real-time monitoring, numerical simulations emerged as a valuable tool, capable of not only recreating actual mining scenarios but also illustrating airflow characteristics and the generation, emission, and transposition of PM within the underground mine section.

However, the accuracy of the simulation model is paramount; it must be validated against real-time monitoring data to ensure its authenticity. Once validated, modifications to the operating scenarios can further enhance the evaluation of airflow characteristics and PM migration, all while mitigating the in-situ risks associated with field operations. This presents an additional advantage of utilizing numerical simulations.

3.2 Mine site description

In this study, the airflow velocity and real-time PM sampling were carried out in an underground polymetallic mine located in the East-Kazakhstan, as shown in Fig. 2. The mine was producing 300,000 tons/year of ore. This study was conducted based on the data collected during a filed visit.

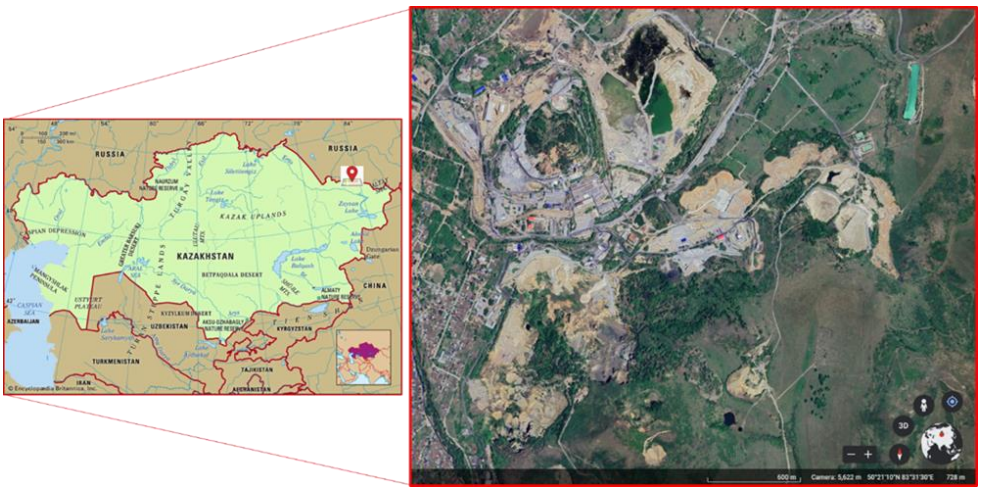

Fig. 2. The approximate location of the polymetallic underground mine in East-Kazakhstan

3.3 Computational model description

The computational model was developed based on field observations. The operating scenarios of DPE inside a mine drift near a working face and a temporary dumpsite, and at a haulage drift were observed, and similar working conditions were developed to simulate the actual underground mine operating conditions.

A 3D computational model was constructed by using Ansys Geometry Space-Claim. The mine drift was 70 m long and featured a rectangular cross-section measuring 4.4 m in width and 4.3 m in height. Additionally, a temporary dumpsite, measuring 12 m in length, 5 m in width, and 4.3 m in height, was situated 20 m from the entrance of the mine drift. The mine drift was equipped with a forced dual duct auxiliary ventilation system. The outlets of ventilation ducts, with a diameter of 0.8 m, were positioned 10 m away from the working face. Two types of DPE were considered in this study, LHD Cat R1700 and UMT CatAD45. The LHD had dimensions of 10 m in length, 2.9 m in width, and 2.5 m in height, with a maximum power capacity of 361hp/269 kW. The exhaust gas outlet of the LHD was at the lower left of the back. On the other hand, the UMT featured dimensions of 11.5 m in length, 3.02 m in width, and 2.8 m in height, with a maximum power capacity was 581hp/433 kW. Mainly, the LHD was operating inside the mine drift, and the UMT was hauling at the cross-section of mine drift and haulage drift. The emissions from both LHD and UMT engines correspond to the Tier 3 engine equivalent. The engine utilizes diesel fuel DT-L-K2 (standard GOST 305–82), which is the first approximation aligning with the Euro 3 standard, differing only in the cetane number.

3.4. Methodology for operating condition 1(OC1)

In operating condition (OC) 1, the airflow distribution and PM dispersion were examined within mine drift and haulage drift during the muck loading and unloading operations of the LHD, without considering the vehicle load. Fig. 3. (a) illustrates the computational model specifications and boundary conditions, which closely resemble experimental field observations. Fig. 3. (b) shows condition 1 (C1) where the LHD was loading muck at the active working face, positioned facing into the wind. Fig. 3. (c) illustrates condition 2 (C2) where the LHD was working perpendicular to the wind to unload muck inside the temporary dumpsite. Fig. 3. (d) shows condition 3 (C3) where the LHD was dumping muck onto the UMT while hauled in the haulage drift, at the entrance of the mine drift, similarly positioned facing against the wind (condition 3).

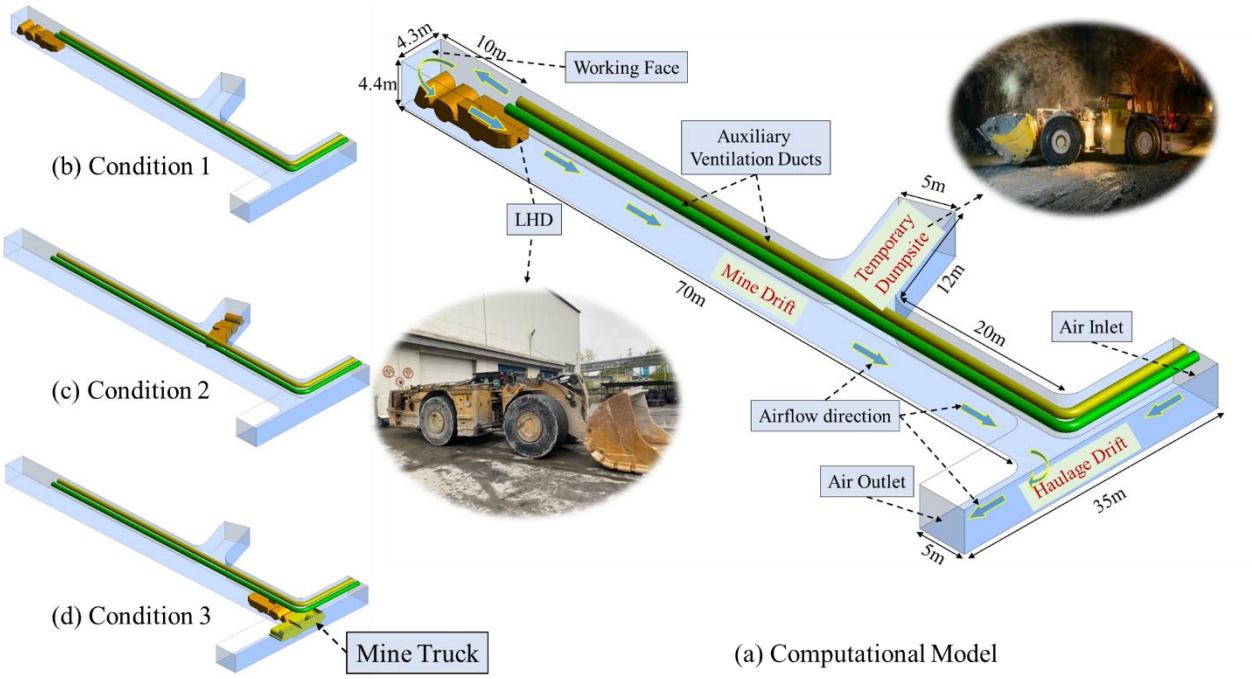

Fig. 3. (a) Computational model of underground mine drift, (b) C1, (b) C2, and (c) C3

3.5. Methodology for operating condition 2 (OC2)

In OC 2, the impact of different DDF-AVS designs was evaluated on the PM dispersion. Fig. 4. (a) shows the geometric model of the underground mine drift and associated characteristics. Fig. 4. (b) depicts the scenario 1 (S1) in which LHD was loading ore near the working face. Fig. 4. (c) highlights scenario 2 (S2) in which LHD was dumping inside the temporary dumpsite. In OC2, the dimensions of the mine drift and temporary dumpsite and the positions of the LHD were similar like OC1, however, only change was between the actual positions and simulated positions of the DDF-AVS outlets.

3.5.1. Assessment of the DDF-AVS designs

The spacing between the center axes of the AVS outlets and their positioning relative to the central axis of the mine drift along the z-axis are two design parameters incorporated in the DDF-AVS system. Figure 4 illustrates various design configurations created to assess the impact of these parameters on the airflow field and the transposition of PM to enhance the DDF-AVS.

In AVS 1, Fig 5. (a), the outputs are positioned 1 m apart, with Vent 1 located 2.4 m from the left wall and Vent 2 located 1 m from the right wall. Fig. 5. (b) illustrates AVS 2, indicating that the outlets are positioned 1.1 m apart, with both vents situated 1.65 m from the corresponding right and left walls. In AVS 3, Fig. 5. (c), the outlets are 2 m apart, with both vents located 1.2 m from the side walls. In AVS 4 Fig. 5. (d), the outlets are located 3 m apart, with each vent located 0.7 m from the side walls.

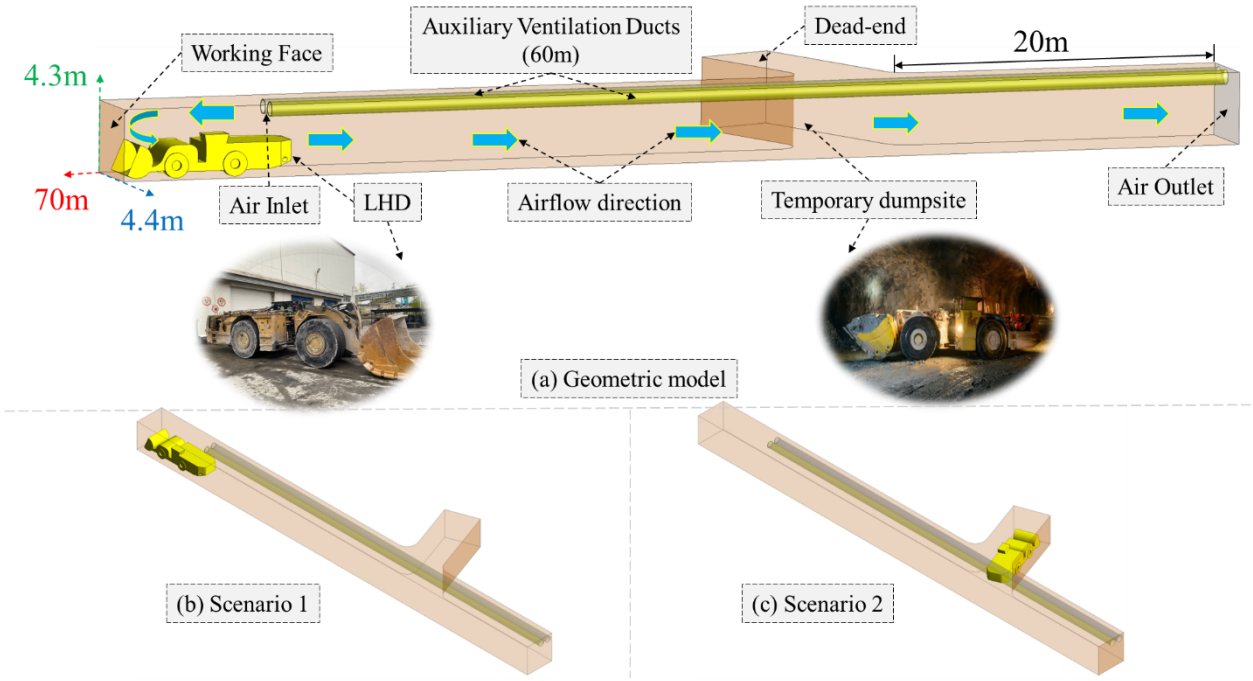

Fig. 4. (a) Geometric model of underground mine drift, (b) S1, and (c) S2

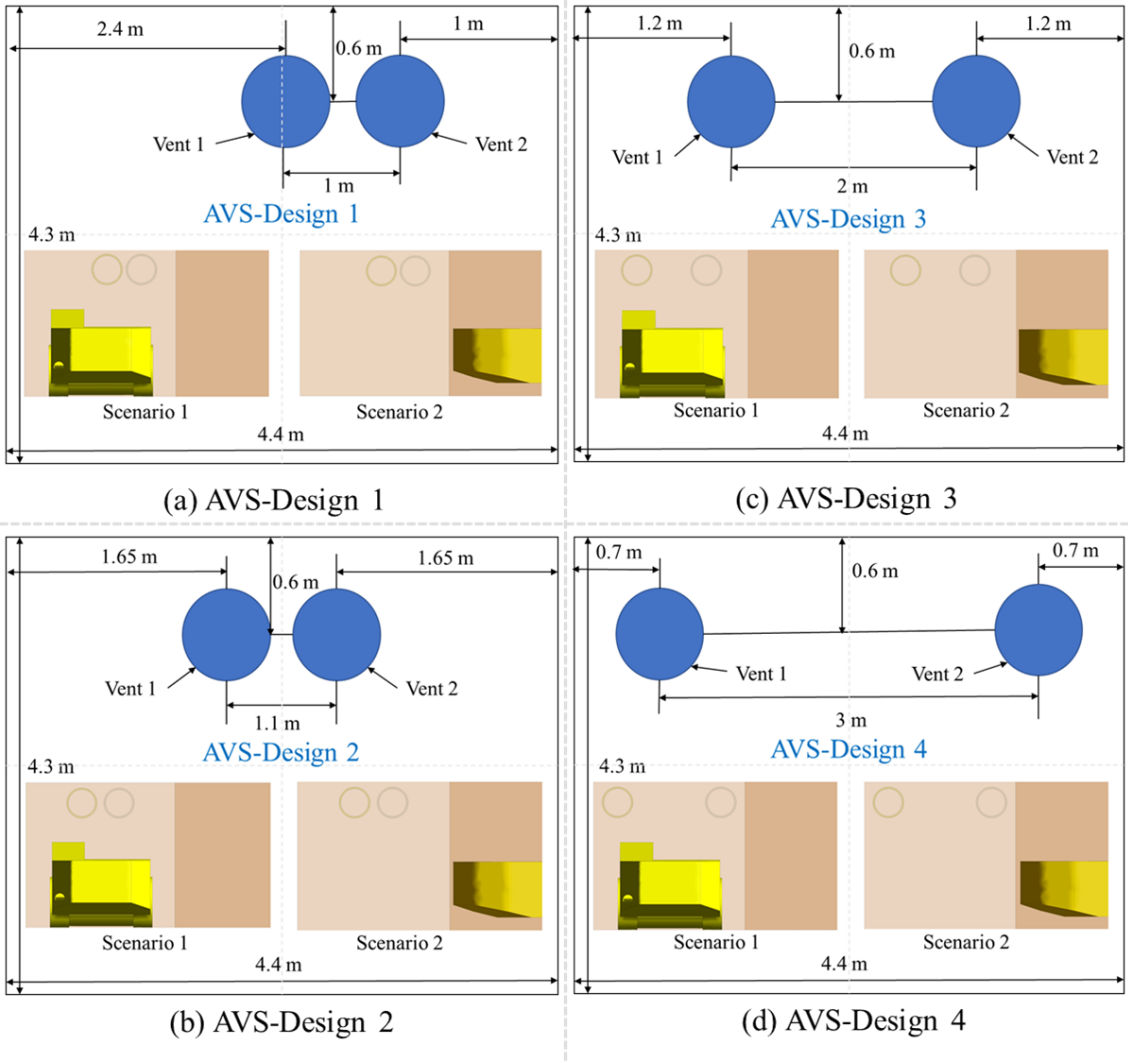

Fig. 5. (a) AVS-1, (b) AVS-2, (c) AVS-3, and (d) AVS-4 for S1 and S2

3.6 Numerical models

In general, two CFD numerical models are available to simulate two-phase flow (airflow and PM) [125]. The selection of numerical scheme usually depends upon the operating environmental conditions and boundary conditions of the computational domain. The first model is referred to as Species Transport, which utilizes a Eulerian-Eulerian (fluid-fluid) methodology. In this approach, both the PM and the airflow are regarded as a continuous phase [126, 127]. The second model is the Discrete Phase Model, which employs the Eulerian-Lagrangian method (particle-fluid) and considers PM as solid particles and airflow as fluid [128-130]. Several simulation-based investigations were undertaken to compare the outcomes of the CFD continuous phase model and the discrete phase model. The authors determined that both models are viable for simulating a solid-gas environment. Nonetheless, discrete phase model exhibits superior concordance with experimental outcomes in comparison to the continuous model [131-133]. Regarding PM, numerical research investigations were undertaken, employing both continuous and discrete phase models to analyze the distribution of diesel PM in the underground mine. They asserted that a superior correlation was established between the experimental results and the continuous phase model. Nonetheless, the computational expense associated with the continuous phase is relatively lower than that of the discrete phase models [27, 134] due to the Species Transport Model's handling of continuous fields. Conversely, the discrete phase models entail the tracking of particle motion and its interaction with fluid and other particles. Consequently, this research employed the Eulerian-Lagrangian methodology to simulate airflow and particulate matter in the subterranean mine.

3.6.1. Fluid flow model

The airflow was regarded as a continuous phase and incompressible fluid. The equations for mass conservation and momentum [135, 136] can be expressed as equations 1 and 2.

$$\frac{\partial \rho}{\partial t} + \nabla.(\rho \vec{v}) = S_m \tag{1}$$

$$\frac{\partial}{\partial t}(\rho \vec{v}) + \nabla.(\rho \vec{v}.\vec{v}) = -\nabla p + \nabla.(\bar{\bar{\tau}}) + \rho \vec{g} + \vec{F} \tag{2}$$

Where, p, $\bar{\bar{\tau}}$, $\rho\vec{g}$, $\vec{v}$, S_m, $\vec{F}$ are the static pressure, stress tensor, gravitational body force, velocity vector, added mass form dispersed phase to the continuous phase and external body forces, respectively.

$$\bar{\bar{\tau}} = \mu\left[(\nabla\vec{v} + \nabla\vec{v}^T) - \frac{2}{3}\nabla\vec{v}I\right]\frac{\partial \rho}{\partial t} + \nabla.(\rho\vec{v}) = S_m \tag{3}$$

Where μ and I are molecular viscosity, and unit tensor.

The standard model of turbulent kinetic energy (k) and dissipation rate (ε) are usually considered to simulate the turbulent flow [137-140].

The k-equation:

$$\frac{\partial(\rho k)}{\partial t} + \frac{\partial(\rho k u_i)}{\partial x_i} = \frac{\partial}{\partial x_j}\left[\left[\mu + \frac{\mu_t}{\sigma_k}\right]\frac{\partial k}{\partial x_j}\right] + G_k - \rho\varepsilon \tag{4}$$

The turbulent viscosity μ_t can be determined as follows:

$$\mu_t = \rho C_\mu \frac{k^2}{\varepsilon} \tag{5}$$

The ε equation:

$$\frac{\partial(\rho\varepsilon)}{\partial t} + \frac{\partial(\rho\varepsilon u_i)}{\partial x_i} = \frac{\partial}{\partial x_j}\left[\left[\mu + \frac{\mu_t}{\sigma_\varepsilon}\right]\frac{\partial \varepsilon}{\partial x_j}\right] + \frac{C_{1\varepsilon}}{k} - C_{2\varepsilon}\rho\frac{\varepsilon^2}{k} \tag{6}$$

Where ρ, k, ε, μ, μ_t, G_k, are the density, turbulent kinetic energy, turbulent energy dissipation rate, laminar viscosity coefficient, turbulence viscosity coefficient, and average velocity gradient, respectively. The constant values of terms $C_{1\varepsilon}$, $C_{2\varepsilon}$, C_μ, σ_k, σ_ε are 1.44, 1.92, 0.09, 1.00, and 1.30, respectively.

3.6.2. Particle flow model

ANSYS Fluent discrete phase model (Lagrangian) predicts the trajectory of particles by integrating the balance force on the particle. The particles are injected as surface source. The DPM is injected from the exhaust tailpipe and the PM is injected from the LHD's bucket surface. This force equates the particle inertia with the forces acting on the particle and can be written as [140, 141]:

$$m_p \frac{d\vec{u}_p}{dt} = m_p \frac{\vec{u}-\vec{u}_p}{\tau_r} + m_p \frac{\vec{g}\,(\rho_p-\rho)}{\rho_p} + \vec{F} \tag{7}$$

where m_p, $\vec{u}$, $\vec{u}_p$, ρ, ρ_p, $\vec{F}$, $m_p \frac{\vec{u}-\vec{u}_p}{\tau_r}$, and τ_r are the particle mass, fluid phase velocity, particle velocity, fluid density, density of the particle, an additional force, drag force, and droplet or particle relaxation time, respectively. The τ_r can be calculated by:

$$\tau_r = \frac{\rho_p d_p^2}{18\mu}\frac{24}{C_d Re} \tag{8}$$

Here, μ, d_p, and Re are molecular viscosity of the fluid, particle diameter, and relative Reynolds number, which can be numerically defined as:

$$\mathrm{Re} = \frac{\rho d_p |\vec{u}_p-\vec{u}|}{\mu} \tag{9}$$

3.7 Mesh generation and sensitivity analysis

The accuracy of the mesh greatly affects the outcomes of the simulation. As a rule of thumb, the simulation's accuracy improves as the mesh density increases. However, the time and resources needed for computing will increase. As a result, this study split the mesh into three groups with varying quantities, and each group's skewness was set to less than or equal to 0.3 [24, 25, 134]. In both, OC 1 and 2 three mesh groups (fine, medium, and coarse) were created to distribute the domain in the mesh elements. In OC 1 the number of elements in each mesh category was around 2.3 million, 1.8 million, and 1.4 million, respectively. In OC 2 the number of elements was around 1.9 million, 1.5 million, and 1.1 million, respectively.

The mesh sensitivity analysis was performed with a mesh ratio maintained at no less than 1.26 [142]. The height of the initial mesh cell was set at 0.02 m, determined by the calculation of dimensionless y+ = 30 [143]. The overall number of prism layers was determined to be 5, with an inflation ratio of 1.2 for each layer. Ansys-Fluent was employed to simulate the airflow in the drift using multiple mesh schemes. CFDPost was utilized to employ line monitors for the calculation of airflow velocity. The line monitors have been defined on the x, y, and z coordinates in the following sequence: L1(x, 1.5, 3.4), L2(x, 1.5, 2.2), L3(x, 1.5, 1), L4(x, 2.2, 1), L5(x, 2.2, 2.2), and L6(x, 2.2, 3.4). Fig. 6. (a) illustrates the outcomes of the mesh independence test, with the blue, red, and black lines denoting airflow velocity in Coarse, Medium, and

Fine Meshes, respectively. The brown, green, and purple bars illustrate the relative error [144] between Coarse and Medium Meshes, Coarse and Fine Meshes, and Medium and Fine Meshes, respectively. Fig. 6. (b and c) show the appearance of surface and volumetric meshes (Medium Mesh) of the computational domain.

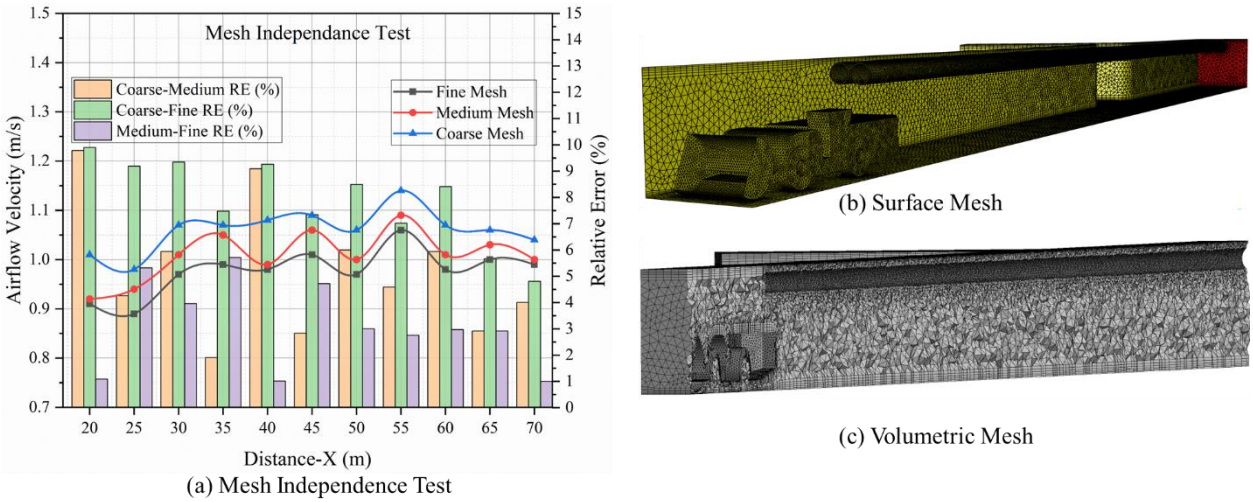

Fig. 6. (a) Mesh independence test, (b) surface mesh, and (c) volumetric mesh

The figure depicts that the variation trend of the airflow field obtained from the 3 meshes is consistent with each other. The simulation results obtained from medium and fine mesh have the same variation trend and the data are nearly similar. Comparatively, the data obtained by the coarse mesh has a considerable deviation. Thus, to gain more accurate simulation results and save computational cost, medium mesh was chosen for simulation.

3.8 Input Parameter setup

After meshing the geometric model, the mesh file was imported into Ansys-Fluent for parameter setting. The details of each parameter and corresponding values are detailed in Table 1.

Table 1. Input parameters and corresponding values of simulation model

Parameter	**Value**	**Parameter**	**Value**
Gravity (m/s^2)	9.81	Minimum particle diameter (m)	1e-6
Air inlet (m/s)	1.2	Median particle diameter (m)	1.75e-6
AVS-DDF 1 and 2 (m/s)	13	Mass flow rate UMT (kg/s)	4.57e-6
Exit boundary type	Pressure outlet	Mass flow rate LHD (kg/s)	3.11e-6
Maximum particle diameter (m)	2.5e-6	Mass flow rate PM (kg/s)	5.67e-5
Solver Type	Pressure-Based	Boundary type of airflow inlet	Velocity-inlet
Boundary type of PM inlet	Mass flow-inlet	Diameter distribution of PM	Rosin-Rammler
Initialization Method	Standard Initialization	Scheme	COUPLE
Turbulent Kinetic Energy	Second Order Upwind	Turbulent Dissipation Rate	Second Order Upwind
Near-wall treatment	Standard wall function	Pressure outlet (kPa)	101.325

As the airflow in the mine drift is low-speed incompressible flow, the solver type in this study was set as Pressure-based, while the scheme of the solution method was set as Coupled. To improve the accuracy of simulation results, the discretization of the momentum, turbulent kinetic energy, and turbulent dissipation rate equations were all set as Second order upwind.

3.9. Layout of measuring points in OC1 and OC2

In all three conditions of OC1, each measuring point was denoted by a number (1 to 6) and corresponding coordinates (x, y, z), as shown in Fig. 7. The measuring points 1, 2, and 3 were aligned with breathing zone at 1.5 m and the measuring points 4, 5, and 6 were established on breathing zone 2.2 m. The measuring points in the mine drift on each cross section were located at 1 (x, 1.5, 3.4), 2 (x, 1.5, 2.2), 3 (x, 1.5, 1), 4 (x, 2.2, 1), 5 (x, 2.2, 2.2), and 6 (x, 2.2, 3.4), respectively.

Similarly, in the haulage drift measuring points distributed as 1 (71, 1.5, z), 2 (72.5, 1.5, z), 3 (74, 1.5, z), 4 (74, 2.2, z), 5 (72.5, 2.2, z), and 6 (71, 2.2, z), respectively. Moreover, the cross-sections selected in C1 were at x = 20, 30, 40, 50, 60, and 70 m, respectively. In C2, the selected cross sections were at x = 10, 20, 30, 40, 50, 60, and 70 m, and in C3, the cross sections were selected at x = 10, 20, 30, 40, 50, and 60 m, respectively. While the selected cross-sections in haulage drift were constant in all three conditions and situated at z = 10, 15, and 20 m, respectively. As mentioned earlier, OC2 is limited to mine drift only and lacks the haulage drift, so the layout of monitoring planes in both scenarios of OC2, Fig. 8. (a and b), follows the similar pattern which was discussed above for OC1.

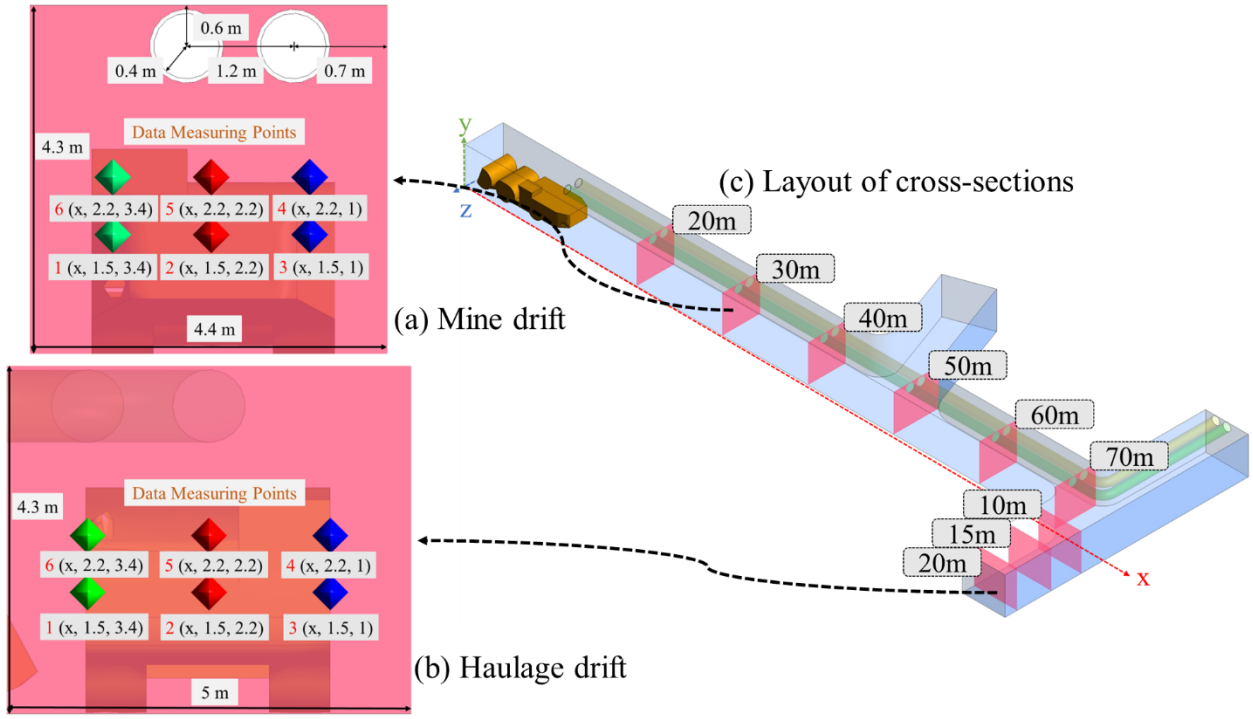

Fig. 7. Distribution of monitoring points in (a) Mine drift, (b) Haulage drift, and (c) layout of the cross sections

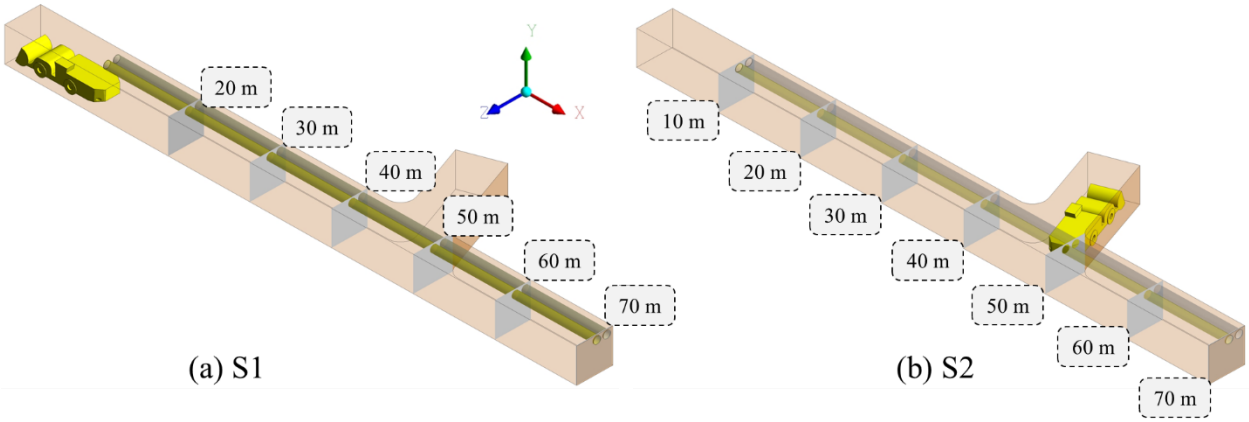

Fig. 8. Data monitoring planes layout in (a) S1, and (b) S2

3.10. Real-time monitoring

Real-time data monitoring in the mine was conducted using various instruments. To capture field data at specific points and cross-sections, the Leica Disto D2 laser distance meter, as shown in Fig. 9. (a), was utilized for accurate distance measurements. Fig. 9. (b) shows the Alnor RVA501 Rotating Vane Anemometer which was used to measure the airflow velocity in the mine. Fig. 9. (c) shows the DustTrak™ DRX Aerosol Monitor 8533 which was used to capture the PM concentrations in the mine. It is capable of simultaneously measuring both mass and size fractions. This multi-channel, battery-operated, data-logging, light-scattering laser photometer provides real-time aerosol mass readings while also collecting gravimetric samples. It is suitable for a range of applications, including indoor and outdoor settings, industrial and occupational hygiene, baseline screening, remote monitoring, and research studies. The device employs a sheath air system that isolates the aerosol within the optics chamber, ensuring cleaner optics for enhanced reliability and reduced maintenance. The flow rate of the DustTrak™ pump was calibrated to 1.7 liters per minute, allowing for simultaneous measurement of size-segregated mass fraction concentrations corresponding to PM1, PM2.5, PM10, and total PM size fractions [145, 146].

(a) Leica Disto D2 (b) Alnor RVA501 (c) DustTrak™ DRX Aerosol Monitor 8533

Fig. 9. Real-time field data monitoring instruments (a) Leica Disto D2, (b) Alnor RVA501, and (c) DustTrak™ monitor

3.10.1. DustTrak filter kit

The DustTrak was fitted with a 37 mm replaceable mesh filter housed within a concealed filter kit in its body. The airflow passes through the air inlet and outlet cavities of the kit, as shown in Fig. 10. (a). A mesh filter is inserted in between the internal filter kit to trap the particles on the mesh filter. Five points were selected on the mesh filter for further analysis of the elemental composition of the particles under scanning electron microscope (SEM), as shown in Fig. 10. (b). This study utilized the SEM 'Jeol JSM-IT200' (JEOL, Freising, Germany), which was integrated with energy dispersive X-ray spectroscopy (EDS), as shown in Fig. 10 (c). A sputter coating layer, measuring 5 mm in thickness, was

applied to the sample filter before it was placed inside the SEM for analysis. The desktop computer connected to the SEM ran the application 'SEM Operation', which was responsible for controlling all aspects of the equipment.

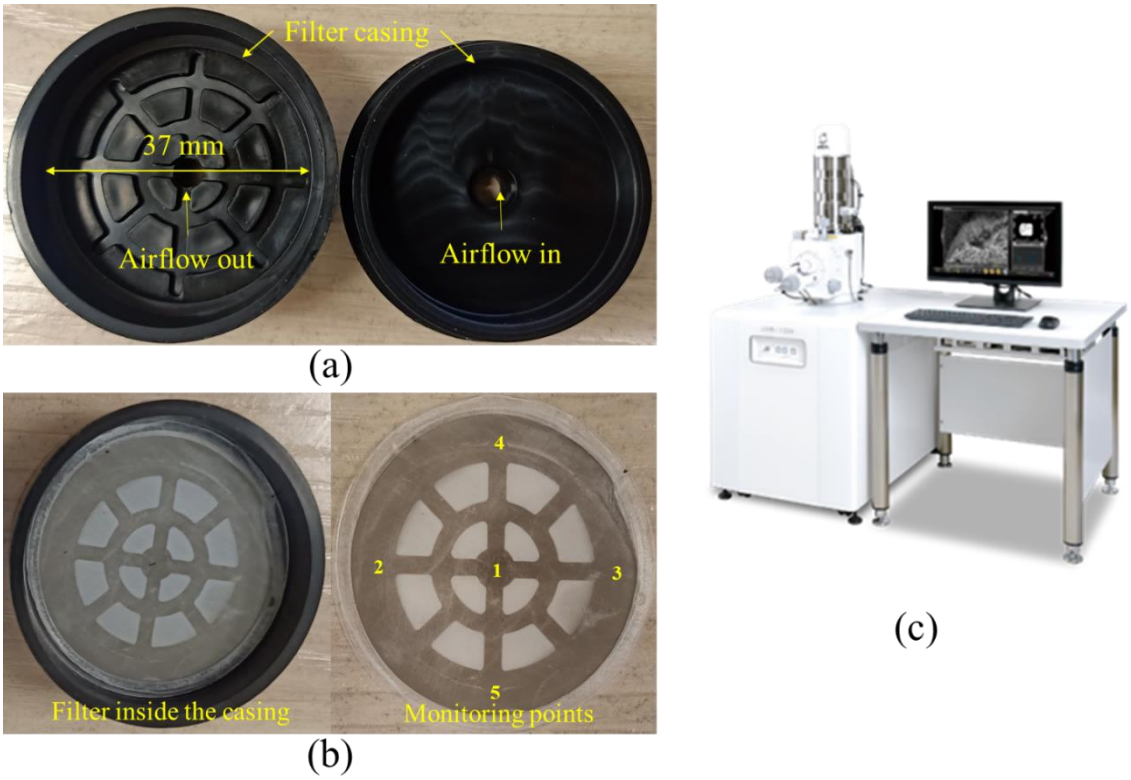

Fig. 10. (a). Internal filter kir, (b) mesh filter and monitoring points, and (c) SEM/EDS Jeol JSM-IT200

3.11. Assumptions

In this study, the exhaust pipe of DPE and muck loading and unloading operation of LHD were considered as the main sources of the PM generation. However, the resuspension of the PM in the breathing zone due to DPE maneuvering was neglected. The PM particles consisted of very small size and volume fraction, and the velocity of PM production due to muck loading and unloading was considered similar to the regional airflow velocity. Because of the higher airflow velocity near the working face, neither the drag force nor the gravitational force was effective enough to control particles movement. On the other hand, PM released from the DPE exhaust tail pipe bears higher velocity. Most of the produced PM quickly followed the airflow direction after being discharged. However, a significant amount of PM in C1 and C2 showed prolonged unpredictable movements before eventually being carried out of the mine drift. However, the small size of PM particles compared to the intense airflow velocity, the Brownian force acting on PM was considered insignificant [147]. Additionally, the thermal impacts of PM emissions were considered minor due to the large cross-sectional area of mine, leading to lower temperatures and reduced thermal conductivity of the released PM [24, 134, 148]. Thus, solely the impact of gravity and drag force on PM was considered [53]. In addition, the PM was considered as discrete phase and the relevant parameters were set according to the actual condition of the experimental field and the characteristics of the PM [149, 150].

4. Results and discussion

4.1. Results

4.1.1. The airflow distribution analysis in OC1

The airflow velocity vectors were selected to represent the airflow distribution and direction at breathing zones 1.5 m and 2.2 m above the ground [124, 151-153]. During field experiment in the mine drift, the supplied volumetric airflow from the outlet of both ducts was 13 m^3/s (v = 13 m/s), the temperature, pressure and relative humidity in the mine drift were 22.85 °C, 968 hPa, and 68%, respectively. Based on the supplied airflow distributions, the mine drift and haulage drift were partitioned into separate regions at each of the breathing zones: backflow region, vortex region, unsteady flow region, and steady flow region. The defined regions were visually depicted using dashed-line quadrilateral and circular shapes in Fig. 10.

The initiation of the backflow region began near the working face because the supplied airflow struck the working face, causing a rebound action that directed the airflow towards the exit of the mine drift. The backflow region covered nearly 13 m from the working face. Following that, a vortex region developed, characterized by the interaction between high-velocity and low-velocity airflow components. The vortex region lasts between 13 m and 20 m. Afterwards, an unstable flow region was developed because of further decrease in airflow velocity. This region exists between 20 m and a little over 52 m. Additionally, between 52 m and 68 m is a relatively stable flow region developed in the mine drift. Near the end of the mine drift the airflow mixed with the existing airflow in the haulage drift. Due to the amalgamation of two airflows an unstable flow region developed in the haulage drift.

The airflow distribution regions were similar at both breathing zones, 1.5 m and 2.2 m, under all three conditions. In C1, as shown in Fig. 10. (a, b), there was negligible fluctuation in the size range of the vortex and unsteady flow regions at both breathing zones. Minor variations in airflow velocities were observed, likely due to the position of the LHD and the height difference between the breathing zones. However, the overall distribution of airflow velocity vectors was consistent in both zones.

In C2, shown in Fig. 10 (c, d), the LHD located in the temporary dumpsite hardly obstructed the airflow stream in the mine drift. Compared to C1, there were small differences in the dimensions and airflow velocities detected in the airflow distribution regions. Furthermore, in C3 as shown in Fig. 10 (e, f), when both the LHD and UMT were located at the intersection of the mine drift and haulage drift, a noticeable difference in the covered area of the backflow region was seen at both breathing zones. The difference occurred because the large size of the LHD and UMT stopped exit of the airflow from the mine drift.

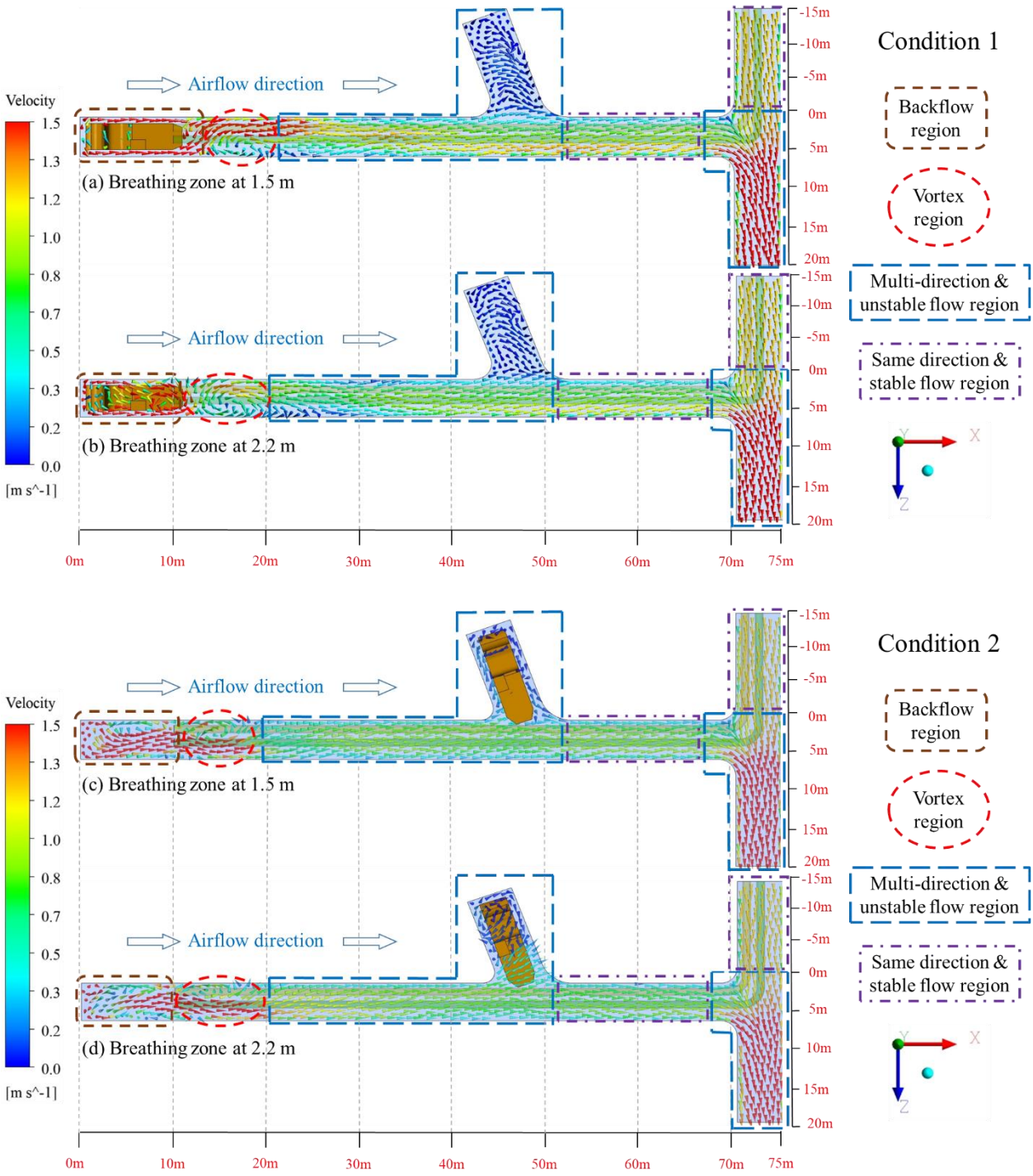
Condition 1
Backflow region
Vortex region
Multi-direction & unstable flow region
Same direction & stable flow region
Airflow direction
Airflow direction
Velocity
[m s^-1]
(a) Breathing zone at 1.5 m
(b) Breathing zone at 2.2 m
(c) Breathing zone at 1.5 m
(d) Breathing zone at 2.2 m
Condition 2
Backflow region
Vortex region
Multi-direction & unstable flow region
Same direction & stable flow region
0m
10m
20m
30m
40m
50m
60m
70m
75m

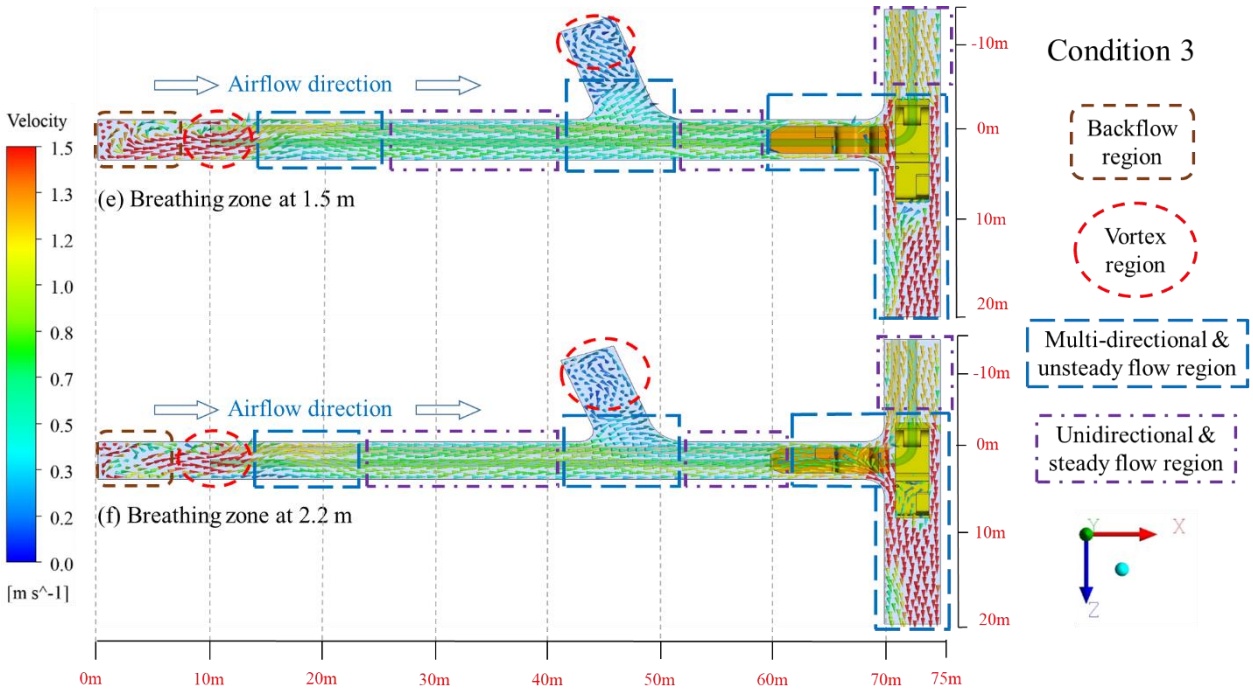

Fig. 11. Airflow streamlines distribution in: (a, b) condition 1 at breathing zones 1.5 m and 2.2 m, (c, d) condition 2 at breathing zones 1.5 m and 2.2 m, and (e, f) condition 3 at breathing zones 1.5 m and 2.2 m

4.1.2. PM analysis in OC1

To analyze the distribution characteristics and migration of PM under given volumetric airflow the CFDPOST software was adopted for the simulation calculation and processing of the results [24, 154-156].

4.1.2.1. PM migration under C1

Fig. 11. (I-a) illustrates the dispersion patterns of PM originating from the muck loading operation and discharged by the LHD. The dominant backflow and vortex regions of airflow resulted in a significant accumulation of PM near the working face, especially at the rear of the LHD. Subsequently, the PM gradually extended towards the exiting via the haulage drift.

Fig. 11. (I-b) illustrates the distribution of PM concentration across the monitoring planes. The highest concentrations of PM were detected near the floor and roof across all the measurement planes, indicating the widespread occurrence of PM pollution in both mine and haulage drifts. The transition in PM distribution from the mine drift to the haulage drift at x = 70 m highlights the influence of airflow dynamics on PM migration patterns.

Fig. 11. (II-a and c) illustrates the impact of airflow vector direction on PM migration at a breathing zone of 1.5 m and 2.2 m. A vortex region was observed within the range of x = 10 to 20 m, influencing the recirculation of PM around the LHD. The vortex region produced irregular and unstable flow patterns, resulting in delays in the migration of PM. Between the distances of 20 and 40 m, the migration of PM exhibited transposition towards the exit, while airflow vectors demonstrated partially stable airflow characteristics. However, a more turbulent airflow vectors distribution of airflow is depicted at height of 2.2 m.

Fig. 11. (II-b and d) presents the PM concentration contours that depict the spatial distribution of PM surrounding the LHD at a height of 1.5 m and 2.2 m. The PM concentrations surpassing 2 x 10^{-6} kg/m³ were observed within the range of x = 0 to 10 m. A gradual decrease in PM concentration was observed as distance increased from x = 10 to 40 m.

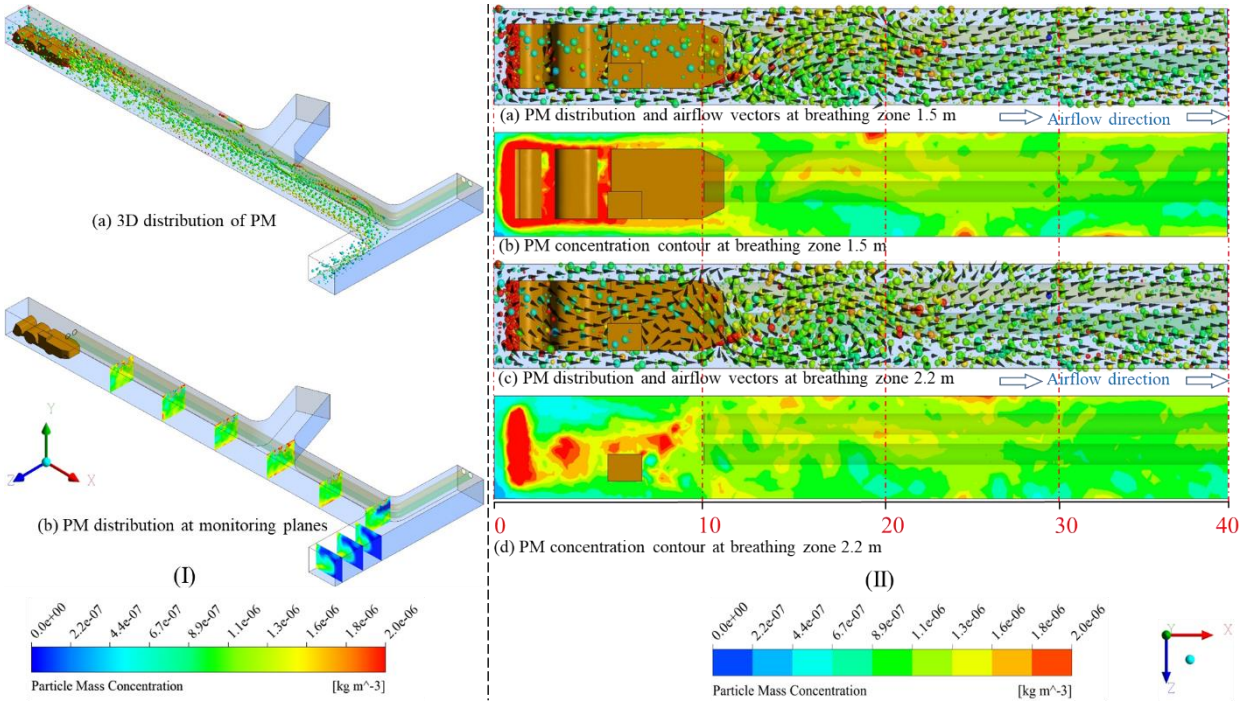

Fig. 12. (I-a) 3D distribution of PM, (I-b) PM distribution at monitoring planes, (II-a) airflow vectors and PM distribution at breathing zone 1.5 m, (II-b) PM concentration at breathing zone 1.5 m, (II-c) airflow vectors and PM distribution at breathing zone 22.2 m, (II-d) PM concentration at breathing zone 2.2 m, in C1

4.1.2.2. PM migration under C2

Fig. 12. illustrates essential insights into airflow transition and PM migration during the unloading operation of LHD within the temporary dumpsite in C2. The distribution of PM resulted from the unloading operation and LHD tailpipe exhaust, as illustrated in Fig. 12. (I-a). The PM concentration exceeded 2 x 10^{-6} kg/m³ and was randomly distributed within the temporary dumpsite. The PM progressively moved toward the haulage drift due to the impact of the incoming airflow. This illustrates the challenges associated with the efficient management of PM dispersion in the dumpsite.

Fig. 12. (I-b) illustrates the observed patterns of PM concentration on monitoring planes situated at distances of x = 50, 60, and 70 m within the mine drift, and at heights of 10, 15, and 20 m in the haulage drift. The observation of PM within the range of x = 20 to 40 m revealed no traces of PM associated with the direction of supplied airflow. Concentrations of PM exceeding 2 x 10^{-6} kg/m³ were primarily observed near the roof and right-side wall of the mine drift at the monitoring plane x = 50 m. This results from unobstructed airflow through AVS, which effectively limits PM access to the mine drift. A similar pattern of PM distribution is observed at x = 60 m; however, there is a gradual decrease in PM concentration at the lower right side of the monitoring plane. The incoming airflow resulted in the partial dispersion of PM in this region. At the monitoring plane x = 70 m, PM was detected near the roof and suppressed along the left

side wall of the mine drift. This demonstrates the effect of airflow mixing between the mine drift and the haulage drift. Consequently, PM migration predominantly occurred along the roof and left-side wall of the haulage drift, observable at monitoring planes situated within the z = 10 to 20 m range.

Fig. 12. (II-a) depicts the distribution of airflow vectors and the migration of PM at a height of 1.5 m breathing zone. Upon entering the temporary dumpsite, airflow impacted the left side of the LHD, resulting in circulation around the vehicle before exiting the dumpsite from the right side of the LHD. The pressure differential between the dumpsite and the mine drift obstructs the efficient transfer of PM from the dumpsite. PM produced during the unloading operation exhibited a tendency to ascend towards the roof, whereas PM emitted from the LHD remained near the floor until reaching the end of the mine drift.

The PM distribution contours are presented in Fig. 12. (II-b) demonstrate that PM concentration surpasses 2×10^{-6} kg/m³ within the range of x = 40 to 50 m. The concentration was diluted and did not exceed 8.9×10^{-7} kg/m³ in the range of x = 50 to 70 m. The diffusion of PM within the range of x = 50 to 60 m was constrained to the right-side wall of the mine drift due to the resistance from incoming airflow. Consequently, over half of the mine drift was not impacted by PM dispersion. Furthermore, PM distribution within the range of x = 60 to 70 m extended to half of the mine drift due to the transmission of airflow into the haulage drift. In the haulage drift, differential airflow pressures facilitated the migration of PM towards the roof, resulting in a nearly negligible PM concentration at the 1.5 m breathing zone.

Fig. 12. (II-c) illustrates the arrangement of airflow vectors and the transition of PM at a height of 2.2 m. The incoming airflow collided with the right-side wall of the temporary dumpsite and reflected inward, creating a vortex region above the front of the LHD. The pressure differential between the mine drift and the dumpsite was the main factor contributing to the obstruction of PM transit. Additionally, the presence of the LHD reduced the cross-sectional area while simultaneously increasing the pressure difference. Consequently, PM accumulated within the dumpsite, leading to increased concentrations.

Fig. 12. (II-d) illustrates the PM concentrations exceeding 2×10^{-6} kg/m³ across the range of x = 40 to 50 m. The concentrations cover a significant portion of the mine drift from x = 50 to 60 m and extend to more than half of the mine drift from x = 60 to 70 m. Upon entering the haulage drift, the PM concentration was significantly dispersed due to alterations in airflow pressure and an increase in cross-sectional area. Consequently, the PM concentration in the haulage drift is less than 6.7×10^{-7} kg/m³.

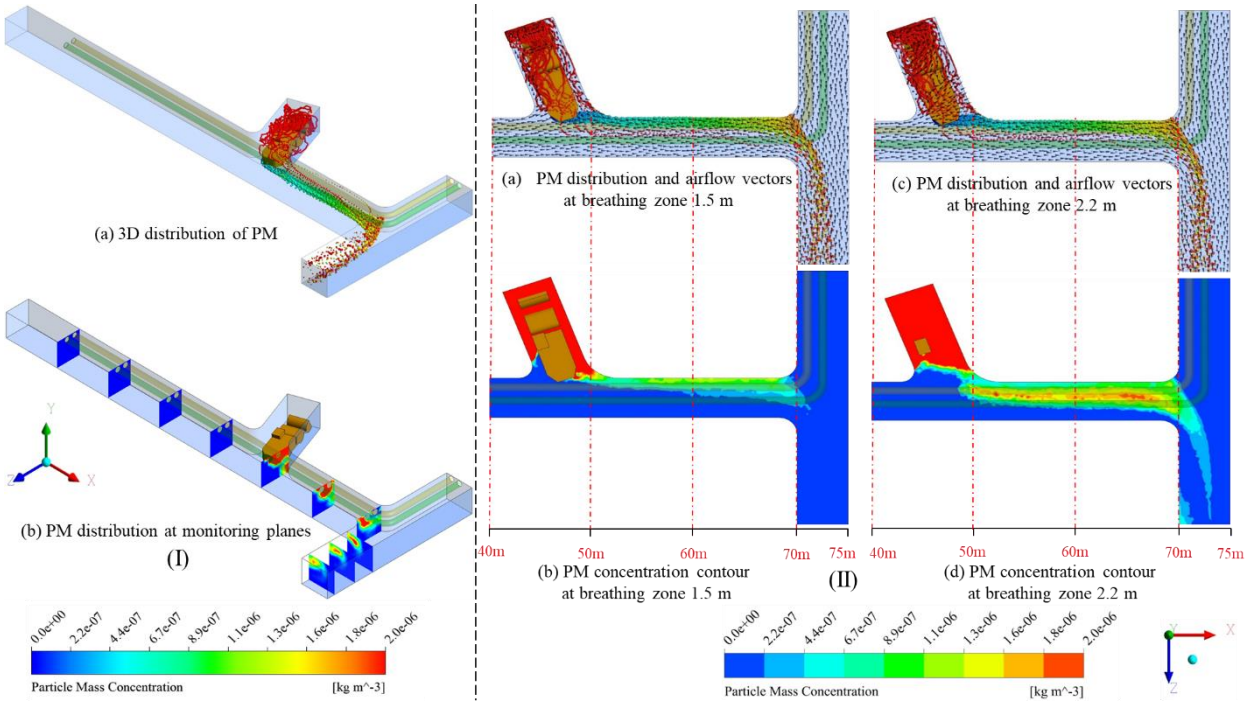

Fig. 13. (I-a) 3D distribution of PM, (I-b) PM distribution at monitoring planes, (II-a) airflow vectors and PM distribution at breathing zone 1.5 m, (II-b) PM concentration at breathing zone 1.5 m, (II-c) airflow vectors and PM distribution at breathing zone 2.2 m, (II-d) PM concentration at breathing zone 2.2 m in C2

4.1.2.3. PM migration under C3

Fig. 13. presents the results related to airflow vectors and PM dispersion at breathing zones of 1.5 m and 2.2 m under C3. The cross-section of the mine drift and haulage drift in Fig. 13. (I-a) demonstrates a random distribution of PM emissions resulting from unloading operation, and tailpipe exhaust of LHD and UMT. The PM migration was moving from the left-side wall to the center of the haulage drift. The transition resulted from the substantial dimensions of the UMT, which restricted airflow from entering through the sides and the UMT itself. The airflow resistance generated a pressure differential at the front of the UMT, which contributed to the accumulation of PM.

Fig. 13. (I-b) illustrates the lack of PM on monitoring planes situated within the mine drift (x = 10 to 60 m). It is because of the direction of airflow. PM concentration was observed solely on monitoring planes located within the haulage drift (z = 10 to 20 m), with dispersion occurring as distance increased. The distribution of PM migration on monitoring planes between Z = 10 to 20 m indicated a shift in PM concentration from the upper right corner and center to the lower left corner and center within the haulage drift. The mechanism of PM transition is indicative of swirling airflow, observed exclusively under C3.

Fig. 13. (II-a) depicts the airflow vectors at a height of 1.5 m above the floor, demonstrating the movement of PM around the LHD and UMT. The PM released by the LHD traveled along the airflow adjacent to the left-side wall of the haulage drift (z = 0 to 10 m). The UMT's presence obstructs airflow, leading to the accumulation of PM in the central region of the haulage drift (z = 10 to 20 m).

Fig. 13. (II-b) illustrates PM concentration contours, revealing levels surpassing 2 x 10^{-6} kg/m^3 in proximity to the LHD cabin and in front of the UMT, extending to the end of the haulage drift. Beyond z = 15 m, the

concentration splits into two parts because of the swirling flow pattern of PM, with a predominant accumulation at the center of the haulage drift.

Fig. 13. (II-c) illustrates the airflow vectors at a height of 2.2 m above the floor in the breathing zone. The redirection of airflow into the mine drift after colliding with the UMT. This diversion directs PM emissions from the LHD towards the left-side wall of the haulage drift (z = 0 to 10 m). The accumulation of PM in the haulage drift center (z = 10 to 20 m) was enhanced by the creation of a low airflow pressure zone in front of the UMT.

Fig. 13. (II-d) illustrates the contours of PM concentration at a height of 2.2 m above the floor. PM concentrations were observed to exceed 2 x 10^{-6} kg/m³ in proximity to the LHD and UMT cabins (z = 0 to 10 m). The swirling pattern observed in the transition of PM led to a division in PM concentration distribution at a breathing zone of 2.2 m, occurring before z = 15 m. The distribution of PM concentration throughout the haulage drift reveals a minor concentration gap at the center.

The results demonstrated the intricate relationship among the positioning of LHD and UMT, airflow dynamics, and PM dispersion, highlighting the necessity of careful consideration of these factors in the design of ventilation systems and operational schedules in underground mining environments.

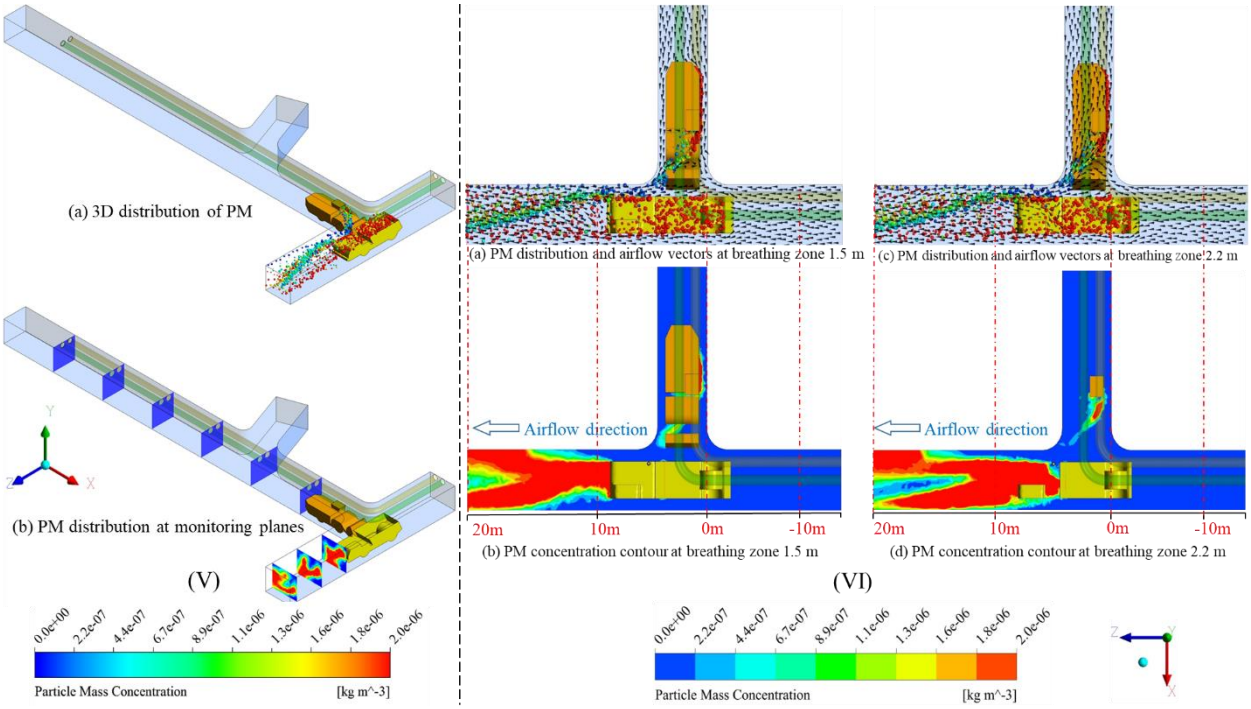

Fig. 14. (I-a) 3D distribution of PM, (I-b) PM distribution at monitoring planes, (II-a) airflow vectors and PM distribution at breathing zone 1.5, (II-b) PM concentration at breathing zone 1.5 m, (II-c) airflow vectors and PM distribution at breathing zone 2.2, (II-b) PM concentration at breathing zone 2.2 m in C3

4.1.3. Effect of varying volumetric airflows to dilute PM concertation

The variability in PM behavior was observed across all three conditions, attributable to factors including supplied volumetric airflow, operational conditions, and the positioning of the LHD and UMT. The exposure of LHD and UMT operators to elevated PM concentrations was evaluated across all three conditions with differing supplied volumetric airflows. A comparative analysis was conducted to determine

the most effective airflow volume for optimal dilution and dispersion of PM. The initial assessment of PM dilution was conducted with an actual airflow volume of Q = 13 m³/s (v = 13 m/s), supplied in the mine drift via AVS. The research included simulations with three distinct airflow volumes: Q = 15 m³/s (v = 15 m/s), Q = 17 m³/s (v = 17 m/s), and Q = 20 m³/s (v = 20 m/s). The objective of these simulations was to analyze the behavior of PM and to propose an optimized airflow volume.

4.1.3.1. Effect of varying volumetric airflows in C1

Fig. 14. (a, i, ii) illustrates the PM distribution contours for a supplied volumetric airflow of Q = 13 m³/s at breathing zones of 1.5 m and 2.2 m. PM concentrations greater than 2 x 10^{-6} kg/m^3 were observed in the vicinity of the LHD and within the dumpsite, specifically in the ranges of x = 0 to 10 m and X = 40 to 50 m, respectively. A notable concentration of PM was detected within the range of x = 10 to 40, exceeding 1.6 x 10^{-6} kg/m^3. Furthermore, PM concentration exhibited notable persistence beyond x = 50 m, reaching a maximum value of 1.3 x 10^{-6} kg/m^3. Across the range of x = 70 to 75 m, the distribution of PM covered a significant cross-sectional area of the haulage drift, with concentrations exceeding 1.3 x 10^{-6} kg/m^3.

An increase in the supplied volumetric airflow to Q = 15 m^3/s resulted in a significant reduction in PM concentration, measured at less than 1.1 x 10^{-6} kg/m^3 between x = 10 to 75 m, demonstrating enhanced ventilation effectiveness. A notable rise in PM concentration was observed within the dumpsite due to alterations in airflow pressure differentials, as illustrated in Fig. 14. (b, i, ii). Furthermore, Fig. 14. (c, i, ii) illustrates that the PM concentration was further reduced, remaining below 8.9 x 10^{-7} kg/m^3 between x = 10 to 75 m. The PM concentration was reduced within the dumpsite due to the supplied volumetric airflow of Q = 17 m^3/s. Finally, Fig. 14. (d, i, ii) illustrates the PM contours, indicating that the PM concentration remains below 6.7 x 10^{-6} kg/m^3 for the range of x = 10 to 75 m, influenced by a volumetric airflow of Q = 20 m³/s.

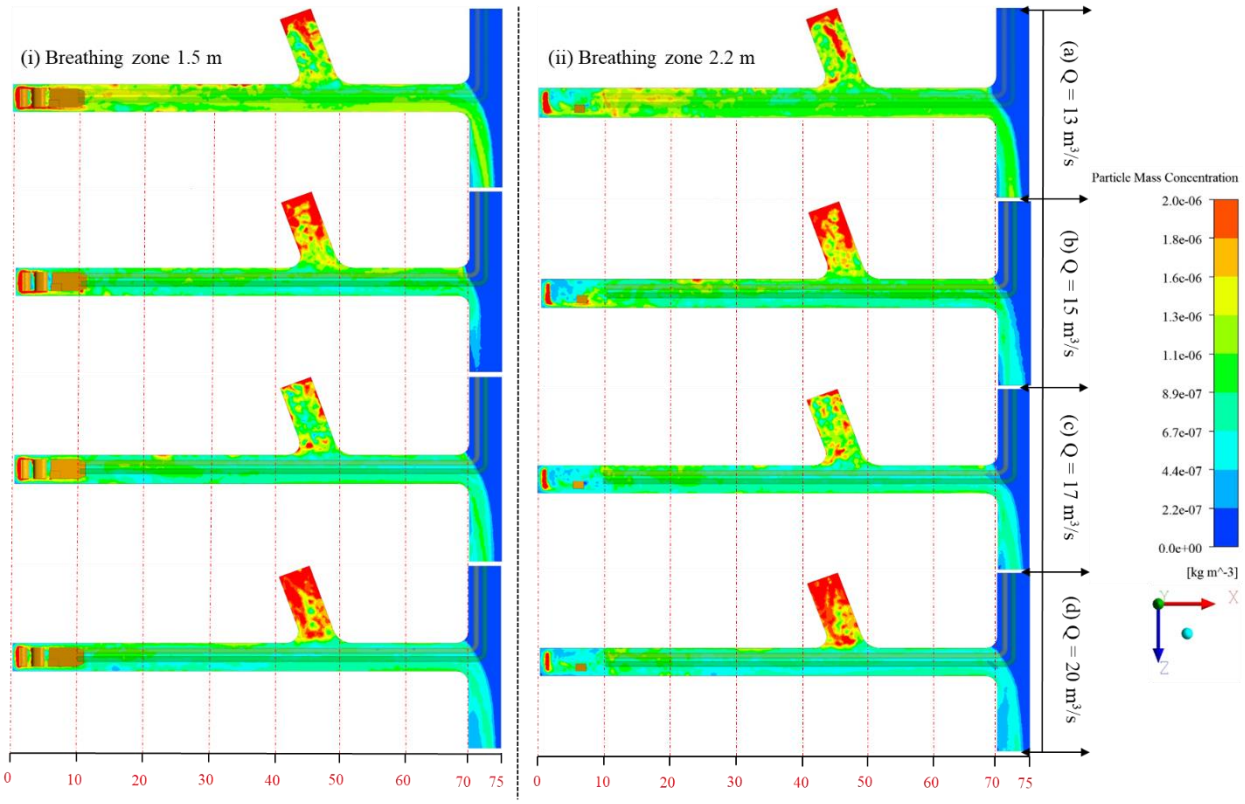

Fig. 15. PM concentration distribution at breathing zones (i) 1.5 m and (ii) 2.2 m, under varying supplied volumetric airflows in C1: (a) Q = 13 m3/s, (b) Q = 15 m3/s, (c) Q = 17 m3/s, (d) Q = 20 m3/s

4.1.3.2. Effect of varying volumetric airflows in C2

The PM distribution contours for a supplied volumetric airflow of Q = 13 m³/s at breathing zones of 1.5 m and 2.2 m are illustrated in Fig. 15. (a, i, ii). PM concentrations surpassing 2 x 10^{-6} kg/m^3 were observed in the vicinity of the LHD within the dumpsite, specifically within the range of x = 40 to 50 m. The PM concentration from x = 50 to 75 m remained below the 8.9 x 10^{-7} kg/m^3 at a height of 1.5 m in the breathing zone. The PM concentration within the range of x = 50 to 70 m at a breathing zone of 2.2 m approached approximately 2 x 10^{-6} kg/m^3. In the haulage drift from x = 70 to 75 m, the PM concentration did not exceed 8.9 x 10^{-7} kg/m^3 due to alterations in the cross-sectional area and an increase in airflow volume.

When the volumetric airflow increased to Q = 15 m³/s, the PM concentration contours are illustrated on Fig. 15. (b, i, ii). PM concentrations greater than 2 x 10^{-6} kg/m^3 were recorded between x = 40 to 70 m at both 1.5 m and 2.2 m breathing zones. The variation in cross-sectional area and airflow volume resulted in PM concentration not exceeding 1.6 x 10^{-6} kg/m^3 between x = 70 to 75 m at both 1.5 m and 2.2 m breathing zones. Additionally, the PM concentration contours influenced by a supplied volumetric airflow of Q = 17 m³/s are presented in Fig. 15. (c, i, ii). The PM concentration between x = 50 to 70 m remained below the 1.6 x 10^{-6} kg/m^3 at a breathing zone of 1.5 m. However, a PM concentration exceeding 2 x 10^{-6} kg/m^3 was recorded within the same distance range at a breathing zone of 2.2 m. The haulage drift between x = 70 to 75 m maintained a concentration below the limit of 6.7 x 10^{-7} kg/m^3 at both the 1.5 m and 2.2 m breathing zones. Finally, the PM contours indicated PM concentration influenced by an increased volumetric airflow of Q = 20 m³/s, as illustrated in Fig. 15. (d, i, ii). The reduction in PM concentration was noted between x = 50 to 75 m, remaining below 1.6 x 10^{-6} kg/m^3 at the 1.5 m and 2.2 m breathing zones.

The distribution of PM concentration between x = 50 to 75 m varied with the supplied volumetric airflows. However, these volumetric airflows exerted a negligible effect on the PM concentration inside the dumpsite. The concentration of PM within the dumpsite was likely confined, with migration impeded due to elevated volumetric airflows in the mine drift.

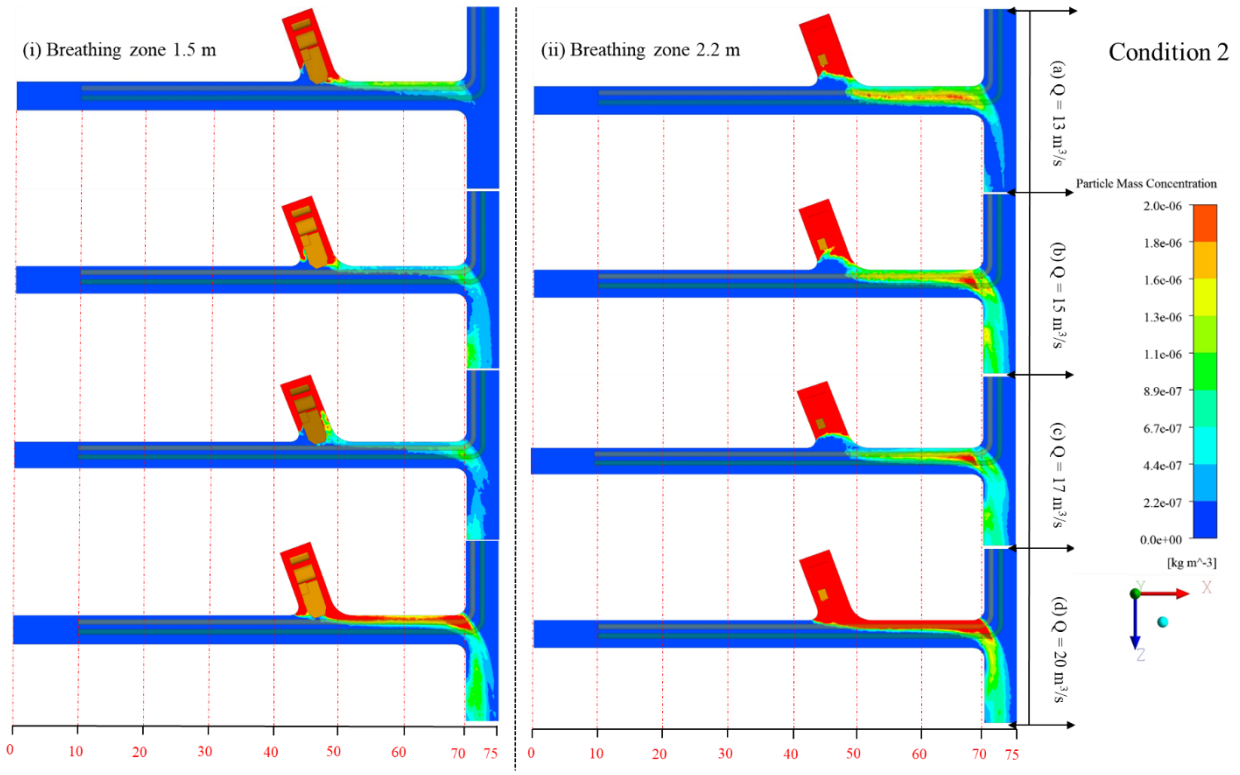

Fig. 16. PM concentration distribution at breathing zones (i) 1.5 m and (ii) 2.2 m, under varying supplied volumetric airflows in C2: (a) Q = 13 m3/s, (b) Q = 15 m3/s, (c) Q = 17 m3/s, (d) Q = 20 m3/s

4.1.3.3. Effect of varying volumetric airflows in C3

Fig. 16. (a, i, ii) illustrates the PM distribution contours for a supplied volumetric airflow of Q = 13 m^3/s at breathing zones of 1.5 m and 2.2 m. PM concentrations greater than 2 x 10^{-6} kg/m^3 were observed on the right side of the LHD, specifically within the range of x = 60 to 70 m and in front of the UMT at x = 70 to 75 m. The PM emitted from LHD was transmitted to the left-side wall of the haulage drift due to the supplied volumetric airflow. The supplied airflow was distributed on both sides of the UMT, leading to a bifurcation of PM concentration in the front of the UMT due to the swirling airflow effect.

When the volumetric airflow increased to Q = 15 m^3/s, the PM concentration contours are illustrated in Fig. 16. (b, i, ii). A minor decrease in PM concentration was noted in the mine drift; however, a substantial reduction in PM distribution was evident at the front of the UMT in the haulage drift. Furthermore, the PM concentration contours were illustrated under the influence of a supplied volumetric airflow of Q = 17 m^3/s in Fig. 16. (c, i, ii). An increase in PM concentration was noted near the left-side wall, while a decrease was observed adjacent to the right-side wall of the haulage drift, at both 1.5 and 2.2 m breathing zones, compared to previous volumetric airflow measurements. Finally, the PM contours indicated a further decrease in PM concentration with the increase in volumetric airflow to Q = 20 m^3/s, as illustrated in Fig. 16. (d, i, ii).

The distribution contours of PM concentration exhibited a distinct trend of dispersion resulting from the swirling airflow under these conditions. A distinction in PM concentration was noted across all provided volumetric airflows at both breathing zones. With the increase in volumetric airflow, the division between PM concentration lengthened and shifted towards the right-side wall of the haulage drift.

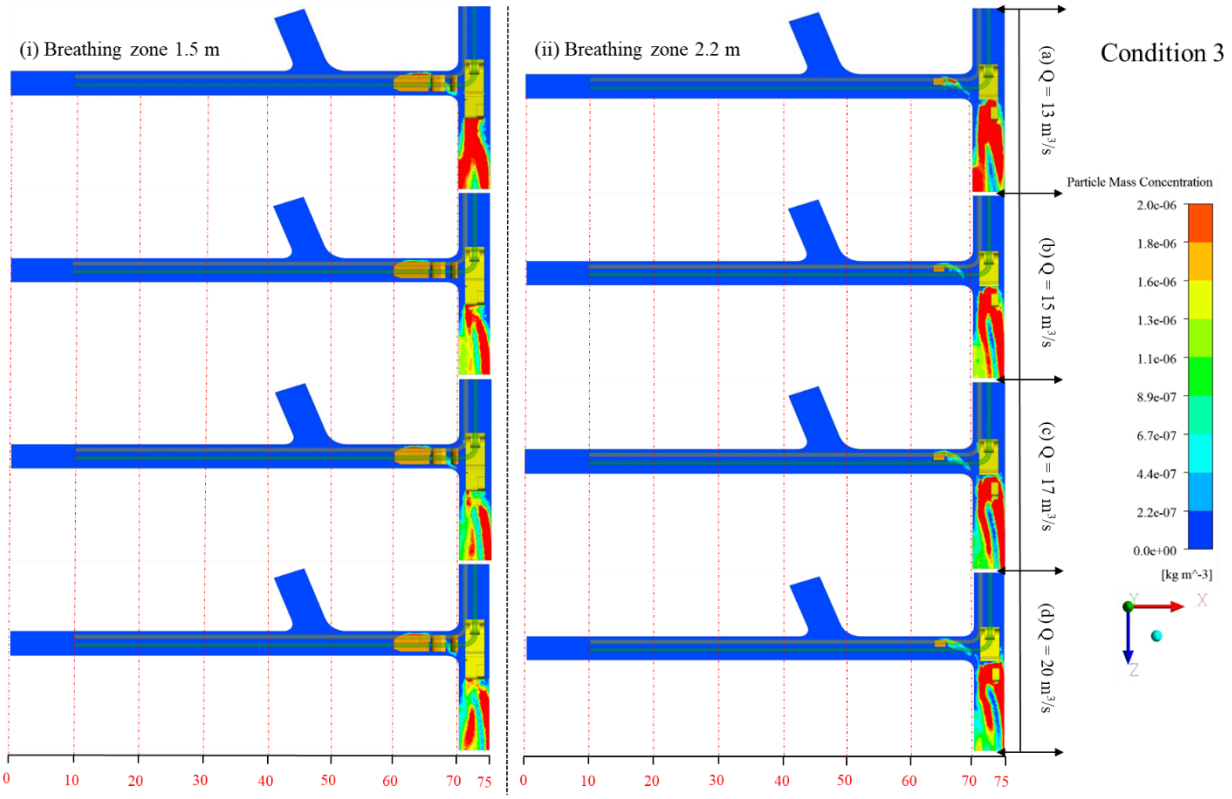

Fig. 17. PM concentration distribution at breathing zones (i) 1.5 m and (ii) 2.2 m, under varying supplied volumetric airflows in C3: (a) Q = 13 m3/s, (b) Q = 15 m3/s, (c) Q = 17 m3/s, (d) Q = 20 m3/s

The systematic decrease in PM concentration contours was directly related to the increase in supplied volumetric airflows. The differing volumetric airflows effectively elevated the generated PM above the breathing zones, reaching near the roof and extending beyond the boundaries of the observational area.

4.1.4. Comparative analysis of PM diffusion rate under varying volumetric airflows.

The PM diffusion rate was calculated using the area-weighted average across the mine drift and haulage drift under all three operating conditions. The PM diffusion rate was determined for all four volumetric airflows, and a mathematical function was proposed based on the curve fitting technique for each airflow to achieve PM diffusion rate.

4.1.4.1. PM diffusion rate in C1

Fig. 17. (a) depicts the diffusion rate of PM under C1. The diffusion rate trend line demonstrated fluctuations in response to volumetric airflow rates of Q = 13 m^3/s and 15 m^3/s. The trend line exhibited an upward trajectory both before and after the temporary dumpsite, particularly within the 40 to 50 m range in the mine drift. The transmission of PM from mine drift to haulage drift resulted in a significant reduction in PM concentration, as evidenced by the associated trend line. The mathematical functions that

characterize the diffusion rates are expressed as: PMQ13 = -0.0005x^4 + 0.0987x^3 - 6.2875x^2 + 165.75x - 521and PMQ15 = -0.0017x^4 + 0.2841x^3 - 17.26x^2 + 437.88x - 3031.1, respectively. On the other hand, the trend line for PM diffusion rate influenced by flow rates of Q = 17 m^3/s and 20 m^3/s show a consistent decline in the PM concentration. The mathematical functions governing PM diffusion with the Q = 17 m^3/s and 20 m^3/s volumetric airflows are outlined as follows: PMQ17 = -6.3457x + 981.06 and PMQ20 = 4.2686x + 885.75, respectively. The least PM concentration was observed at an operating flow rate of Q = 17 m^3/s.

4.1.4.2. PM diffusion rate in C2

Fig. 17. (b) illustrates the rate of PM diffusion under C2. In contrast to C1, the concentration of PM increased with greater distance. The trend line's behavior is affected by the position of the LHD, airflow direction, monitoring point locations, and the concentration of PM, quantified as an area-weighted average. The concentration of PM peaked at an airflow rate of Q = 20 m^3/s, as a substantial quantity of PM was transferred from the temporary dumpsite to the mine drift. The concentration of PM at designated monitoring points increased with increasing distance. The diffusion rate under volumetric airflow of Q = 13 m^3/s, 15 m^3/s, and 17 m^3/s represented a decent linear behavior by the following mathematical functions: PMQ13 = 23.171x - 860.84, PMQ15 = - 32.635x - 1519.4, PMQ17 = 29.326x - 1356.1. However, the diffusion rate trend line under volumetric airflow Q = 20 m^3/s depicted fluctuated behavior and given by the mathematical function PMQ20 = 0.5048x^3 - 89.674x^2 + 5290.9x - 102848. The least PM concentration was recorded at a volumetric airflow of Q = 17 m^3/s.

4.1.4.3. PM diffusion rate in C3

Fig. 17. (c) illustrates the PM diffusion rate under C3. The trend line for PM concentration at Q = 13 m^3/s indicates the highest concentration, which decreases with increasing distance. In contrast, at Q = 15 m^3/s, the PM concentration depicted considerable fluctuations. However, a consistent decline in the PM concentration was observed under the volumetric airflows Q = 17 m^3/s and 20 m^3/s. Under C3, a flow rate of Q = 20 m^3/s shows the maximum diffusion rate. The mathematical functions describing the diffusion rate under the specified volumetric airflows are as follows: PMQ13 = -15.883z^2 + 400.25z + 99.689, PMQ15 = 0.3124z^5 - 23.871z^4 + 717.94z^3 – 10622z^2 + 77291z - 219241, PMQ17 = -6.2231z^2 + 120.9z + 1528.4, and PMQ20 = -110.21z + 3315.9.

The turbulence intensity of airflow regions mainly affects the PM concentrations on the data points. In C1 and C3, Q = 13 and 15 shows polynomial curves with cube or higher power due to random movements of PM resulted in higher and lower PM concentrations on the monitoring points. A decent slope is observed under Q = 17 and Q = 20 because higher air velocity pushed the PM in a more controlled manner and resulted in a continuous decrease in PM concentration on the monitoring points.

In C2, the fluctuated PM concentration was observed under Q = 20 while the remaining airflows show a decent curve but in ascending direction. The possible reasons could be the position of LHD which influences the discharge direction of DPM. Additionally, higher airflow velocity acted like a curtain effect

and resisted the PM transposition from the dumpsite to production drift. Resultantly, a less amount of PM was transposing from dumpsite to production drift, and it was suppressed along the right side wall till the end of the production drift.

As a result, in C1 and C2, we observed the optimized diffusion rate under the influence of Q = 17 m^3/s, and in C3, it was observed under the influence of Q = 20 m^3/s. Because of LHD's dynamic operating nature, it may not be feasible to continuously vary the volumetric airflow of an AVS based on LHD's positions and operating conditions. Therefore, based on the diffusion rate analysis, Q = 17 m^3/s is proposed as the optimal volumetric airflow for all three conditions.

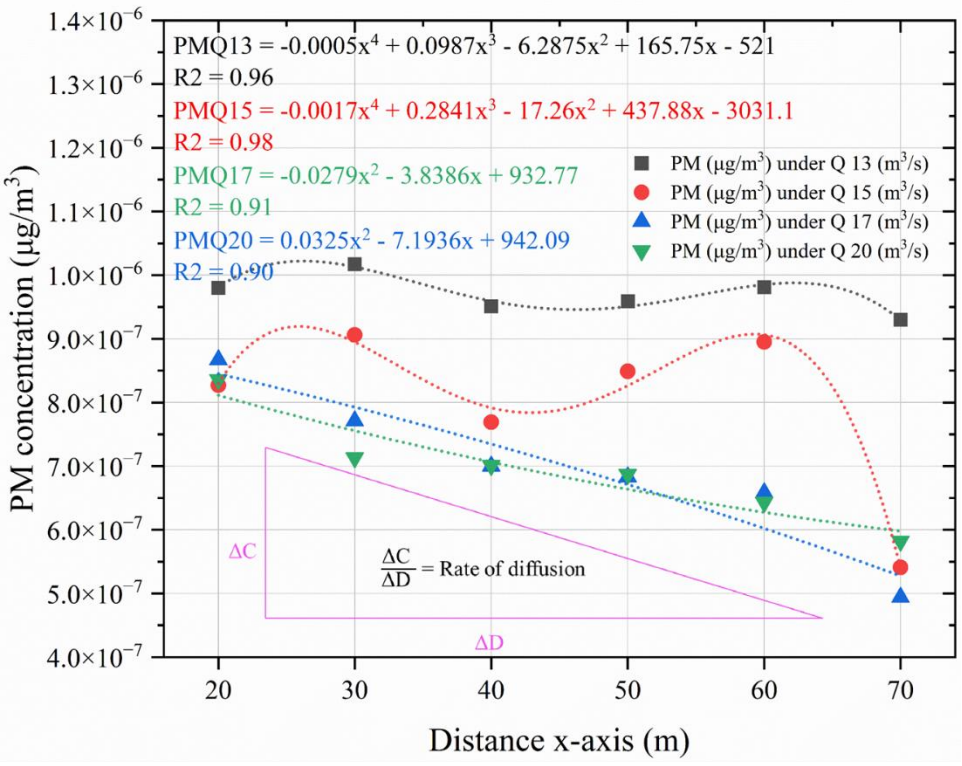

(a) Condition 1

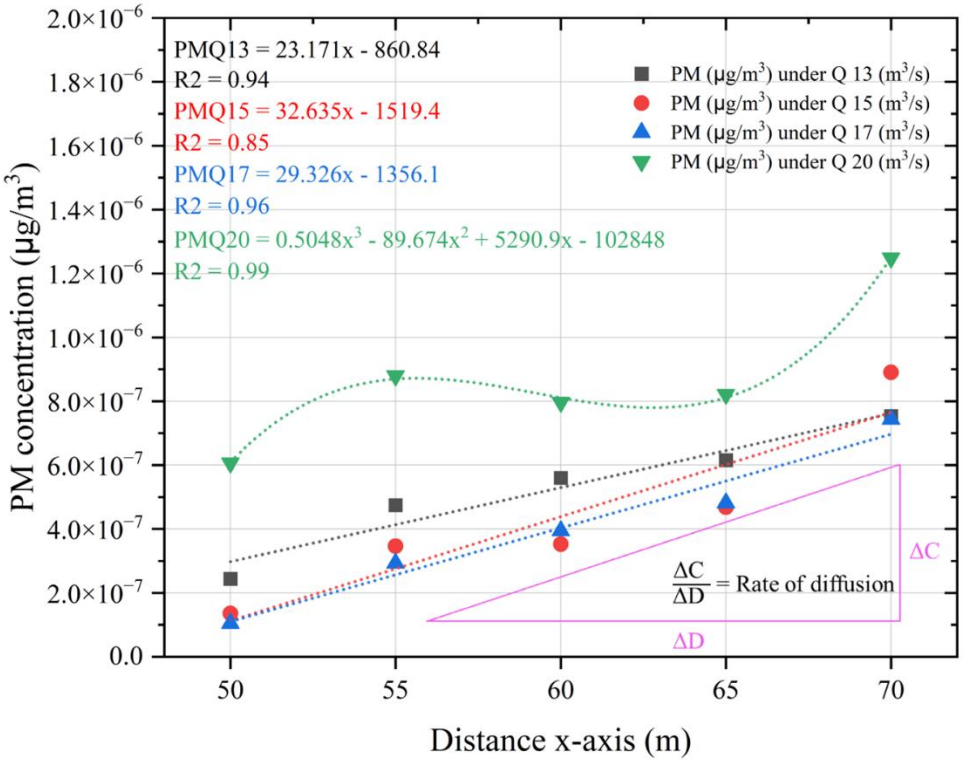

(b) Condition 2

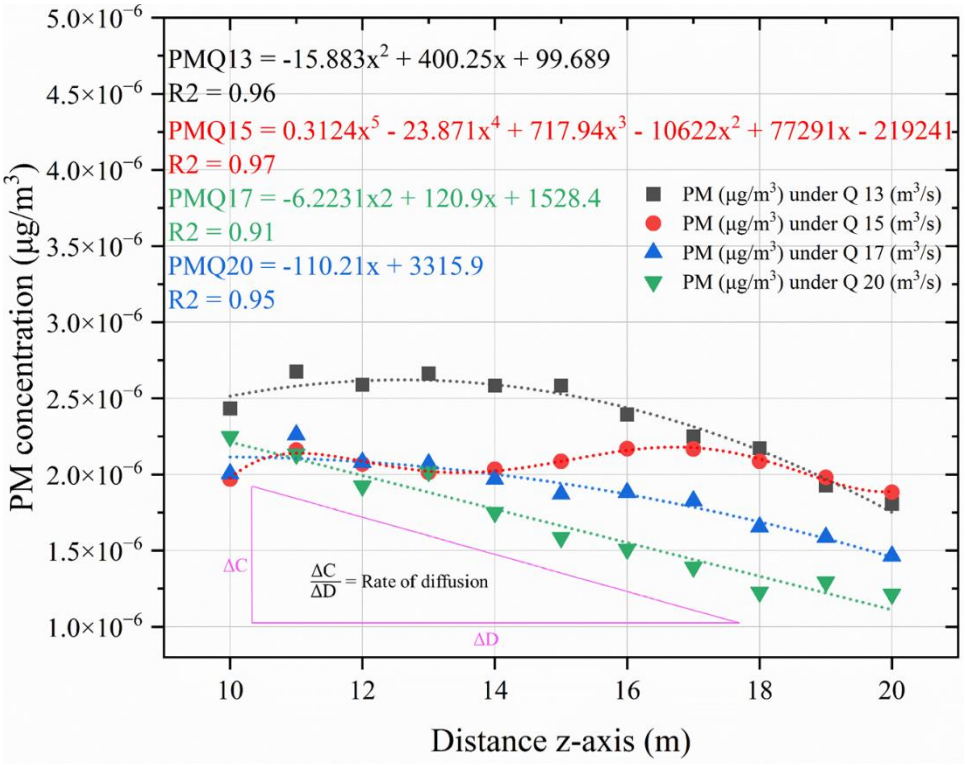

(c) Condition 3

Fig. 18. PM diffusion rate under different volumetric airflows (a) C1, (b) C2, and (c) C3

4.1.5. Proposed volumetric airflow

The engine power of the LHD and UMT was recorded at 269 kW and 433 kW, respectively. The area of the mine drift measured 18.92 m², while the dumpsite and haulage drift covered 21.5 m². The volumetric airflow at the AVS outlets was 13 m³/s. Consequently, the existing volumetric airflow, based on the diesel

engine power, was determined to be 0.048 m³/s. In contrast, the proposed volumetric airflow, considering the diesel engine power, was calculated to be 0.064 m³/s, resulting in an output of 17 m³/s or 20 m³/s per kW at the AVS outlet. As a result, the necessary airflow speeds were calculated for the mine drift, dumpsite, and haulage drift. The estimated airflow velocity for the mine drift was 0.89 m/s, while both the dumpsite and haulage drift required a velocity of 1.28 m/s. Elevated PM concentrations were observed inside the dumpsite, as it was not feasible to equip it with AVS. Consequently, a very low airflow velocity was recorded within the dumpsite, which directly contributed to the formation of a highly vulnerable zone for the LHD operator.

4.1.6. The airflow distribution analysis in OC 2

Due to a slight change in both operating conditions, the airflow analysis conducted for both S1 and S2 of OC-2 separately.

4.1.6.1. Airflow distribution in x, y, and z coordinates

The airflow within the drift exhibits turbulence due to the dynamic nature of mining activities and the complex geometry of the mine drift. Fig. 19 (a and b) demonstrates that evaluating airflow velocity in the x, y, and z directions across the six-line monitors provides insights into the intensity and direction of airflow in the drift, which generally leads to the formation of eddies. The line monitors are identified as L1 (x, 1.5, 3.4), L2 (x, 1.5, 2.2), L3 (x, 1.5, 1), L4 (x, 2.2, 1), L5 (x, 2.2, 2.2), and L6 (x, 2.2, 3.4). The mean of all six lines in each AVS design and in both scenarios was employed to measure the airflow velocity in the x-direction (Vx), y-direction (Vy), and z-direction (Vz). In S1, the line monitors ranged from 11 m to 70 m because the LHD was situated near the working face; conversely, in S2, the line monitors began at 0 m and extended to 70 m as the DPE was placed within the temporary dumpsite. The mine drift is classified into "Unstable flow region" and "Partially stable flow region" based on the Vx, Vy, and Vz components of airflow velocity.

The (i) S1-AVS 1 defines the unstable flow region between 10 and 30 meters. In this region, Vx reached 1 m/s, Vy achieved 0.5 m/s, and Vz fluctuated between -0.25 and 0.4 m/s, respectively. In the region of partially steady flow, these components demonstrate minimal variations. The (v) S2-AVS 1 denotes the unstable flow region ranging from 0 to 25 m. In this region, Vx ranged from -0.75 to 1 m/s, Vy ranged from -1.5 to 1 m/s, and Vz ranged from 1.5 to -0.25 m/s, respectively.

The (ii) S1-AVS 2 displays an unstable flow zone between 10 to 22 m, while the rest of the drift is marked by a relatively stable flow region. In the unstable flow region, Vx surpassed 1 m/s, while Vy fluctuated between -0.5 and 0.25 m/s, and Vz varied between 0.5 and -0.1 m/s, respectively. The (vi) S2-AVS 2 indicates the unstable flow zone within a distance of less than 20 m. The Vx ranges from -0.25 to 2.5 m/s, Vy varies from -2 to 1 m/s, and Vz fluctuates between 0.25 and -0.25 m/s.

The (iii) S1-AVS 3 demonstrates an unstable flow zone between 10 and 25 m, while the rest of the drift is marked by a relatively stable flow region. In the unstable flow region, Vx surpassed 1.5 m/s, Vy fluctuated

between –0.25 and 0.35 m/s, while Vz remained roughly 0 m/s. The (vii) S2-AVS 3 delineates the unstable flow zone, which extends from 0 to 15 meters. The Vx reached a peak of 1.75 m/s, the Vy fluctuated between -2.5 and 0.75 m/s, while the Vz remained close to 0 m/s.

The (iv) S1-AVS 4 demonstrates an unstable flow area between 10 and 25 m, whereas the rest of the drift is characterized by a relatively stable flow region. In the unstable flow region, Vx surpassed 1.1 m/s, while Vy fluctuated between -0.25 and 0.35 m/s, and Vz varied between 0.5 and -0.12 m/s, respectively. (viii) The S2-AVS 4 indicates that the unstable flow zone is located below 20 m. The Vx reached a peak of 1.75 m/s, while Vy fluctuated between -2.12 and 0.5 m/s, and Vz varied between 0.3 and -1.5 m/s, respectively.

The results demonstrate that the most stable flow zone is found in AVS 2 and 3 in both scenarios. The Vx exhibits near-identical characteristics with minor variations. The Vy and Vz components play a significant role in the generation of turbulent and unstable flow regions. In AVS 2 and 3, the impact of Vz is negligible, leading to minimal turbulence effects in the Z-direction of airflow. The variations in the Vy direction are typically attributed to the airflow mechanism.

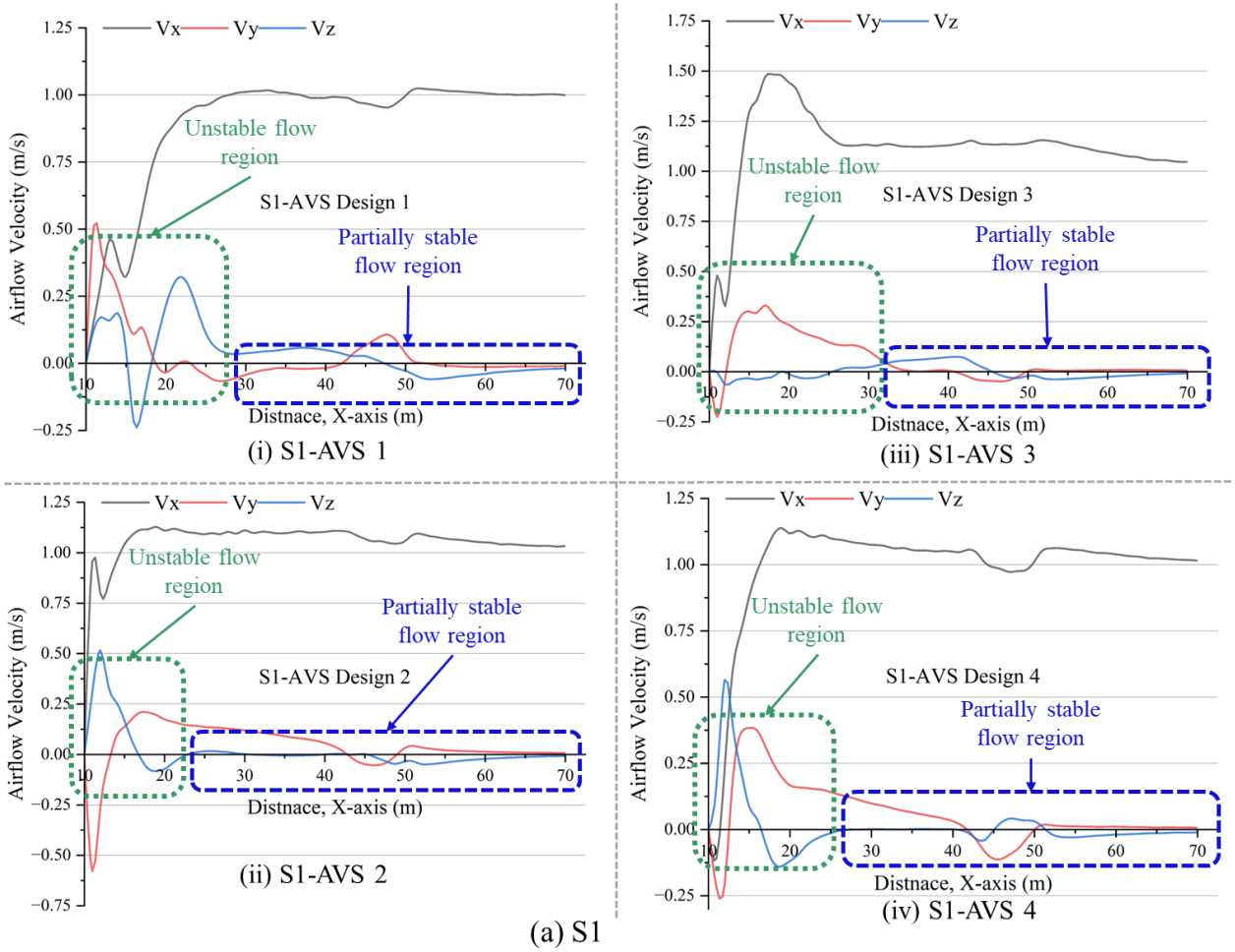

(a) S1

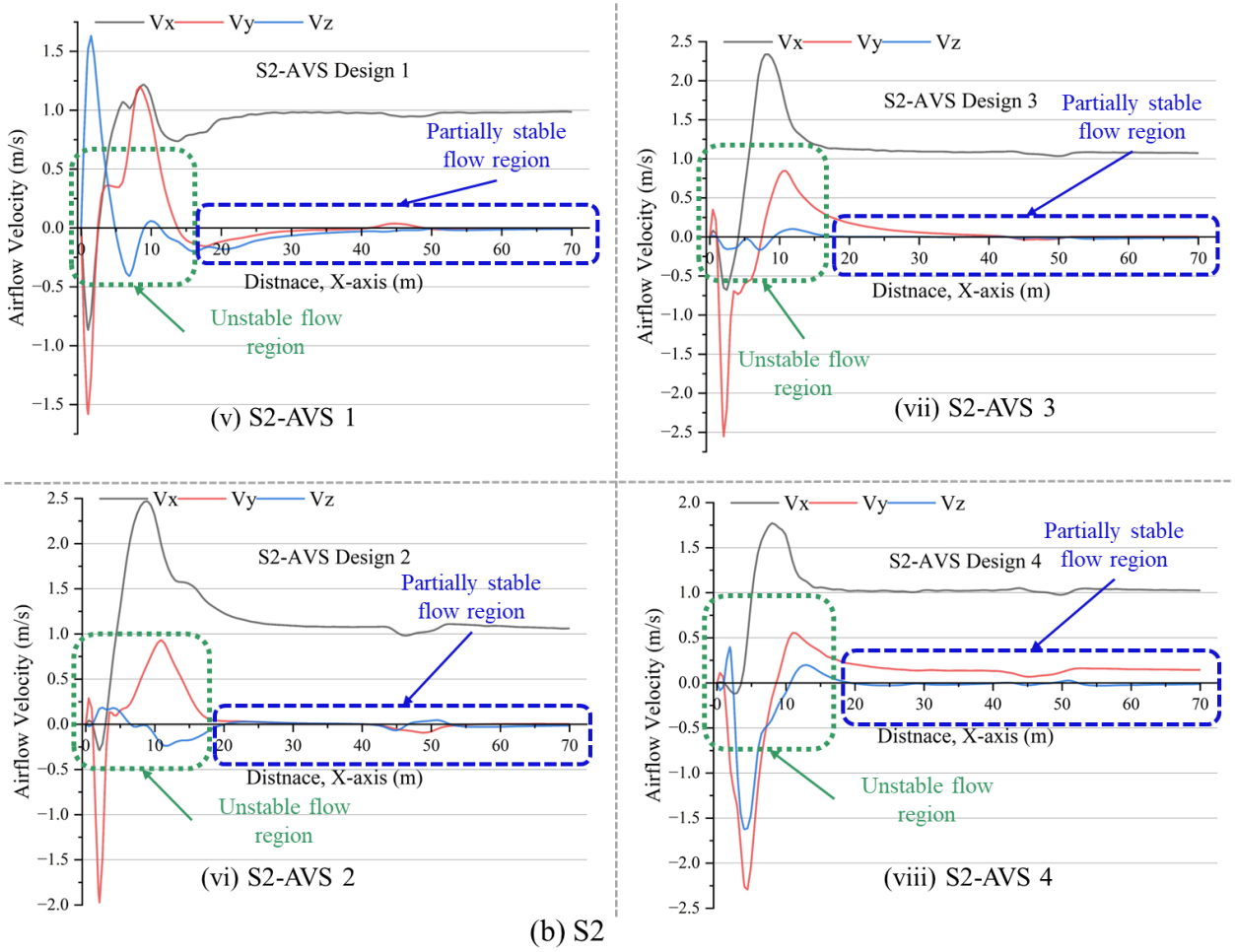

Fig. 19. Airflow velocity (Vx, Vy, Vz) in x, y, and z dimensions on the line monitors (a) S1 and (b) S2

4.1.6.2. Airflow velocity vectors distribution on monitoring planes

The airflow vectors demonstrate the direction of airflow at each monitoring plane in both scenarios, as shown in Fig. 20. (a and b). These vectors enhance the understanding of airflow dynamics across all monitoring planes within the various AVS designs. The blue, red, and green dots on the monitoring planes represent data monitoring points, whereas the yellow circles indicate the eddies present on the monitoring planes.

The (i) S1-AVS 1 exhibits notable eddy formation adjacent to the left-side wall at a distance of 20 m. It subsequently developed into two eddies at depths of 30, 40, and 50 m. Substantial eddies formed at 60 m and 70 m, partially obscuring the drift. In (v) S2-AVS 1, no eddy was observed at 10 m due to the absence of the DPE. A minor eddy was formed in the lower left section of the drift. This eddy subsequently expanded in size, encompassing nearly the center of the drift from 30 to 70 m.

The (ii) S1-AVS 2 displays two minor eddies positioned on the left and right-side walls at a depth of 20 m. No eddies were observed at depths of 30 and 40 m. Two minor eddies subsequently formed on the upper left and right sides of the drift at 50 m, merging into a single eddy that encompassed both AVS at 60 m. The significant eddy moved downhill, affecting the center of the drift at 70 m. The (vi) S2-AVS 2 exhibits no eddy at a distance of 10 meters. An inconsequential eddy developed near the floor at 20 m, subsequently

intensifying at 30 and 40 m. At 50 m, the eddy dissipated; however, at 60 and 70 m, a minor eddy was observed along the upper left-side wall of the drift.

The (iii) S1-AVS 3 exhibits two minor eddies located near the left and right walls at a depth of 20 m. An eddy was observed at 30 m along the left-side wall of the drift. A minor eddy also formed near the roof at altitudes of 40, 50, and 60 m. An eddy was observed below the AVS ducts at a depth of 70 m. The (vii) S2AVS 3 shows an absence of eddies at depths of 10, 20, and 30 m, respectively. An eddy was observed along the right-side wall of the drift at a depth of 40 m. At 50 m, the eddy shifted to the lower left wall of the drift and decreased in size. The eddy propagated near the roof at altitudes of 60 and 70 meters.

The (iv) S1-AVS 4 reveals the existence of two eddies at a depth of 20 m: a larger eddy adjacent to the left side wall and a smaller eddy located near the right-side wall. An eddy formed at 30 m from the left wall of the drift. The eddy increased in size and remained at the center of the drift at depths of 30, 40, 50, 60, and 70 meters, respectively. The (viii) S2-AVS 4 exhibits no eddies at depths of 10, 20, and 30 meters, respectively. A small eddy was observed along the left-side wall at a depth of 40 m. At a depth of 50 m, the eddy shifted to a lower center, near the base of the drift. At 60 m, the eddy formed between both ducts and near the roof; however, at 70 m, it expanded in size and occupied the center of the drift.

The airflow study reveals significant differences in eddy production and propagation across the AVS designs. The designs of AVS 1 and 4 generally exhibit more pronounced and persistent eddy formations, with eddies originating close to the walls and extending towards the center of the drift. In contrast, AVS 2 and 3 configurations exhibit a diminished quantity of small eddies, marked by a postponed initiation and constrained impacts, likely due to modifications in design. The findings underscore the influence of AVS design on airflow dynamics and its implications for the effectiveness of drift ventilation.

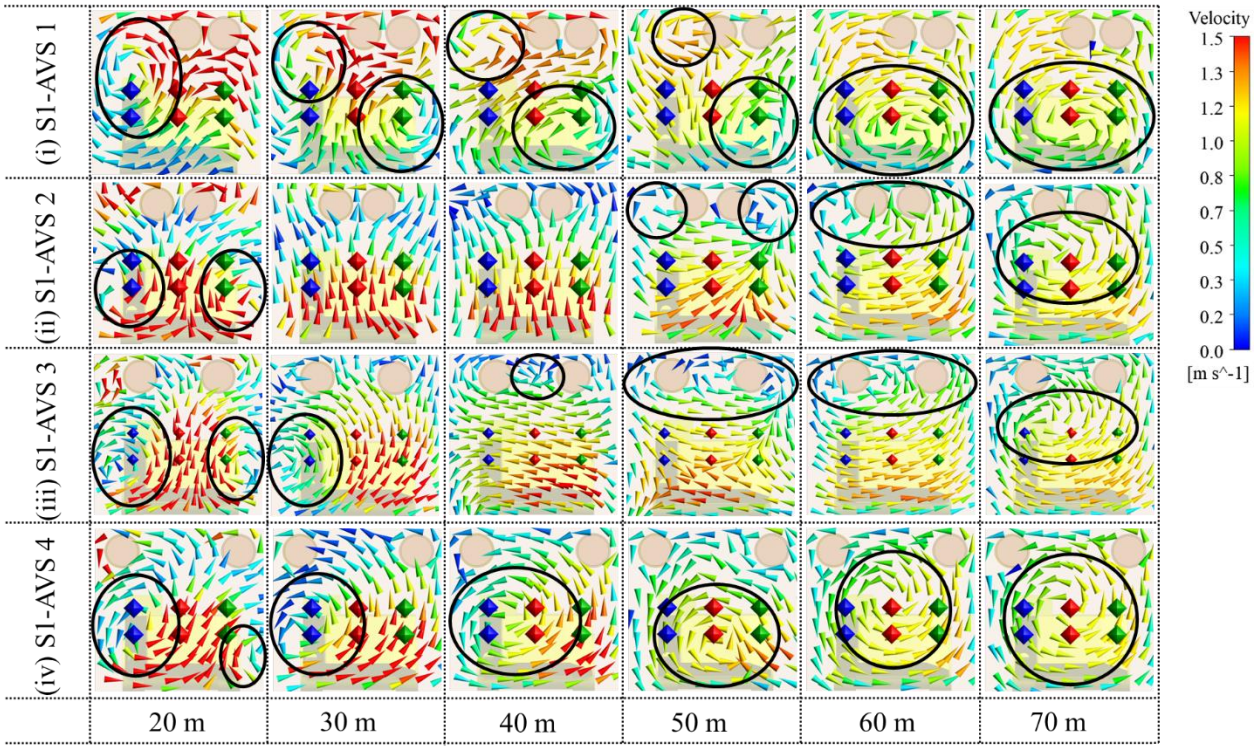

(a) S1

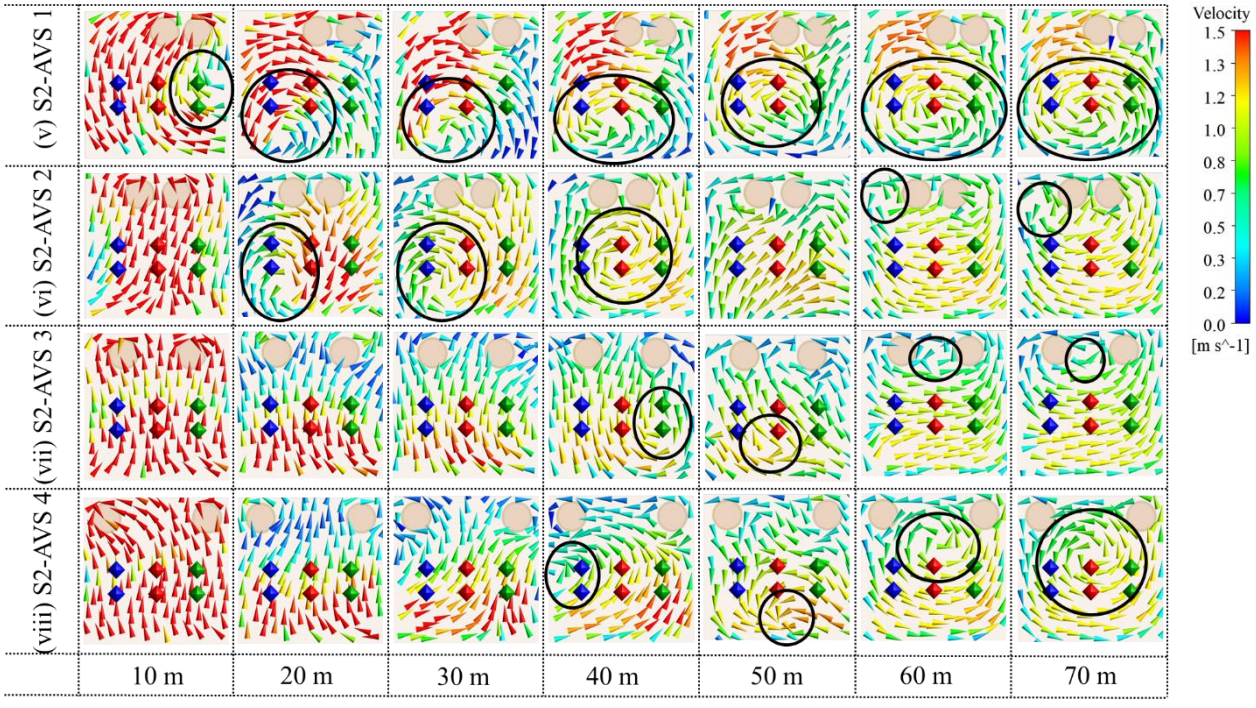

(b) S2

Fig. 20. Airflow vectors representation on monitoring planes (a) S1 and (b) S2

4.1.6.3. Analysis of PM contours

The PM contours illustrate the distribution characteristics on the monitoring planes across both scenarios and each AVS design, as shown in Fig. 21 (a and b). The PM contours offer an evaluation of areas with the highest likelihood of PM exposure.

Elevated PM concentrations are observed in the upper left quadrant of (i) S1-AVS 1, particularly around the AVS ducts and near the right wall and floor, within a range of 20 to 40 m. The PM concentration is consistent around the AVS but varies near the left wall between 50 and 70 m. The (v) S2-AVS 1 demonstrates insufficient PM concentration within the range of 10 to 40 m due to the placement of the DPE within the temporary dumpsite. At 50 m, the concentration of PM is located near the lower corner of the right wall. At 60 to 70 m, the PM concentration starts to extend from the right wall to the left wall along the floor.

In (ii) S1-AVS 2, the PM concentration is elevated around the AVS ducts and at the floor at 20 m, with higher PM concentrations persisting near the floor between 30 and 50 m. The concentration of PM remained high along the floor and the left-side wall between 60 and 70 m. In (vi) S2-AVS 2, there is no PM concentration observed between 10 and 40 m. Nonetheless, the PM concentrations persisted in the upper right quadrant at 50 m, subsequently shifting from the right side to the left side between 60 and 70 m.

In (iii) S1-AVS 3, the PM concentration is elevated around the AVS ducts and adjacent to the left-side wall and floor at 20 m, with higher PM concentration maintained near the left-side wall and floor between 30 to 70 m. (vii) S2-AVS 3 exhibits a partial concentration of PM ranging from 10 to 40 m, attributed to a significant vortex zone within the airflow field. An extensive concentration of PM was observed in the upper right corner at 50 m, subsequently shifting from the right side to the left side between 60 and 70 m.

In (iv) S1-AVS 4, the PM concentration is elevated along the left-side wall and near the floor at 20 m, persisting at the floor level at 30 m. The PM concentration was consistently high at the left wall and floor within the range of 40 to 70 m. In (viii) S2-AVS 4, there is no PM concentration observed between 10 and 40 m. PM concentrations were primarily localized near the roof and right-side wall at 50 m, subsequently spreading from the right side to the left side between 60 and 70 m, thereby covering the entire monitoring plane.

The PM contours exhibited distinct distribution characteristics across the analyzed AVS designs and in both scenarios. In S1, the airflow field exhibits greater turbulence, resulting in frequent transmission of PM concentration between the monitoring planes. In S2, the placement of DPE constrained the dispersion of PM on monitoring planes. The designs of AVS 2 and 3 demonstrate improved control over PM dispersion in the drift, thereby decreasing potential PM exposure to miners.

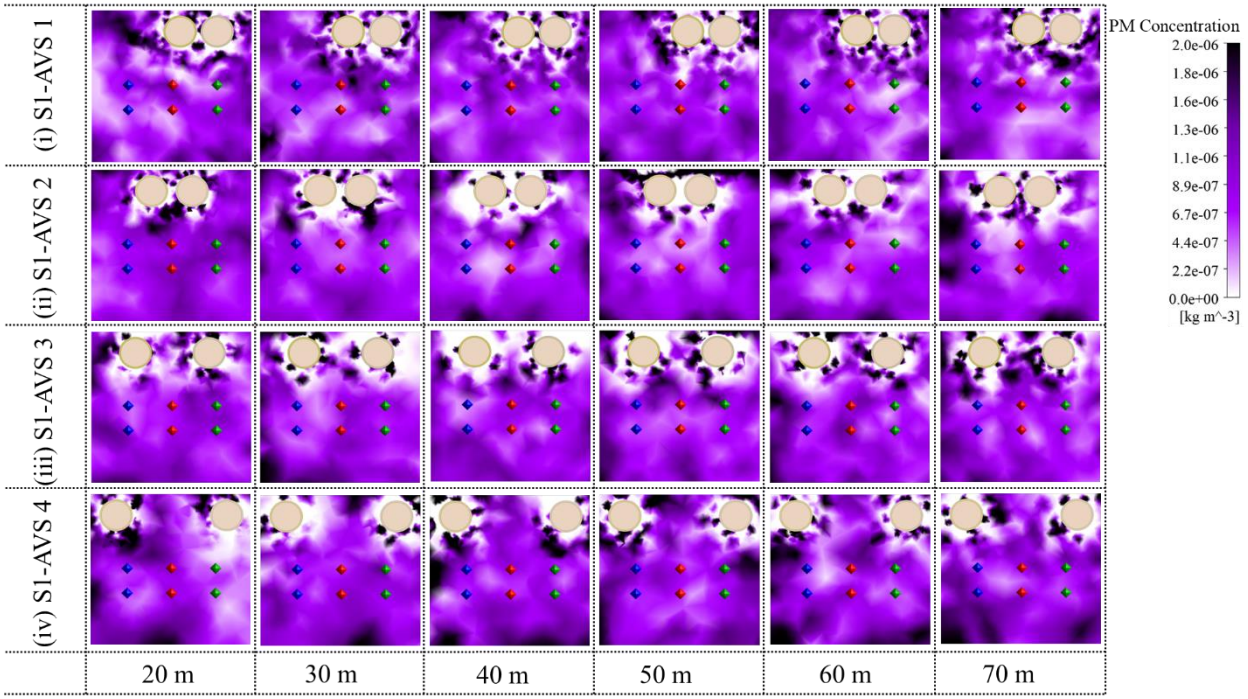

(a) S1

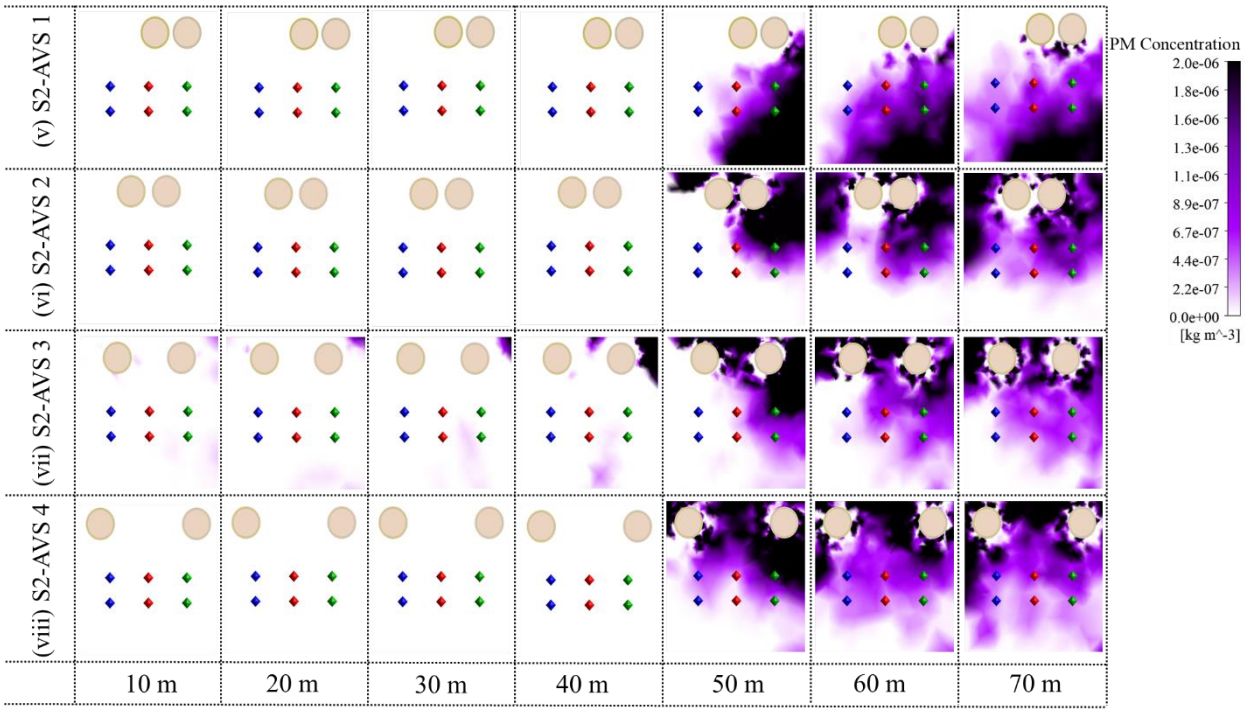

(b) S2

Fig. 21. PM concentration on monitoring planes (a) S1 and (b) S2

4.1.6.4. Spatial-temporal distribution characteristics of PM

The spatiotemporal distribution characteristics of PM offer insight into its temporal distribution in the drift. The AVS designs in both scenarios, illustrated in Fig. 22 (a and b), are assessed to determine the optimal design for reducing PM exposure to miners in the drift.

In (i) S1-AVS 1, most PM concentrations moved close to the ceiling, covering 20 m in 5 s. The PM concentration exceeded 40 m, with levels concentrated near the roof. In 15 s, it traveled over 50 m and

accumulated in the temporary dumpsite. After 60 s, the PM traversed over 70 m and exited the drift. In (v) S2-AVS 1, the PM emitted from the DPE tailpipe escaped the drift outlet within 60 s; however, the PM generated by DPE unloading the muck progresses slowly due to the lack of direct airflow in the area. The PM exited the temporary dumpsite in 120 s, while the LHD tailpipe exhaust remained unchanged. In 180 s, PM covered most of the temporary dumpsite and accumulated in the drift. Within 300 s, the PM from the unloading operation combined with the PM from the LHD tailpipe and exited through the drift outlet.

In (ii) S1-AVS, PM traveled approximately 30 m in 5 s, with most PM concentrations located near the floor. Within 15 s, the PM concentration attained 50 m, maintaining a concentrated presence near the floor during transit. Within 30 s, the PM accumulated in the temporary dumpsite and reached the drift outlet. Within 60 s, the PM advanced further into the temporary dumpsite. In (vi) S2-AVS 2, both the PM generated by unloading and the PM emitted from the LHD tailpipe exited the drift outlet within 60 s. However, the LHD unloading PM partially covered the temporary dumpsite. In 120 s, the PM at the rear of the LHD mixed with tailpipe exhaust PM. The PM concentration exhibited minimal variation at 180 and 300 s, and the transition of PM from the temporary dumpsite to the mine drift exit was more gradual.

In (iii) S1-AVS 3, most PM concentrations accumulated in front of the LHD and traveled less than 30 m in 5 s. Within 15 s, the PM concentrations attained 40 m and were predominantly located near the floor. Within 30 s, the PM concentration reached 60 m but did not accumulate in the temporary dumpsite. Within 60 s, the PM accumulated within the temporary dumpsite and subsequently exited through the mine drift outlet. In (vii) S2-AVS 3, the PM from unloading departed the temporary dumpsite in anti-flow, while the PM from the LHD tailpipe exited from the mine drift outlet within 60 s. At 120 s, the PM was concentrated above the LHD and near the roof at the temporary dumpsite, while the LHD tailpipe exhaust PM was transmitted along the right-side wall and roof. In 180 s, the DPE unloading PM crossed 30 m in the antiflow direction, nearly reaching the temporary dumpsite. Over a period of 300 s, the concentration of PM remained relatively stable, with PM dispersing from the temporary dumpsite in two simultaneous directions: towards the working face and towards the drift exit.

In (iv) S1-AVS 4 PM, the travel distance was approximately 30 m over a duration of 5 s, showing elevated concentrations near the floor. The PM concentrations reached 40 m within 15 s in the mine drift and remained close to the ground. Over a duration of 30 s, the PM concentration moved 60 m in the mine drift and began to accumulate in the temporary dumpsite. The PM accessed the temporary dumpsite, covered the mine drift, and exited through the mine drift outlet within 60 s. In (viii) S2-AVS 4, the PM was collected within the temporary dumpsite, and the majority travelled along the right-side wall of the mine drift and near the roof within 60 s. The transition of PM from the temporary dumpsite to the mine drift outlet was nearly identical at 120, 180, and 300 seconds.

The spatiotemporal analysis of PM distribution demonstrates varied patterns across different AVS designs in both scenarios. AVS 1 and 4 typically exhibit decreased PM mobility and heightened accumulation at the temporary dumpsite. Conversely, AVS 2 and 3 configurations demonstrate improved PM dispersion and

accelerated drift escape due to optimized airflow patterns and reduced accumulation at the temporary dumpsite. The primary objective of AVS design is to minimize PM exposure, thereby ensuring a cleaner and safer working environment for miners.

(a) S1

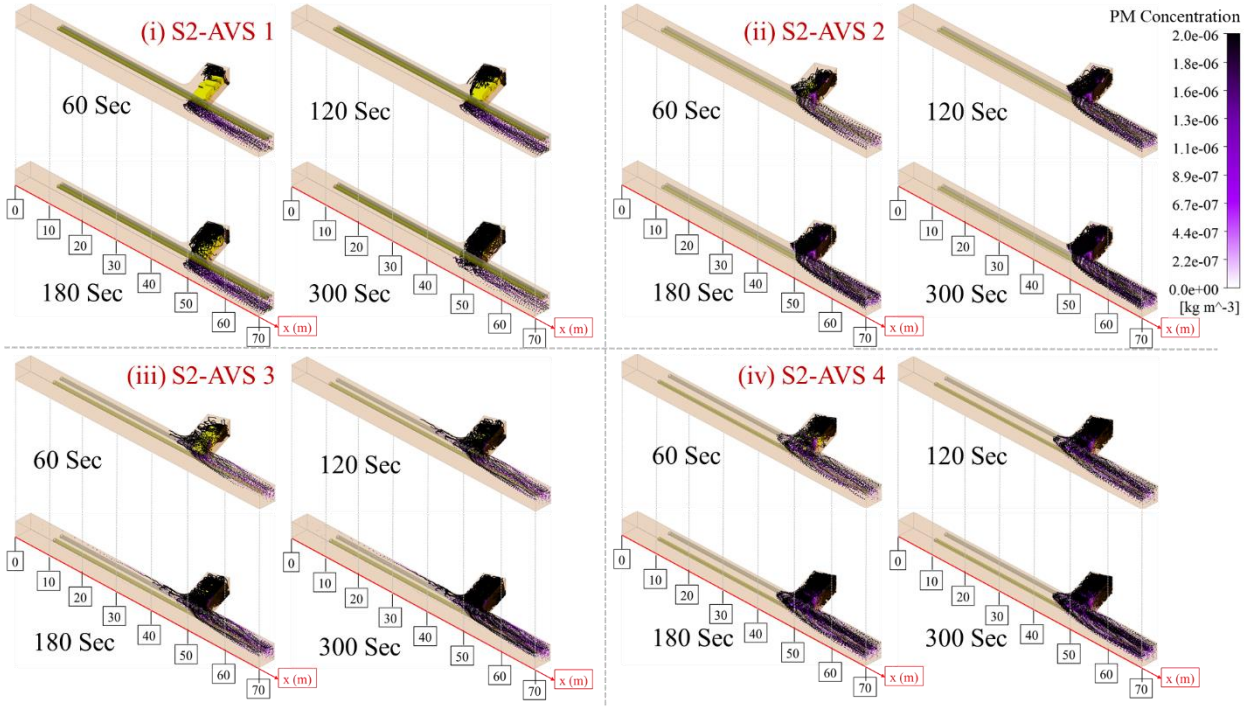

(b) S2

Fig. 22. Spatiotemporal PM distribution in (a) S1 and (b) S2

4.1.6.5. Comparative analysis of PM diffusion rate under all AVS-Designs 1 – 4

The PM diffusion rate was determined based on an area-weighted average along the mine drift in both scenarios. The PM diffusion rate was calculated under all four AVS-Designs 1 – 4 and a mathematical polynomial function was proposed for each AVS-Design to satisfy the PM dilution.

4.1.6.5.1. PM diffusion rate in S1

Fig. 23. (a) illustrates the PM behavior under all AVS-Designs 1 – 4 in S1. The trend line follows nearly similar pattern under the influence of S1 AVS 1, 2, and 3. However, the concentration of PM along the distance varies and S1 AVS 2 shows the least PM concentration along the mine drift, followed by S1 AVS 3, and in last S1 AVS 1. On the other hand, the PM trend line under S1 AVS 4 indicated minimal decline throughout the mine drift. The mathematical functions describing PM behavior along the distance are as follows: $PM_{S1\ AVS1}$ = -1E-12x^4 + 2E-10x^3 - 1E-08x^2 + 4E-07x - 3E-06, $PM_{S1\ AVS2}$ = 1E-11x^3 - 1E-09x^2 + 5E08x + 2E-07, $PM_{S1\ AVS3}$ = -6E-13x^4 + 1E-10x^3 - 8E-09x^2 + 2E-07x - 1E-06, and $PM_{S1\ AVS4}$ = -8E-13x^4 + 2E-10x^3 - 1E-08x^2 + 3E-07x - 2E-06, respectively.

4.1.6.5.2. PM diffusion rate in S2

Fig. 23. (b) illustrates the behavior of PM across all AVS Designs 1 - 4 in S1 and S2. The trend line indicates continuous fluctuations influenced by these AVS Designs. Notably, the concentration of PM varies with distance, with S1 AVS 3 exhibiting the lowest PM concentration along the mine drift, followed by S1 AVS 2, S1 AVS 4, and S1 AVS 1. The mathematical functions that describe PM behavior along the distance are as follows: $PM_{S1\ AVS1}$ = -3E-11x^4 + 8E-09x^3 - 7E-07x^2 + 3E-05x - 0.0004, $PM_{S1\ AVS2}$ = 1E-10x^3 - 2E-08x^2 + 1E-06x - 2E-05, $PM_{S1\ AVS3}$ = 4E-11x^4 - 9E-09x^3 + 8E-07x2 - 3E-05x + 0.0004, and $PM_{S1\ AVS4}$ = 3E-11x^4 - 7E-09x^3 + 6E-07x^2 - 2E-05x + 0.0004, respectively.

Consequently, in both S1 and S2, the lowest observed PM concentrations among all AVS Designs were recorded under the influence of AVS 2 and AVS 3, respectively. Given the dynamic operating nature of the LHD, it is recommended that the AVS 2 design be adopted for both scenarios to achieve the least PM concentration along the mine drift.

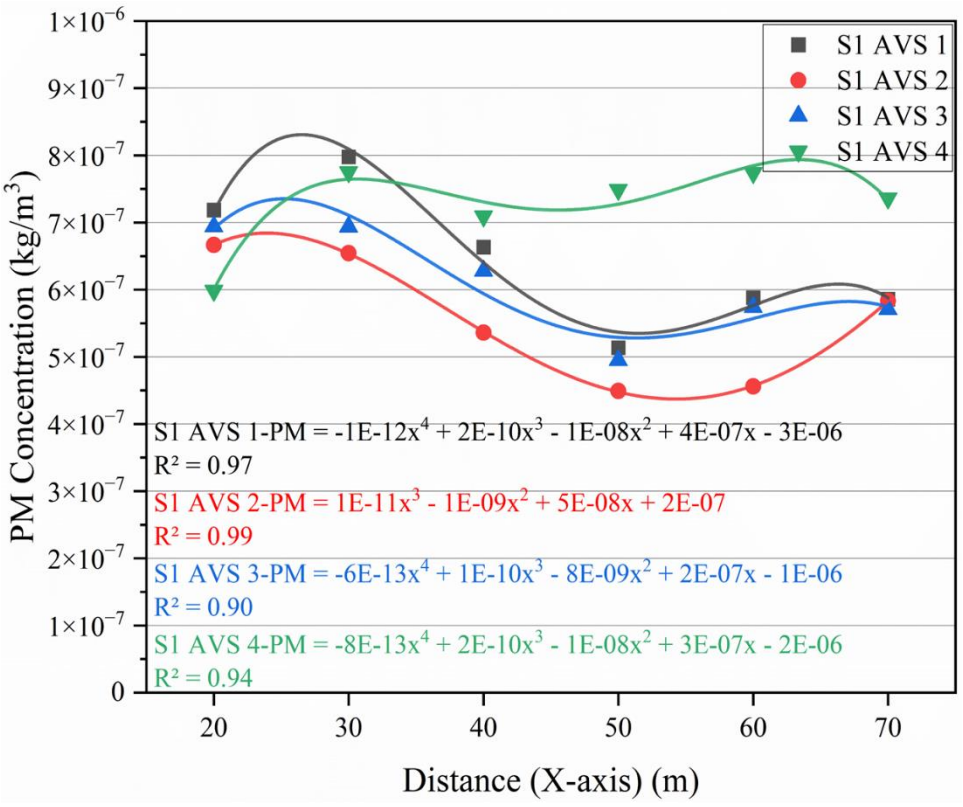

(a) PM concentrations in S1-AVS 1-4

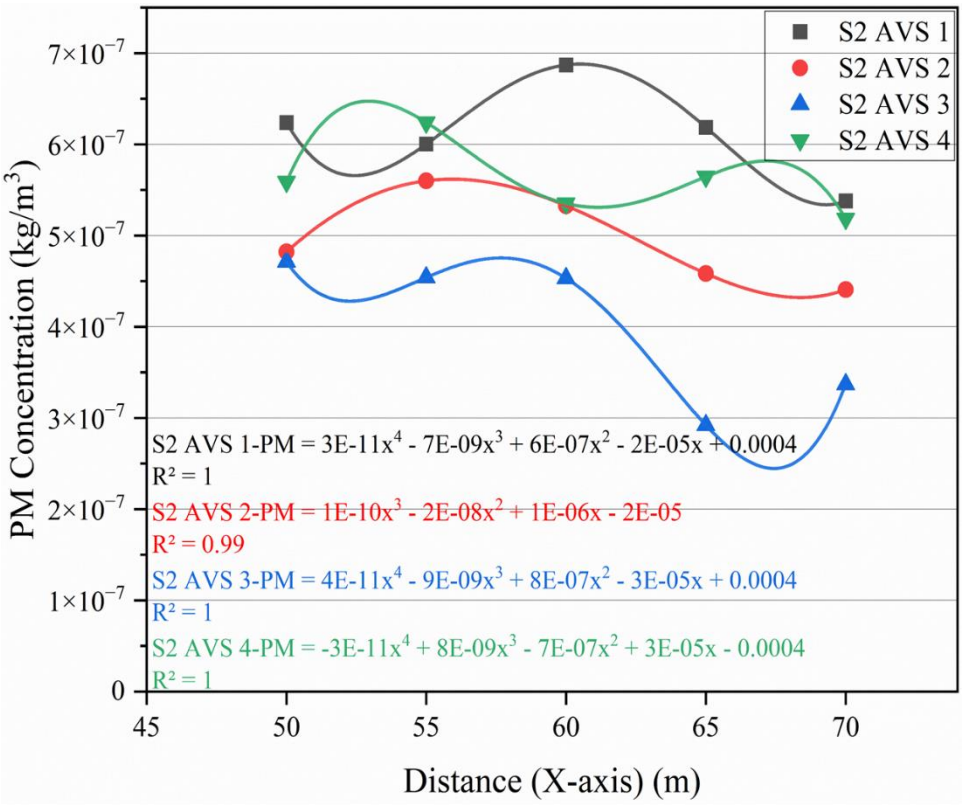

(b) PM concentrations in S2-AVS 1-4

Fig. 23. Comparative analysis of PM diffusion under all AVS-Designs 1 – 4

4.1.7. Filter Analysis by SEM/EDS (Jeol JSM-IT200)

The SEM/EDS analysis showed that the mesh filter contains five elements in total while the major elemental composition was comprised of two elements that are Fluoride (F) and Carbon (C). Although the Oxygen (O), Aluminum (Al), and Silica (Si) traces were also found but their mass concentration was less than 6% from the total mass concentration. Thus, these elements were neglected in further analysis. The mass concentration of F and C at each monitoring point on the mesh filter is compiled in Table 2. The F concentration remained between 71 and 72 percent, while the C concentration fluctuated between 22 and 24 percent. In total, these two elements were responsible for nearly 95 percent of the total mass concentration collected on the mesh filter.

Table 2. Elemental mass concentration on mesh filter

Elements	**Monitoring Points**					**Average**
	1	**2**	**3**	**4**	**5**	
Floride (%)	71.81	72.65	71.11	72.08	71.51	71.83
Carbon (%)	22.99	23.35	22.89	22.92	23.49	23.12

Fig. 24. (a) highlights the peaks of each element traced by the SEM/EDS with related intensity counts and energy dispersive X-ray. The highest peak is allocated to F, and the second highest peak represents C. The mesh filter morphology image observed at the scale of 10 µm is depicted in Fig. 24. (b), while focusing on the mesh filter monitoring point 1 (center). The gray scale image shows the particles distribution on the mesh filter. Fig. 24. (c, and d) depicts the elemental distribution of C and F, respectively. The distribution of all the elements collected on the mesh filter is shown in Fig. 24. (e). Similarly, the figures and images on the other monitoring points on the mesh filter showed similar results with negligible differences. Thus, the mass concentration details along with minor differences of each monitoring point on the mesh filter were provided in Table 2.

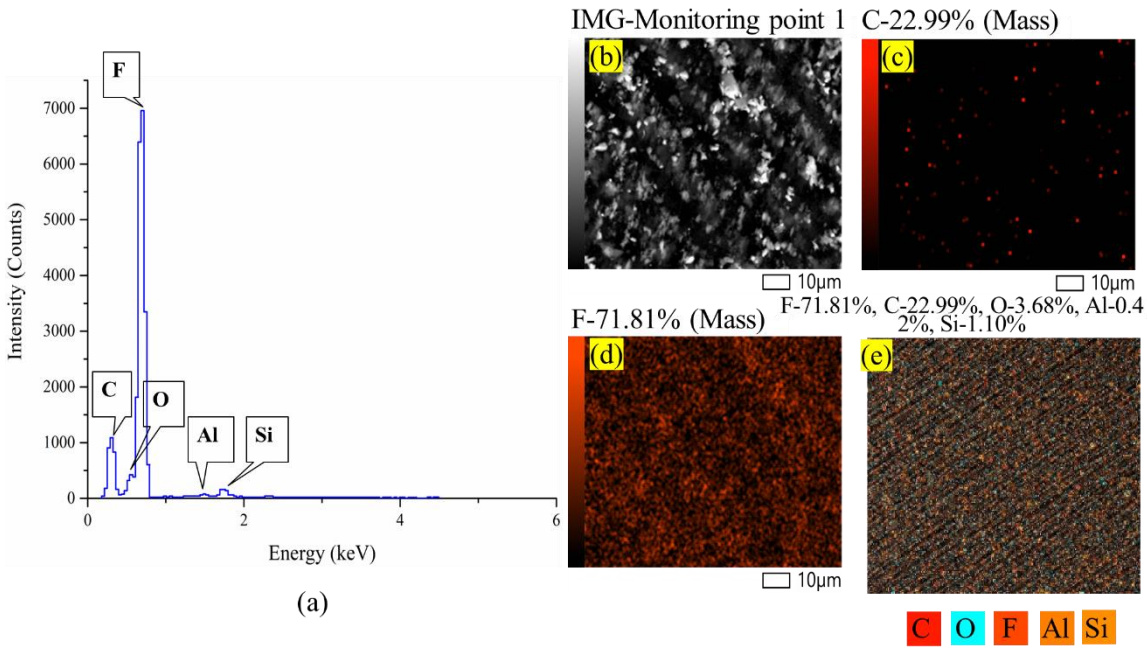

Fig. 24. SEM/EDS analysis of mesh filter (a) elemental mass concentration peaks, (b) morphological distribution at point 1, (c) Carbon particles, (d) Floride particles, and (e) all elemental particles

4.1.8. Numerical simulation validation with field experimentation

To verify the accuracy and reliability of the simulation results based on the field experimental data, the cross-sectional areas in the mine drift and haulage drift were selected for all three conditions. The six corresponding measuring points were established at each monitoring cross-section, among which three points were at breathing zone 1.5 m and other three points were at breathing zone 2.2 m.

Plane and line elements were generated in the CFD-POST in accordance with specifications, providing multiple measurement points on the corresponding cross sections. The variable can be set to either Velocity or Particle Mass Concentration within the software, facilitating the acquisition of simulated airflow velocity or PM concentration at designated measurement points. The data from each measurement location was accurately recorded to facilitate the effective operation of airflow and PM measurement. After the measurements were completed, the detection data was processed to determine the variable values at each measurement point.

The simulated values at various monitoring points across all three conditions were compared to the measured values, and the relative error values were computed. Fig. 18. (a, c, e) represents a comparison of measured and simulated results for airflow and Fig. 18. (b, d, f) depicts PM concentrations along with relevant errors. In engineering applications, a relative error of 20% between numerical simulations and experimental results is typically deemed acceptable [157, 158]. The relative error distribution between actual and simulated airflow velocity in conditions 1, 2, and 3 remained below 10%. On the other hand, the relative error between experimental and simulated PM concentration in all three conditions was below 12%. The numerical simulation results were deemed reliable for simulating the distribution of PM produced and emitted during muck loading and unloading operations conducted by LHD.

Discrepancies between measured and simulated results may result from variations in boundary conditions. Wall roughness influences airflow characteristics in real-world scenarios, despite the simplifications in modeling it through CFD. The disturbance in airflow caused by the presence of individuals during data recording may also contribute to variations in the data. The data collection process during the field test necessitated manually holding the monitors at designated monitoring points, a task that poses significant challenges for human operators. The numerical simulation model offers estimates of concentration levels at designated monitoring points within the computational domain, specified by their x, y, and z coordinates. The identified factors may have contributed to discrepancies in the results.

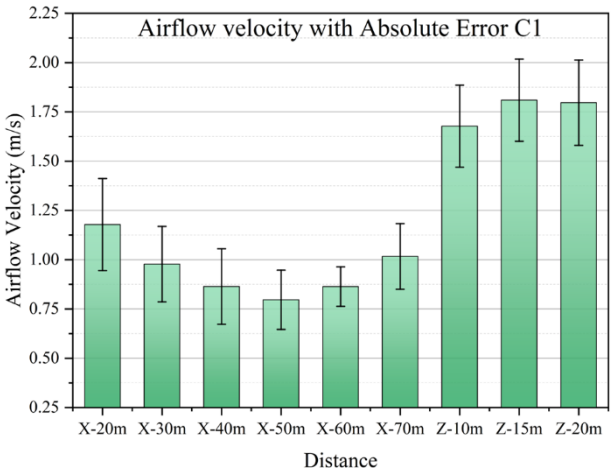

(a) Airflow comparison in C1

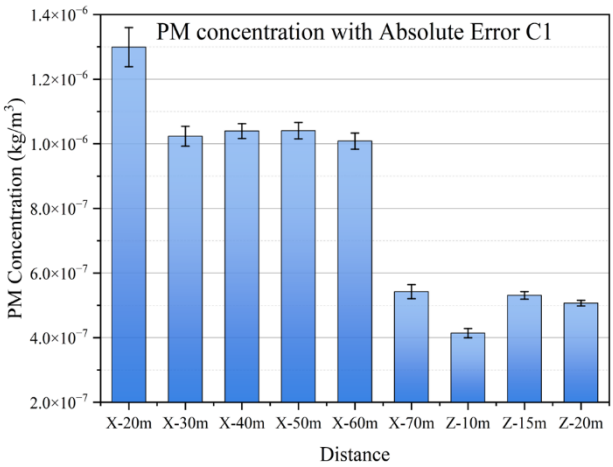

(b) PM comparison in C1

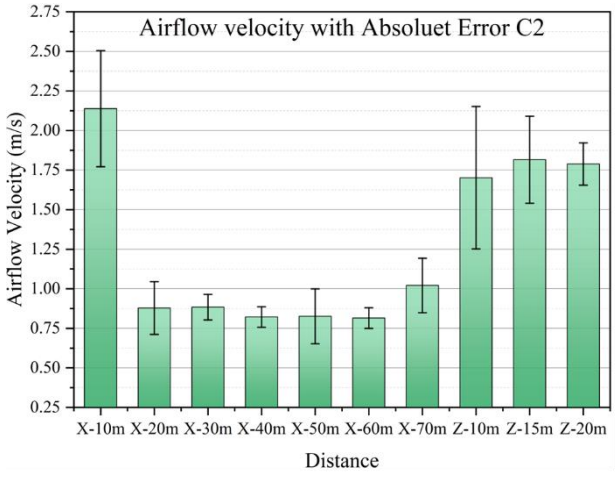

(c) Airflow comparison in C2

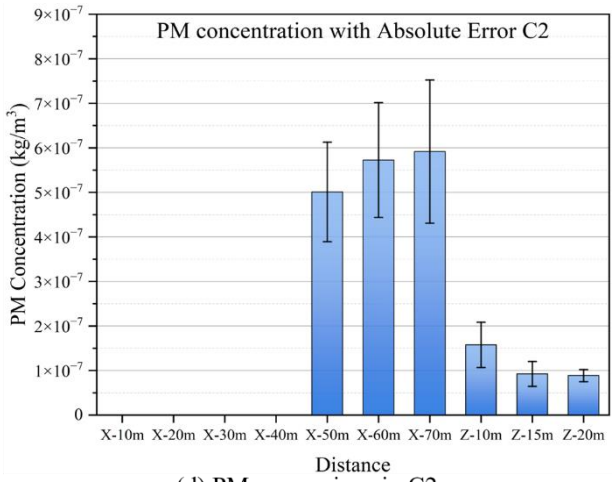

(d) PM comparison in C2

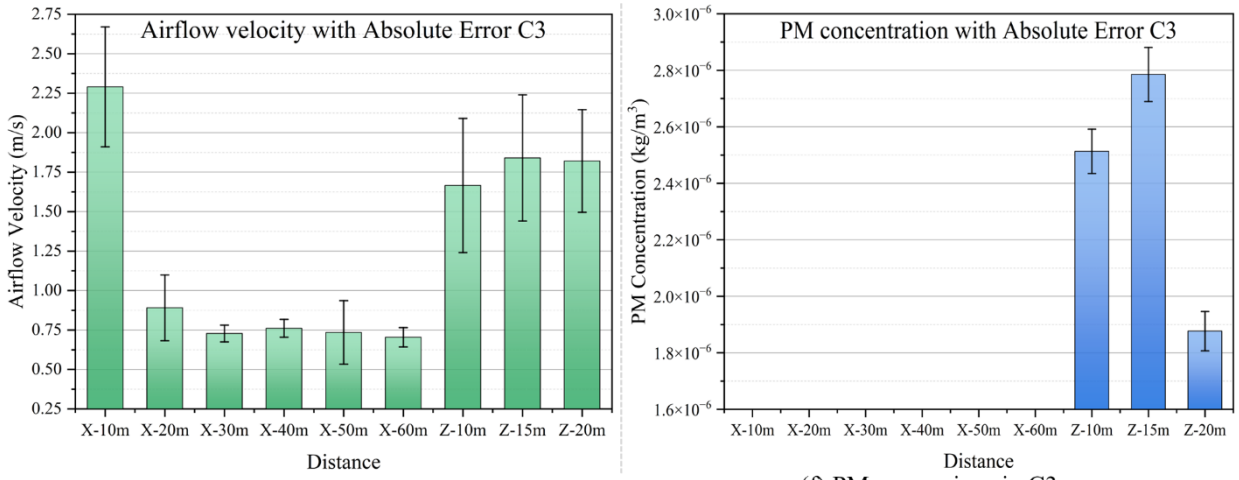

(e) Airflow comparison in C3 (f) PM comparison in C3

Fig. 25. Comparison of experimental and simulation results along with absolute error:(a) airflow in C1, (b) PM in C2, (e) airflow in C3, (f) PM in C3

4.2. Discussion

Based on the results above, the diffusion characteristics of PM are mainly dependent on the volumetric airflow and the AVS design. This study highlights the significance of airflow regions within the breathing zones of DPE operators and personnel involved in experimental data collection. The airflow turbulence and PM diffusion is mainly controlled by these airflow regions. Thus, the development of these regions provides insight into the potential exposure of underground miners. A few studies [24, 134, 159] conducted numerical simulation of DPM in underground mines during different idling conditions under SDF-AVS. The airflow streamlines were used to depict the overall airflow around the diesel vehicles in different idling conditions. These results showed a complex sequence of airflow streamlines without highlighting the shapes and dimensions of the airflow field.

In OC-1, the LHD operator encountered the highest concentration of PM in C2, followed by C1 and C3. The results presented in Fig. 17 indicate that C1 and C2 achieved the lowest and nearly identical PM concentrations at volumetric airflow Q = 17 m³/s and 20 m³/s. Conversely, a volumetric airflow Q = 15 m³/s replaced the 20 m³/s in C2. Therefore, across all three conditions, Q = 17 m³/s demonstrated a sufficiently effective capacity to reduce PM concentrations. In addition, the volumetric airflow required based on the engine power, as discussed in problem statement [43, 44] could be achieved under Q = 17 m^3/s and 20 m^3/s. Furthermore, continuously adjusting the AVS airflow during LHD maneuvering would be impractical. For instance, several studies [42, 160-162] aimed to optimize airflow volume based on numerical simulation results, which indicated that increasing the existing airflow volume would enhance pollutant mitigation. For this reason, the study recommends a volumetric airflow of Q = 17 m³/s as the optimal airflow for OC-1. As it was determined, C3 is the least critical condition among those of OC1. To conserve computational resources and time, only the first two conditions of OC-1 were selected and subsequently renamed S1 and S2 for OC-2.

The AVS designs in OC-2 significantly influence the intensity of airflow turbulence and the spatiotemporal distribution of PM in the mine drift of underground mines. Fig. 19. presents a comparative analysis of the lengths of unstable flow regions across all four AVS designs in S1 and S2. It was noted that the most highly unstable region is found in S1-AVS 3, followed by S1-AVS 1, S1-AVS 4, and S1-AVS 2, respectively. In contrast, the lengths of the unstable flow regions in S2 are nearly identical across all four AVS designs. The positioning of the LHD and AVS duct outlets primarily influences the turbulence within the airflow field and PM migration in the mine drift. As the AVS is an important component of underground mine face ventilation, several studies [24, 26, 32, 41, 163, 164] optimized the length of the AVS (distance between working face and duct outlet) along with variations in DDH-AVS volumetric airflows, to reduce PM concentration. However, these studies were conducted in underground coal mines, where PM was generated by mechanical excavation, while DPM was emitted from diesel vehicles idling at constant speeds on the mine roadways. To the best of the author's knowledge, no studies have been conducted to investigate PM emissions from multiple sources under DDF-AVS conditions in a polymetallic underground mine.

In contrast, the findings of this thesis provide a reasonable justification for adopting the configuration of volumetric airflow and AVS design in similar mining operating conditions. However, it is important to note that the mine environment may vary due to regional differences, climate, AVS, and other operational environmental parameters. Therefore, adjustment of the proposed models is recommended for new underground mines.

5. Applications and Limitations

The following sections present the applications of the study in predicting the critical parameters. The significance of this study in predicting the intricate airflow patterns and PM migration characteristics plays a pivotal role in mitigating the miners' exposure to hazardous pollutants. Additionally, the limitations inherent in the current work are carefully outlined, highlighting areas for future investigations.

5.1. Applications of current research work

- By integrating field measurements with CFD simulations, this study provides a framework for designing and optimizing AVS in underground mines. This approach enables the identification of airflow patterns, detection of stagnation zones, and assessment of ventilation efficiency, leading to improved air quality and reduced exposure to harmful particulates for miners.
- The model developed can be applied to establish real-time air quality monitoring systems within mines. Incorporating sensors and predictive models allows for continuous assessment of PM2.5 levels, facilitating timely interventions to maintain safe working conditions and comply with occupational health standards.
- The findings offer valuable insights for policymakers and regulatory bodies aiming to establish or update air quality standards in mining operations. By providing validated models, this research supports the formulation of evidence-based regulations to safeguard miners' health and environmental integrity.
- The comprehensive analysis of ventilation dynamics and PM dispersion serves as an educational resource for training mining engineers and safety personnel. Incorporating these findings into curricula and professional development programs can enhance understanding of ventilation management and occupational health practice.
- The principles and models developed in this study can be adapted to other underground industries, such as tunnels, subways, and underground storage facilities. Applying these insights can improve ventilation design and air quality management in various underground infrastructures.
- The SEM/EDS analysis could be used to identify and predict the elemental concentrations of fine and ultra fine particles in underground structures and the results could assist in estimating the potential health effects on the human body.
- Based on the results of this study, the calculation of required volumetric airflow and AVS designs can significantly influence the overall air quality, operating environment, and health and safety of the miners.

5.2. Limitations of current research work

- The present work ignored LHD vehicle engine load fluctuations during muck loading and unloading activities. Engine load directly impacts the revolutions per minute (RPM), which then changes the PM emission rates from diesel engines. Usually, more engine load means more PM

emissions. Future studies should include real-time engine load data to more precisely evaluate and simulate PM emissions in deep mining conditions. Although this study addressed the spatial distribution and concentration of PM, it did not assess how long miners were exposed to high PM levels. Exposure duration is a key determinant of possible health effects on miners. Future research should include time-activity patterns of miners to evaluate cumulative exposure and related health hazards.

- This work did not investigate the link between ore transport rate and resulting PM levels. Important causes of PM production are mechanical ore handling techniques including transportation and unloading. Knowing how changes in ore transport rates affect PM levels can help one to reduce exposure. Future studies should investigate this link to create ideal scheduling and operational procedures for reducing PM emissions.
- Though the simulation examined all four AVS designs, field testing was done only under AVS 1. The dependability and relevance of the results would be improved by validating simulation findings with actual data across all suggested AVS designs. Future studies should seek to conduct thorough field tests for every AVS configuration to verify their efficacy in actual settings. Future studies that address these constraints will help to create a more complete picture of PM dynamics in underground mining settings and help to create more efficient plans to safeguard miner health and safety.
- Dealing with these constraints in future studies will help to provide a more complete picture of PM dynamics in the underground mine environment and support the creation of more efficient plans to safeguard miner health and safety.

6. Conclusion and Recommendations

Conclusively, the study has adopted a combination of field experimentation and numerical simulation to investigate the ≤PM2.5 emitted from multiple sources during LHD performing loading and dumping of ore in underground polymetallic mine. A series of airflow and PM monitoring has been conducted in the operational drifts of mine. Later, the field experimental data collected was used to validate the numerical simulation model.

6.1. Conclusions

This study has also been able to relate the PM transient levels with DPEs operating activities in underground mine. To the author's knowledge, no research has been done so far that develops a novel model which elaborates the PM spread over time and space emitted from multiple sources under DDF-AVS in a polymetallic underground mine. The thesis has drawn the following conclusions:

- A detailed comparison between the experimental and simulating airflow quantities (see OC-1) revealed that the airflow field comprised of specific regions, including "Backflow", "Vortex", "Multi direction and unstable flow", and "Same direction and stable flow", controls the PM diffusion and transposition. The existence of these dynamic airflow regions is unavailable for a naked eye during the field experimentation. As a result, this thesis has led to the foundation of identifying the positioning and dimensions of these airflow regions under different operating activities performed by DPEs in underground polymetallic mines. The insight into the dimensions and position of these regions significantly assists in predicting and controlling the PM concentrations in underground mines.
- The analysis of PM concentrations under all four volumetric airflows in OC-1 revealed that Q = 17 m^3/s significantly reduced the PM concentrations to 28.45%, 29.59%, and 20.63% in C1, C2, and C3, respectively. Thus, a correlation is proposed between the PM concentrations and lengths of the operational drifts of mine. A high value of correlation coefficient is achieved for all three operating conditions. For C1, C2, and C3 the proposed correlation coefficients are $R^2 = 0.91$, 0.96, and 0.91, respectively. The proposed equations can be used to predict the PM concentrations under similar mining conditions. The correlation equations given are:

$$\text{For C1, } PM = -0.0279x^2 - 3.8386x + 932.77 \quad (10)$$

$$\text{For C2, } PM = 29.326x - 1356.1 \quad (11)$$

$$\text{For C3, } PM = -6.2231x^2 + 120.9x + 1528.4 \quad (12)$$

- Similarly, another comparison between the experimental and simulated DDF-AVS designs (see OC-2) showed that the positioning of AVS 2 outlets substantially reduced PM concentration to 15.66% and 27% in S1 and S2, respectively. Thus, another correlation is proposed between the PM concentration and length of the mine drift based on the AVS designs. The proposed correlation coefficient under AVS 2 for both S1 and S2 is achieved as $R^2 = 0.99$. Based on the AVS design the

proposed equations can be adopted to predict the potential PM concentrations in resembling mining operating conditions. The equations of correlation are as follows:

$$\text{For S1, PM} = 1x10^{-11}x^3 - 1x10^{-09}x^2 + 5x10^{-08}x + 2x10^{-07} \quad (13)$$

$$\text{For S2, PM} = 1x10^{-10}x^3 - 2x10^{-08}x^2 + 1x10^{-06}x - 2x10^{-05} \quad (14)$$

- This study offers an integrated, spatial-temporal characterization of diesel exhaust and PMs, thereby contributing novel insights into the dispersion of the health-relevant aerosol exposure of underground miners.

6.2. Recommendations

Despite the predictive ability and close proximity with field experimentation of the spatiotemporal model, it is important to propose recommendations to enhance air quality management and health and safety of the miners.

- Enhancing volumetric airflow rates, specifically at 17 m^3/s, has demonstrated a substantial decrease in PM concentrations. The mining operating conditions must evaluate and modify the AVS to attain optimal airflow that controls PM dispersion during ore handling activities.
- The research determined that the positioning of AVS outlets significantly affects PM dispersion patterns. AVS design 2 exhibited a 15% decrease in PM concentrations during loading at the working face and a 27% reduction while discharging at temporary dumpsites. Mines are advised to implement AVS layouts that strategically situate outlets to efficiently channel airflow to minimize the miners' exposure.
- It is recommended to integrate real-time PM monitoring systems for the proactive management of air quality. These devices should be calibrated before field experimentation to ensure safe working conditions.
- The correlation equations developed between PM concentrations and mine drift lengths can function as predictive instruments for evaluating air quality under diverse operational scenarios. Mining engineers and ventilation experts should employ these models to predict PM concentrations and devise suitable mitigation solutions.
- Training sessions for LHD and UMT operators should prioritize best practices that reduce PM emission, including controlled loading and dumping operations. Furthermore, operational protocols must be amended to integrate insights into optimal ventilation techniques and equipment positioning to mitigate hazardous exposure.
- Regulatory authorities ought to revise guidelines and standards to acknowledge the significance of optimum airflow and AVS arrangements in managing PM concentrations. Regulations requiring systematic evaluation and modification of AVS based on scientific evidence can enhance health and safety standards for miners across the industry.

References

1. Timonen, H., et al., *Sources and composition of particulate matter in boreal arctic environment next to an active mining area.* Boreal Environment Research, 2018. **23**(1-6): p. 105-105–125.
2. Saarikoski, S., et al., *Particulate matter characteristics, dynamics, and sources in an underground mine.* Aerosol Science and Technology, 2018. **52**(1): p. 114-122.
3. Saarikoski, S., et al., *Sources and Characteristics of Particulate Matter at Five Locations in an Underground Mine.* Aerosol and Air Quality Research, 2019. **9**(12): p. 2613-2624.
4. Brake, D. *The growing use of hazardous primary ventilation systems in hard rock mines*. in *Proceedings Ninth International Mine Ventilation Congress*. 2009.
5. Bugarski, A.D., T.L. Barone, and J.A. Hummer, *Diesel and welding aerosols in an underground mine.* International Journal of Mining Science and Technology, 2020. **30**(4): p. 449-454.
6. Paluchamy, B., D.P. Mishra, and D.C. Panigrahi, *Airborne respirable dust in fully mechanised underground metalliferous mines – Generation, health impacts and control measures for cleaner production.* Journal of Cleaner Production, 2021. **296**: p. 126524.
7. McDonald, J.D., et al., *Source Apportionment of Airborne Fine Particulate Matter in an Underground Mine.* Journal of the Air & Waste Management Association, 2003. **53**(4): p. 386-395.
8. Kissell, F.N., *Handbook for dust control in mining*. 2003: US Department of Health and Human Services, Public Health Service, Centers ….
9. Lee, S.W., *Fine particulate matter measurement and international standardization for air quality and emissions from stationary sources.* Fuel, 2010. **89**(4): p. 874-882.
10. Schraufnagel, D.E., et al., *Air Pollution and Noncommunicable Diseases: A Review by the Forum of International Respiratory Societies' Environmental Committee, Part 1: The Damaging Effects of Air Pollution.* Chest, 2019. **155**(2): p. 409-416.
11. Hesterberg, T.W., et al., *Health effects research and regulation of diesel exhaust: an historical overview focused on lung cancer risk.* Inhalation Toxicology, 2012. **24**(sup1): p. 1-45.
12. Xu, Y., et al., *Assessment of personal exposure to environmentally persistent free radicals in airborne particulate matter.* Journal of Hazardous Materials, 2021. **409**: p. 125014.
13. Steiner, S., et al., *Diesel exhaust: current knowledge of adverse effects and underlying cellular mechanisms.* Archives of Toxicology, 2016. **90**(7): p. 1541-1553.
14. Vohra, K., et al., *Global mortality from outdoor fine particle pollution generated by fossil fuel combustion: Results from GEOS-Chem.* Environmental Research, 2021. **195**: p. 110754.
15. Forouzanfar, M.H., et al., *Global, regional, and national comparative risk assessment of 79 behavioural, environmental and occupational, and metabolic risks or clusters of risks in 188 countries, 1990–2013: a systematic analysis for the Global Burden of Disease Study 2013.* The Lancet, 2015. **386**(10010): p. 2287-2323.
16. Lee, J.-E., H.J. Lim, and Y.-Y. Kim, *Publication trends in research on particulate matter and health impact over a 10-year period: 2009–2018.* Environ Anal Health Toxicol, 2021. **36**(1): p. e2021005-0.
17. Li, Z., et al., *A novel approach for assessing the spatiotemporal trend of health risk from ambient particulate matter components: Case of Hong Kong.* Environmental Research, 2022. **204**: p. 111866.
18. Stege, T.A.M., et al., *Development and usability of educational material about workplace particulate matter exposure.* BMC Public Health, 2021. **21**(1): p. 198.
19. Bugarski, A.D., et al., *Diesel aerosols and gases in underground mines; guide to exposure assessment and control.* 2011.

20. WHO, *IARC (International Agency for Research on Cancer): DIESEL ENGINE EXHAUST CARCINOGENIC, Press release no. 213*. 2012: Lyon, France. p. 4.

21. Yu, Y., et al., *Adverse outcome pathway of fine particulate matter leading to increased cardiovascular morbidity and mortality: An integrated perspective from toxicology and epidemiology.* Journal of Hazardous Materials, 2022. **430**: p. 128368.

22. Gautam, S., et al., *Particulate matter pollution in opencast coal mining areas: a threat to human health and environment.* International Journal of Mining, Reclamation and Environment, 2018. **32**(2): p. 75-92.

23. Yu, P., et al., *Associations between long-term exposure to PM2. 5 and site-specific cancer mortality: A nationwide study in Brazil between 2010 and 2018.* Environmental Pollution, 2022. **302**: p. 119070.

24. Chang, P., et al., *Minimizing DPM pollution in an underground mine by optimizing auxiliary ventilation systems using CFD.* Tunnelling and Underground Space Technology, 2019. **87**: p. 112121.

25. Duan, J., et al., *CFD numerical simulation on diffusion and distribution of diesel exhaust particulates in coal mine heading face.* Advanced Powder Technology, 2021. **32**(10): p. 3660-3671.

26. Liu, C., et al., *Behavior of the particulate matter (PM) emitted by trackless rubber-tyred vehicle (TRTV) at an idle speed under different movement conditions and ventilation optimization.* Science of The Total Environment, 2021. **783**: p. 147008.

27. Xu, G., et al., *Numerical study of diesel particulate matter distribution in an underground mine isolated zone.* Powder Technology, 2018. **339**: p. 947-957.

28. Konduri, I., M. McPherson, and E. Topuz. *Experimental and numerical modeling of jet fans for auxiliary ventilation in mines*. in *Proceedings of the 6th International Mine Ventilation Symposium*. 1997.

29. Liu, Q., et al., *Long-duct forced and short-duct exhaust ventilation system in tunnels: Formation and dust control analysis of pressure ventilation air curtain.* Process Safety and Environmental Protection, 2019. **132**: p. 367-377.

30. Cheng, W., et al., *Impact of pressure pumping ratio and location of air curtain generator on the dust resistance effect in fully mechanized workface.* J China Coal Soc, 2016. **41**(8): p. 1976-1983.

31. Zhou, G., et al., *Influence of mixed ventilation on particulate-gas diffusion and distribution of diesel engine exhaust in fully mechanized excavation face.* Scientific Reports, 2023. **13**(1): p. 1585.

32. Zhou, G., et al., *Numerical analysis on pollution law for dust and diesel exhaust particles in multiventilation parameter environment of mechanized excavation face.* Process Safety and Environmental Protection, 2022. **157**: p. 320-333.

33. Wang, X., et al., *Ventilation characteristics of double-forced air pipe ventilation in comprehensive mechanized excavation face and determination of its optimal parameters.* Energy Sources, Part A: Recovery, Utilization, and Environmental Effects, 2024. **46**(1): p. 2253-2269.

34. Gautam, S., et al., *Characterization of PM2.5 generated from opencast coal mining operations: A case study of Sonepur Bazari Opencast Project of India.* Environmental Technology & Innovation, 2016. **6**: p. 1-10.

35. Gautam, S., B.K. Prusty, and A.K. Patra, *Pollution due to particulate matter from mining activities.* health, 2012. **4**(5).

36. Wang, Z., et al., *Annual dust pollution characteristics and its prevention and control for environmental protection in surface mines.* Science of The Total Environment, 2022. **825**: p. 153949.

37. Luo, H., et al., *Analyzing Characteristics of Particulate Matter Pollution in Open-Pit Coal Mines: Implications for Green Mining.* Energies, 2021. **14**(9): p. 2680.

38. Wang, Z., et al., *Dust pollution in cold region Surface Mines and its prevention and control.* Environmental Pollution, 2022. **292**: p. 118293.

39. Chang, P. and G. Xu. *Review of Diesel Particulate Matter Control Methods in Underground Mines*. in *Proceedings of the 11th International Mine Ventilation Congress*. 2019. Singapore: Springer Singapore.

40. Yang, Y., et al., *Pollution and occupational protection of diesel particulate matter in underground space.* Environmental Science and Pollution Research, 2023. **30**(16): p. 45840-45858.

41. Liu, X., et al., *Behavior of diesel particulate matter transport from subsidiary transportation vehicle in mine.* Environmental Pollution, 2021. **270**: p. 116264.

42. Chang, P., et al., *Numerical investigation of diesel particulate matter dispersion in an underground development face during key mining activities.* Advanced Powder Technology, 2020. **31**(9): p. 3882-3896.

43. Gangal, M. *Summary of worldwide underground mine diesel regulations*. in *18th Mining Diesel Emission Council conference*. 2012. Toronto, Ontario, Canada.

44. Halim, A., *Ventilation requirements for diesel equipment in underground mines – Are we using the correct values?* 2017.

45. Ahbil, K., et al., *Influence of localized sources and meteorological conditions on dry-deposited particles: A case study of Gabès, Tunisia.* Science of The Total Environment, 2024. **954**: p. 176726.

46. Gautam, S., et al., *Personal exposure to air pollutants from winter season bonfires in rural areas of Gujarat, India.* Exposure and Health, 2020. **12**(1): p. 89-97.

47. Setu, S., et al., *Phytomonitoring of air pollution around brick kilns in urban area: Exploring the potential of plants for the remediation of pollutants.* Chemosphere, 2024. **368**: p. 143721.

48. Gautam, S., P. Kumar, and A.K. Patra, *Occupational exposure to particulate matter in three Indian opencast mines.* Air Quality, Atmosphere & Health, 2016. **9**: p. 143-158.

49. Blessy, A., et al., *IoT-based air quality monitoring in hair salons: Screening of hazardous air pollutants based on personal exposure and health risk assessment.* Water, Air, & Soil Pollution, 2023. **234**(6): p. 336.

50. Corrin, B. and A.G. Nicholson, *Occupational, environmental and iatrogenic lung disease.* Pathology of the Lungs, 2011: p. 327.

51. Organization, W.H., *Air quality guidelines: global update 2005: particulate matter, ozone, nitrogen dioxide, and sulfur dioxide*. 2006: World Health Organization.

52. Sanei, B., et al., *Occupational exposure to particulate matters and telomere length.* Environmental Science and Pollution Research, 2018. **25**(36): p. 36298-36305.

53. Nie, W., et al., *Study on PM diffusion and distribution of trackless rubber-tyred vehicle under different driving conditions in underground coal mining environment.* Environmental Science and Pollution Research, 2023. **30**(44): p. 99484-99500.

54. Mine Safety and Health Administration (MSHA), L., *Diesel Particulate Matter Exposure of Underground Metal and Nonmetal Miners*, D. of Labor, Editor. 2001, Federal Register: USA. p. 5706-5910.

55. Pope Iii, C.A., et al., *Lung cancer, cardiopulmonary mortality, and long-term exposure to fine particulate air pollution.* Jama, 2002. **287**(9): p. 1132-1141.

56. Raaschou-Nielsen, O., et al., *Air pollution and lung cancer incidence in 17 European cohorts: prospective analyses from the European Study of Cohorts for Air Pollution Effects (ESCAPE).* The lancet oncology, 2013. **14**(9): p. 813-822.

57. Burnett, R.T., et al., *An integrated risk function for estimating the global burden of disease attributable to ambient fine particulate matter exposure.* Environmental health perspectives, 2014. **122**(4): p. 397-403.

58. Lelieveld, J., et al., *The contribution of outdoor air pollution sources to premature mortality on a global scale.* Nature, 2015. **525**(7569): p. 367-371.

59. Marco, G. and X. Bo, *Air quality legislation and standards in the European union: background, status and public participation.* Advances in Climate Change Research, 2013. **4**(1): p. 50-59.

60. Li, X., L. Jin, and H. Kan, *Air pollution: a global problem needs local fixes.* Nature, 2019. **570**(7762): p. 437-439.

61. Park, M., et al., *Differential toxicities of fine particulate matters from various sources.* Scientific Reports, 2018. **8**(1): p. 17007.

62. Heinrich, U., et al., *Chronic effects on the respiratory tract of hamsters, mice and rats after long-term inhalation of high concentrations of filtered and unfiltered diesel engine emissions.* Journal of Applied Toxicology, 1986. **6**(6): p. 383-395.

63. Mauderly, J.L., et al., *Diesel exhaust is a pulmonary carcinogen in rats exposed chronically by inhalation.* Fundamental and applied toxicology, 1987. **9**(2): p. 208-221.

64. Heinrich, U., et al., *Chronic inhalation exposure of Wistar rats and two different strains of mice to diesel engine exhaust, carbon black, and titanium dioxide.* Inhalation toxicology, 1995. **7**(4): p. 533-556.

65. Nikula, K., et al., *Comparative pulmonary toxicities and carcinogenicities of chronically inhaled diesel exhaust and carbon black in F344 rats.* Fundamental and Applied Toxicology, 1995. **25**(1): p. 80-94.

66. Iwai, K., et al., *Early oxidative DNA damages and late development of lung cancer in diesel exhaust-exposed rats.* Environmental Research, 2000. **84**(3): p. 255-264.

67. Agency, U.E.P., *Health assessment document for diesel engine exhaust*. 2002, EPA Washington, DC. p. 669.

68. Garshick, E., et al., *A case-control study of lung cancer and diesel exhaust exposure in railroad workers.* American Review of Respiratory Disease, 1987. **135**(6): p. 1242-1248.

69. Garshick, E., et al., *A retrospective cohort study of lung cancer and diesel exhaust exposure in railroad workers.* American journal of respiratory and critical care medicine, 1988. **137**(4): p. 820825.

70. Development, H.D.o.S. and T. Transfer, *Carcinogenic effects of exposure to diesel exhaust*. 1988: US Department of Health and Human Services, Public Health Service, Centers ….

71. Humans, I.W.G.o.t.E.o.C.R.t. and I.A.f.R.o. Cancer, *Diesel and gasoline engine exhausts and some nitroarenes*. Vol. 46. 1989: World Health Organization.

72. Kachuri, L., et al., *Workplace exposure to diesel and gasoline engine exhausts and the risk of colorectal cancer in Canadian men.* Environmental Health, 2016. **15**: p. 1-12.

73. Garshick, E., et al., *Lung cancer in railroad workers exposed to diesel exhaust.* Environmental Health Perspectives, 2004. **112**(15): p. 1539-1543.

74. Garshick, E., et al., *Smoking imputation and lung cancer in railroad workers exposed to diesel exhaust.* American Journal of Industrial Medicine, 2006. **49**(9): p. 709-718.

75. Steenland, K., J. Deddens, and L. Stayner, *Diesel exhaust and lung cancer in the trucking industry: exposure–response analyses and risk assessment.* American journal of industrial medicine, 1998. **34**(3): p. 220-228.

76. Laden, F., et al., *Cause-specific mortality in the unionized US trucking industry.* Environmental Health Perspectives, 2007. **115**(8): p. 1192-1196.

77. Boffetta, P., et al., *Occupational exposure to diesel engine emissions and risk of cancer in Swedish men and women.* Cancer Causes & Control, 2001. **12**: p. 365-374.

78. Järvholm, B. and D. Silverman, *Lung cancer in heavy equipment operators and truck drivers with diesel exhaust exposure in the construction industry.* Occupational and Environmental Medicine, 2003. **60**(7): p. 516-520.

79. Olsson, A.C., et al., *Exposure to diesel motor exhaust and lung cancer risk in a pooled analysis from case-control studies in Europe and Canada.* American journal of respiratory and critical care medicine, 2011. **183**(7): p. 941-948.

80. Attfield, M.D., et al., *The diesel exhaust in miners study: a cohort mortality study with emphasis on lung cancer.* Journal of the National Cancer Institute, 2012. **104**(11): p. 869-883.

81. Silverman, D.T., et al., *The diesel exhaust in miners study: a nested case–control study of lung cancer and diesel exhaust.* Journal of the National Cancer Institute, 2012. **104**(11): p. 855-868.

82. Neumeyer‐Gromen, A., et al., *Diesel motor emissions and lung cancer mortality—Results of the second follow‐up of a cohort study in potash miners.* International journal of cancer, 2009. **124**(8): p. 1900-1906.

83. Ghose, M.K., *Generation and quantification of hazardous dusts from coal mining in the Indian context.* Environmental monitoring and assessment, 2007. **130**: p. 35-45.

84. Csavina, J., et al., *Metal and metalloid contaminants in atmospheric aerosols from mining operations.* Water, Air, & Soil Pollution, 2011. **221**: p. 145-157.

85. Harris, M.L., et al., *Collecting representative dust samples: A comparison of various sampling methods in underground coal mines.* Journal of Loss Prevention in the Process Industries, 2015. **36**: p. 195-202.

86. Sabanov, S., et al., *Analysis of Experimental Measurements of Particulate Matter (PM) and Lung Deposition Surface Area (LDSA) in Operational Faces of an Oil Shale Underground Mine.* Atmosphere, 2024. **15**(2): p. 200.

87. Scheepers, P., et al., *Exposure to dust and particle-associated 1-nitropyrene of drivers of diesel powered equipment in underground mining.* Annals of occupational hygiene, 2003. **47**(5): p. 379388.

88. Noll, J., et al., *Relationship between elemental carbon, total carbon, and diesel particulate matter in several underground metal/non-metal mines.* Environmental science & technology, 2007. **41**(3): p. 710-716.

89. Vermeulen, R., et al., *The Diesel Exhaust in Miners Study: IV. Estimating historical exposures to diesel exhaust in underground non-metal mining facilities.* Annals of Occupational Hygiene, 2010. **54**(7): p. 774-788.

90. Koponen, H., et al., *Applicability of aethalometers for monitoring diesel particulate matter concentrations and exposure in underground mines.* Journal of Aerosol Science, 2024. **177**: p. 106330.

91. Bugarski, A.D., et al., *Effects of diesel exhaust aftertreatment devices on concentrations and size distribution of aerosols in underground mine air.* Environmental science & technology, 2009. **43**(17): p. 6737-6743.

92. MSHA, M.S., *Health Administration. 30 CFR Part 57 Diesel Particulate Matter Exposure of Underground Metal and Nonmetal Miners; Final Rule.* Fed. Reg, 2005. **70**(107): p. 32868.

93. Khan, M.U., *Real-time diesel particulate matter monitoring in underground mine atmospheres, association with the standard method and related challenges*. 2017: Missouri University of Science and Technology.

94. Kimbal, K.C., et al., *Monitoring diesel particulate matter and calculating diesel particulate densities using Grimm Model 1.109 real-time aerosol monitors in underground mines.* Journal of Occupational and Environmental Hygiene, 2012. **9**(6): p. 353-361.

95. Noll, J., S. Janisko, and S.E. Mischler, *Real-time diesel particulate monitor for underground mines.* Analytical Methods, 2013. **5**(12): p. 2954-2963.

96. Mischler, S., A. Bugarski, and J. Noll. *Instrumentation for diesel particulate matter emissions research*. in *11th US/North American Mine Ventilation Symposium 2006: Proceedings of the 11th US/North American Mine Ventilation Symposium, 5-7 June 2006, Pennsylvania, USA*. 2006. CRC Press.

97. Arnott, W., et al. *Real-time measurements of diesel EC and TC in a Nevada gold mine with photoacoustic and DustTrak instruments: Comparison with NIOSH 5040 filter results*. in *12th US/North American Mine Ventilation Symposium. Reno, Nevada*. 2008.

98. Gillies, S. and H.W. Wu, *Evaluation of a first mine real time diesel particulate matter (DPM) monitor.* 2008.

99. Gillies, A., *Real-time diesel particulate matter ambient monitoring in underground mines.* Journal of Coal Science and Engineering (China), 2011. **17**: p. 225-231.

100. Gillies, S. and H.W. Wu. *Underground atmosphere real time personal respirable dust and diesel particulate matter direct monitoring*. in *Proceedings of 8th Underground Coal Operators' Conference*. 2008.

101. Wu, H.W., et al., *Real-time DPM ambient monitoring in underground mines.* 2010.

102. Takiff, L. and G. Aiken. *A real-time, wearable elemental carbon monitor for use in underground mines*. in *13th United States/North Am. Mine Vent. Symp*. 2010.

103. Janisko, S. and J. Noll. *Near real time monitoring of diesel particulate matter in underground mines*.
in *Proceedings of the 12th US/North American Mine Ventilation Symposium*. 2008. Reno, Nev.: Omnipress.

104. Noll, J., L. Patts, and R. Grau. *The effects of ventilation controls and environmental cabs on diesel particulate matter concentrations in some limestone mines*. in *Proceedings of the 12th US/North American Mine Ventilation Symposium*. 2008.

105. Noll, J., et al., *Portable instruments for measuring tailpipe diesel particulate in underground mines.* Mining engineering, 2013. **65**(10): p. 42.

106. Noll, J. and S. Janisko, *Evaluation of a wearable monitor for measuring real-time diesel particulate matter concentrations in several underground mines.* Journal of occupational and environmental hygiene, 2013. **10**(12): p. 716-722.

107. Gillies, A., et al. *Comparison of diesel particulate matter ambient monitoring practices in underground mines in Australia, the United States and South Africa*. in *10th International Mine Ventilation Congress, South Africa*. 2014.

108. Khan, M.U. and S. Gillies. *Realtime diesel particulate matter monitoring in US underground mines*. in *SME Annual Meeting*. 2015.

109. Khan, M. and S. Gillies. *Real-time monitoring of DPM, airborne Dust and correlating Elemental Carbon measured by two methods in underground mines in USA*. in *15th North American Mine Ventilation Symposium, Blacksburg, VA*. 2015.

110. Jafarigol, F., et al., *Particle number, mass, and surface area concentrations inside an underground metalliferous mine in Kazakhstan.* Atmospheric Pollution Research, 2023. **14**(9): p. 101871.

111. Yuan, L. and A. Smith, *Computational fluid dynamics modeling of spontaneous heating in longwall gob areas.* 2007.

112. Ren, T. and R. Balusu, *The use of CFD modelling as a tool for solving mining health and safety problems.* 2010.

113. Sullivan, P. and J. Van Heerden, *The simulation of environmental conditions in continuous miner developments using computational fluid dynamics.* Journal of the Mine Ventilation Society of South Africa;(South Africa), 1993. **46**(1).

114. Hargreaves, D. and I. Lowndes, *The computational modeling of the ventilation flows within a rapid development drivage.* Tunnelling and underground space technology, 2007. **22**(2): p. 150-160.

115. Wala, A., et al., *Mine face ventilation: a comparison of CFD results against benchmark experiments for the CFD code validation.* 2007.

116. Torno, S., et al., *Conventional and numerical models of blasting gas behaviour in auxiliary ventilation of mining headings.* Tunnelling and Underground Space Technology, 2013. **34**: p. 7381.

117. Ren, T., Z. Wang, and G. Cooper, *CFD modelling of ventilation and dust flow behaviour above an underground bin and the design of an innovative dust mitigation system.* Tunnelling and Underground Space Technology, 2014. **41**: p. 241-254.

118. Silvester, S., I. Lowndes, and D. Hargreaves, *A computational study of particulate emissions from an open pit quarry under neutral atmospheric conditions.* Atmospheric Environment, 2009. **43**(40): p. 6415-6424.

119. Han, F., et al., *Modeling the influence of forced ventilation on the dispersion of droplets ejected from roadheader-mounted external sprayer.* International Journal of Mining Science and Technology, 2014. **24**(1): p. 129-135.

120. Kurnia, J.C., A.P. Sasmito, and A.S. Mujumdar, *Dust dispersion and management in underground mining faces.* International Journal of Mining Science and Technology, 2014. **24**(1): p. 39-44.

121. Safa, R. and A.S. Goharrizi, *CFD simulation of an industrial hydrocyclone with Eulerian–Eulerian approach: A case study.* International Journal of Mining Science and Technology, 2014. **24**(5): p. 643-648.

122. Zheng, Y., et al., *DPM dispersion inside a single straight entry using dynamic mesh model.* International Journal of Coal Science & Technology, 2017. **4**(3): p. 234-244.

123. Liu, C., et al., *The migration of CO and PM under different working conditions of trackless rubber tyred vehicle and health risk assessment of underground personnel.* Chemosphere, 2022. **307**: p. 135750.

124. Liu, C., et al., *Numerical study on temporal and spatial distribution of particulate matter under multi-vehicle working conditions.* Science of The Total Environment, 2023. **862**: p. 160710.

125. van Wachem, B.G.M. and A.E. Almstedt, *Methods for multiphase computational fluid dynamics.* Chemical Engineering Journal, 2003. **96**(1): p. 81-98.

126. Enwald, H., E. Peirano, and A.E. Almstedt, *Eulerian two-phase flow theory applied to fluidization.* International Journal of Multiphase Flow, 1996. **22**: p. 21-66.

127. Gidaspow, D., J. Jung, and R.K. Singh, *Hydrodynamics of fluidization using kinetic theory: an emerging paradigm: 2002 Flour-Daniel lecture.* Powder Technology, 2004. **148**(2): p. 123-141.

128. Deen, N.G., et al., *Review of discrete particle modeling of fluidized beds.* Chemical Engineering Science, 2007. **62**(1): p. 28-44.

129. Zhu, H.P., et al., *Discrete particle simulation of particulate systems: A review of major applications and findings.* Chemical Engineering Science, 2008. **63**(23): p. 5728-5770.

130. Zhu, H.P., et al., *Discrete particle simulation of particulate systems: Theoretical developments.* Chemical Engineering Science, 2007. **62**(13): p. 3378-3396.

131. Chiesa, M., et al., *Numerical simulation of particulate flow by the Eulerian–Lagrangian and the Eulerian–Eulerian approach with application to a fluidized bed.* Computers & Chemical Engineering, 2005. **29**(2): p. 291-304.

132. Vegendla, S.N.P., G.J. Heynderickx, and G.B. Marin, *Comparison of Eulerian–Lagrangian and Eulerian–Eulerian method for dilute gas–solid flow with side inlet.* Computers & Chemical Engineering, 2011. **35**(7): p. 1192-1199.

133. de Jong, J.F., et al., *Comparison of a Discrete Particle Model and a Two-Fluid Model to experiments of a fluidized bed with flat membranes.* Powder Technology, 2012. **230**: p. 93-105.

134. Chang, P., et al., *Comparison of underground mine DPM simulation using discrete phase and continuous phase models.* Process Safety and Environmental Protection, 2019. **127**: p. 45-55.

135. Yin, W., G. Zhou, and D. Gao, *Simulation analysis and engineering application of distribution characteristics about multi-stage atomization field for cutting dust in fully mechanized mining face.* Advanced Powder Technology, 2019. **30**(11): p. 2600-2615.

136. Yu, H., et al., *An investigation of the nozzle's atomization dust suppression rules in a fullymechanized excavation face based on the airflow-droplet-dust three-phase coupling model.* Advanced Powder Technology, 2018. **29**(4): p. 941-956.

137. Hu, S., et al., *Numerical study of gas-solid two-phase flow around road-header drivers in a fully mechanized excavation face.* Powder Technology, 2019. **344**: p. 959-969.

138. Yu, H., et al., *Mechanisms of dust diffuse pollution under forced-exhaust ventilation in fullymechanized excavation faces by CFD-DEM.* Powder Technology, 2017. **317**: p. 31-47.

139. Liu, Q., et al., *Research on tunnel ventilation systems: Dust Diffusion and Pollution Behaviour by air curtains based on CFD technology and field measurement.* Building and Environment, 2019. **147**: p. 444-460.

140. ANSYS, I., *ANSYS Fluent Theory Guide*. 2021: U.S.A. p. 1069.

141. Gang Zhou, et al., *Numerical analysis on pollution law for dust and diesel exhaust particles in multi-ventilation parameter environment of mechanized excavation face.* Process Safety and Environmental Protection, 2022. **157**: p. 320-333.

142. Roache, P.J., *Perspective: A Method for Uniform Reporting of Grid Refinement Studies.* Journal of Fluids Engineering, 1994. **116**(3): p. 405-413.

143. Tang, M. and G. Tan. *CFD Calculation of Transonic Flow Around Airfoil*. in *2023 IEEE 6th Information Technology, Networking, Electronic and Automation Control Conference (ITNEC)*. 2023.

144. Kat, C.-J. and P.S. Els, *Validation metric based on relative error.* Mathematical and Computer Modelling of Dynamical Systems, 2012. **18**(5): p. 487-520.

145. Yen, Y.-C., et al., *Indoor ozone and particulate matter modify the association between airborne endotoxin and schoolchildren's lung function.* Science of The Total Environment, 2020. **705**: p. 135810.

146. Javed, W. and B. Guo, *Performance Evaluation of Real-time DustTrak Monitors for Outdoor Particulate Mass Measurements in a Desert Environment.* Aerosol and Air Quality Research, 2021. **21**(6): p. 200631.

147. Zhao, Y., S. Kato, and J. Zhao, *Numerical Investigation of Brownian, Gradient, and Turbulent Coagulation Under Moving Vehicle Conditions in an Underground Garage.* Journal of Dispersion Science and Technology, 2016. **37**(2): p. 258-269.

148. Chen, D., et al., *The diffusion of dust in a fully mechanized mining face with a mining height of 7 m and the application of wet dust-collecting nets.* Journal of Cleaner Production, 2018. **205**: p. 463476.

149. Hua, Y., et al., *The development and application of a novel multi-radial-vortex-based ventilation system for dust removal in a fully mechanized tunnelling face.* Tunnelling and Underground Space Technology, 2020. **98**: p. 103253.

150. Guo, Y.F., *Study on the emission characteristics and treatment status of VOCs in refining enterprises.* J. Shandong Univ. Sci. Technol. (Natural Science Edition), 2020. **39**(6): p. 63-70.

151. Xu, C., et al., *Multi-factor numerical simulation study on spray dust suppression device in coal mining process.* Energy, 2019. **182**: p. 544-558.

152. Zhou, Q., et al., *Changes of physical properties of coal dust with crush degrees and their effects on dust control ability of the surfactant solution spray.* Environmental Science and Pollution Research, 2022. **29**(22): p. 33785-33795.

153. Nie, W., et al., *Dynamic dispersion and high-rise release of coal dust in the working surface of a large-scale mine and application of a new wet dust reduction technology.* Journal of Cleaner Production, 2022. **351**: p. 131356.

154. Hua, Y., et al., *Pattern characterization concerning spatial and temporal evolution of dust pollution associated with two typical ventilation methods at fully mechanized excavation faces in rock tunnels.* Powder Technology, 2018. **334**: p. 117-131.

155. Ray, S.K., et al., *CFD modeling to study the effect of particle size on dispersion in 20l explosion chamber: An overview.* International Journal of Mining Science and Technology, 2020. **30**(3): p. 321-327.

156. Zheng, Y., et al., *Effect of auxiliary ventilations on diesel particulate matter dispersion inside a dead-end entry.* International Journal of Mining Science and Technology, 2015. **25**(6): p. 927-932.

157. Knaus, H. and B. Dürr, *Numerical simulation including model validation of wind flow in alpine terrain in eastern Switzerland.* Progress in Computational Fluid Dynamics, an International Journal, 2015. **15**(3): p. 168-176.

158. Gaioni, V. and K. Fernandez-Cosials, *A Practical Verification and Validation Procedure for Computational Fluid Dynamics*. 2020.

159. Liu, H., et al., *Numerical analysis of spatial and temporal distribution of exhaust emissions from multiple underground diesel vehicles under different idling conditions.* Fuel, 2024. **374**: p. 132234.

160. Guo, L., et al., *The dust diffusion modeling and determination of optimal airflow rate for removing the dust generated during mine tunneling.* Building and Environment, 2020. **178**: p. 106846.

161. Zhou, G., et al., *Numerical simulation investigation on optimal air volume for dilution dust-gas by forced ventilation in fully mechanized driving face.* Environmental Science and Pollution Research, 2023. **30**(7): p. 17723-17740.

162. Zhang, W., et al., *Study on the distribution characteristics of dust with different particle sizes under forced ventilation in a heading face.* Powder Technology, 2022. **406**: p. 117504.

163. Zheng, Y., et al., *Design of push–pull system to control diesel particular matter inside a dead-end entry.* International Journal of Coal Science & Technology, 2015. **2**(3): p. 237-244.

164. Kim, M., et al. *Numerical Investigation of Characteristics of Mine Ventilation Using One or Two Ducts in Underground Mining Faces*. in *Proceedings of the International Conference on Innovations for Sustainable and Responsible Mining*. 2021. Cham: Springer International Publishing.